Experimental Modelling of Debris Damming Loads on Structures in Extreme Flooding Events

Gabriella Mauti

Thesis submitted to the

Faculty of Graduate and Postdoctoral Studies

in partial fulfillment of the requirements for the degree of

Master of Applied Science in Civil Engineering

Under the auspices of the Ottawa-Carleton Institute for Civil Engineering

University of Ottawa

Ottawa, Ontario, Canada

August 2019

Abstract

Extreme flooding events have resulted in significant loss of life and extensive damage to coastal communities. These events include tsunamis, hurricanes, flash floods, and tropical storms. The devastation and destruction caused by them has been illustrated recently in the 2004 Indian Ocean Tsunami, the 2005 Hurricane Katrina, and the 2011 Tohoku Tsunami. The unexpected failure of infrastructure as a result of large-scale flood events demonstrated that past design guidelines did not properly address the various loads occurring during these events, particularly in terms of extreme loads. Research on extreme loading on infrastructure due to debris has focused predominantly on the impact of individual debris objects colliding with structures. Little research has been conducted on the loading due to debris accumulating onto or around structures, commonly referred to as *debris damming*. Debris dams form when entrained solid objects accumulate in-between or onto the face of structures. Debris damming has been treated as a quasi-static load, which can increase hydrodynamic loading due to an enlarged cross-sectional area of the structure exposed to the flow. In addition, debris damming has been shown to result in overtopping of structures and increased scour around them.

This research aimed to investigate the impact of debris dams on structural loading and surrounding flow behaviour. This study examined the influence of debris dam shape, porosity, and height on loads induced onto structures. In addition, force coefficients were determined and analyzed in terms of Froude number and debris dam geometry. Experiments were conducted in the Hydraulic Flume at the University of Ottawa, Canada. Idealized debris dams were attached to a column and tested in both steady-state and transient flow conditions. The experimental program conducted in steady-state conditions was tested with flows exhibiting Froude numbers ranging from 0.37 to 0.61 and the program conducted in transient flow conditions, through the use of a dam-break wave, tested Froude numbers ranging from 0.92 to 1.56. Due to the random nature of debris dam formation, semi-cylindrical and rectangular debris dams with three varying heights and three porosities were tested.

The experimental campaigns investigated the influence of debris dam geometry on structural loading and the surrounding flow behaviour. The research conducted showed that the loading due to debris damming increased with water depth and flow velocity. The resistance coefficients were found to be a function of the Froude number and the flow depth to obstacle width ratio. Increased dam height resulted in increased resistance forces acting on the debris dams and columns. However, the height had greater impact on the resistance coefficients in steady-state flow conditions comparing to that observed in the tests conducted in transient flow. The porosity resulted in a decrease in loading; however, the porosity had little influence on the effective resistance coefficients as porous holes result in an increase in skin friction.

Acknowledgements

First, I would like to thank my academic supervisors, Dr. Ioan Nistor and Dr. Majid Mohammadian. They both provided me with continuous guidance, assistance, and resources throughout my Masters. Both supervisors mentored me with great skill, attention to detail, and technical expertise, allowing me to have the best possible experience at the University of Ottawa. Due to their encouragements and support, I had many opportunities to travel and improve upon my skills. I am very grateful for their astounding leadership as it greatly improved my work and my overall knowledge in the field of hydraulic engineering.

I would also like to express my deepest gratitude to my research colleague, Jacob Stolle, who I worked with throughout my research. He provided me with countless advice and support during my research projects and my Masters. His technical expertise and experience in the field of hydraulic engineering and physical modelling was extremely helpful and essential to the work that I completed. It was a great experience working with Jacob during my time at the University of Ottawa as a graduate student and at the Technical University of Braunschweig in Germany.

Lastly, I would like to thank my family and friends for their unwavering support throughout my academic career. Without them, I would not have been able to complete this work and be where I am today. I am endlessly grateful for their constant encouragement, care, and kindness.

Table of Contents

List of Figures

List of Tables

List of Symbols

A_B	Bulk debris dam area (m^2)
A_E	Effective debris dam area (m^2)
B	Obstacle width (m)
C_D	Drag coefficient
C_H	Hydrostatic coefficient
C_R	Resistance coefficient
C_{RB}	Bulk resistance coefficient
C_{RE}	Effective resistance coefficient
D	Column diameter (m)
d	Flow depth (m)
F_D	Drag force (N)
$F_{HS,u}$	Downstream hydrostatic force (N)
$F_{HS,u}$	Upstream hydrostatic force (N)
F_R	Resistance force (N)
Fr	Froude number
g	Acceleration due to gravity (m/s^2)
H	Debris dam height (m)
h	Flow depth (m)
h_d	Downstream flow depth (m)
h_u	Upstream flow depth (m)
h_o	Impoundment depth (m)
h_1	Far upstream flow depth (m)

h_2 Far downstream flow depth (m)

L_M Model length (m)

L_P Prototype length (m)

n Debris dam porosity

P Probability

R^2 Coefficient of determination

S_h Horizontal hole spacing of debris dams (mm)

S_v Vertical hole spacing of debris dams (mm)

t Time (s)

$t_{critical}$ Critical t-value

t_{stat} Statistical t-value

u Flow velocity (m/s)

W Debris dam width (m)

λ Scaling multiplication factor

κ Debris dam curvature

ρ_f Density of the fluid (kg/m^3)

Chapter 1. Introduction

1.1 Background

Thirty percent of the world's population resides in low-lying coastal flood plains with the majority of the world's megacities being in coastal regions (Neumann et al., 2015). Coupled with the expected rising sea levels as a result of climate change, it becomes of increasing importance to design safer coastal structures. Historically, the failures and damage of such structures were triggered by large-scale flooding events occurring off the coasts such as hurricanes, storm surges, and tsunamis. These failures have demonstrated the growing importance in better design standards and guidelines against large-scale flood events.

Extreme flooding events are among the most damaging and devastating natural disasters. In 2004, an earthquake with a magnitude of 9.1 to 9.3 occurred off the coast of Indonesia, and resulted in a large tsunami event which affected many countries around the Indian Ocean, particularly Thailand, Sri Lanka, India, and Indonesia. The numbers of missing and dead were 51,400 and 181,700, respectively, totalling to 233,100 victims (Matsutomi et al., 2006). Hurricane Katrina hit New Orleans on April 29, 2005 and affected the Gulf Coast region over several days, causing damage to infrastructures including buildings, houses, and transportation systems. Damage to transportation systems is generally not only costly but also poses a threat to citizens as it limits access to emergency response and recovery efforts. This hurricane resulted in significant losses, with estimated costs of $1 billion in bridge repairs and replacement alone (TCLEE, 2006). The 2011 Tohoku Tsunami was triggered by the largest recorded earthquake to have ever occurred in Japan and is one of the most catastrophic and costly natural disasters in history. The number of deaths and missing people was 19,334 (Suppasri et al., 2012) and the direct costs were estimated to be US$211 billion (Kajitani et al., 2013). Prior to this event, reinforced concrete structures were considered safe in tsunami events. However, several reinforced concrete structures failed or were severely damaged, as illustrated in Figure 1.1 (Yeh et al, 2013).

Figure 1.1: An overturned reinforced concrete structure in Onagawa, Japan, after the 2011 Tohoku Tsunami (courtesy of Dr. Ioan Nistor).

Canada has the longest coastline in the world bordering three oceans: the Pacific Ocean, the Atlantic Ocean, and the Arctic Ocean. Canada is also at risk for tsunami events, which have been generated in the past by earthquakes and large-scale landslides. An assessment completed by Leonard et al. (2012) has shown that the probability of exceedance in 50 years for a tsunami hazard with a runup greater than 1.5 metres for the outer Pacific coastline is 40 to 80 percent. The probability of exceedance in 50 years for the Atlantic and Arctic coastline is 1 to 15 percent and less than 1 percent, respectively. Large tsunami inundations could occur along the west coast of Canada. There is particular concern for the coast of Vancouver Island due to the large predicted tsunami runup and the populous regions on the island, as illustrated in Figure 1.2. In addition, tropical storms and hurricanes occur frequently in Atlantic Canada, causing significant inundation of surges and damage to coastal regions. These storms are also expected to increase in magnitude and frequency due to the changing climate (Duinker, 2002).

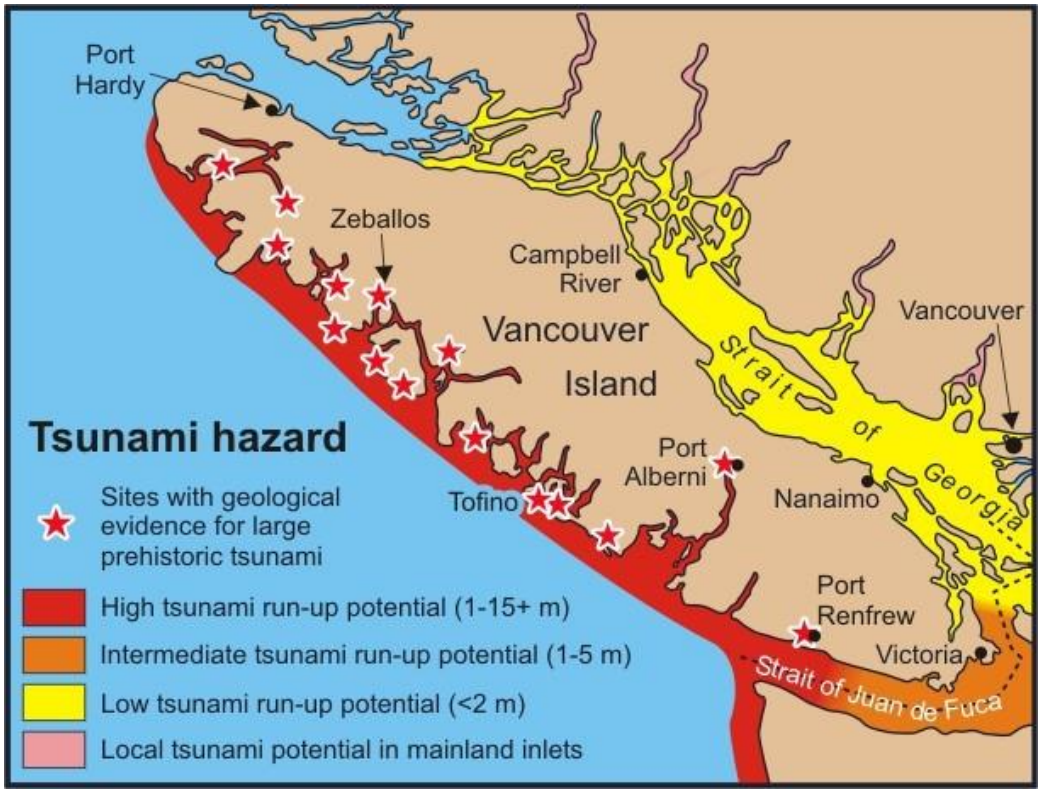

Figure 1.2: Expected maximum runup in the event of a tsunami affecting Vancouver Island and surrounding areas (adopted from City of Victoria, www.victoria.ca).

Unexpected damage or failure to infrastructure as a result of extreme flooding events has demonstrated the lack of understanding surrounding extreme loads (Yeh et al., 2014). Loading that is often difficult to assess, especially in terms of post-flood field surveys, is the loading due to debris (Yeh et al., 2013; Nistor et al., 2017). Debris entrained by storm surges can form accumulations in front of or in-between structures, forming what is commonly referred to as a *debris dam*, illustrated in Figure 1.3. Debris damming has been observed in several field surveys conducted after major tsunami events (Yeh et al., 2014). Critical structures were commonly designed against the hydrodynamic loading due to inundation, while the loading effects of debris were ignored, resulting in structural failures (Yeh et al., 2014). Debris dams result in increased flow obstruction, further restricting the flow path surrounding structures. This blockage results in a greater area exposed to the flow adjacent to structures, resulting in greater drag forces. In addition, the blockage due to debris dams can result in increased water depth upstream of the structure (backwater effect), causing greater hydrostatic pressures in the flow direction and potentially overtopping structures (Schmocker and Hager, 2013; Stolle et al., 2017). Debris dams are typically composed of buoyant materials, thus, redirecting flow and increasing the magnitude of vertical velocities. This redirection of the surrounding flow has been known to result in increased scour surrounding the foundations of structures (Melville and Dongol, 1992; Pagliara and Carnacina, 2011).

Figure 1.3: Photos of debris dams that had formed on structures after the 2011 Tohoku Tsunami (courtesy of Dr. Ioan Nistor).

Guidelines and recommendations have been developed to design critical infrastructure against the loading due to extreme flooding events. While some guidelines regarding debris damming loads have been outlined in these standards, the design prescriptions vary within each standard. The Federal Emergency Management Agency (FEMA) in the United States has developed two sets of guidelines related to coastal flooding events. FEMA P-55 (2011) provides details on planning, designing, and constructing coastal structures. This standard advises users to design against debris impact loads, however, the effects of debris damming loads are ignored. FEMA P-646 (2012) provides guidelines to design structures that shall be used for vertical tsunami evacuation structures. This guideline recommends the use of the drag force equation to estimate debris damming forces, where the width used in the drag force calculation formula is the breadth of the debris rather than the structure's geometrical width. A drag coefficient of 2.0 is recommended while the recommended minimum debris breadth is 12.0 m. The American Society of Civil Engineers (ASCE) developed a standard for the design of critical infrastructure presented in ASCE7-Chapter 6: Tsunami Loads and Effects (Chock, 2016). The loading due to debris accumulations is accounted for by increasing the minimum closure ratio used when calculating the drag force of a structure.

There has been little research completed in terms of the loading due to debris dams. Extensive research has been conducted on debris accumulations surrounding bridge piers in the field of river engineering, due to

the woody debris that are commonly observed in riverine systems. This research has focused primarily on debris dams' impact on scour. The research that has been conducted on the loading due to debris in river systems has also been conducted in steady-state flow conditions and in a lower range of Froude numbers. Therefore, there is a significant gap in research regarding debris damming loads in extreme flooding events. It is difficult to assess debris damming loads in field surveys due to the dissipation of debris dams post-disaster and due to the uncertainties associated with surveying flooding events. Therefore, experimental investigations regarding debris damming are required in a higher range of Froude numbers and in transient flow conditions, as there can be changes in debris damming behaviour depending on the surrounding flow conditions (Stolle et al., 2018a).

1.2 Objectives

Due to the lack of research with respect to the loading due to debris damming, particularly in extreme, rapid flooding events, this study intends to analyze debris damming loads and determine the influence that the debris dam geometry has on loading. This is expected to provide a much needed data set on the loading due to debris and a greater understanding of the impacts of debris dam geometry. Ultimately, this research aims to assist in the development of engineering guidelines and provide recommendations for use in the design of critical infrastructure. Specifically, the main objectives of this study are to:

- Investigate the influence of debris dam geometry on the forces acting on the impacted structure. This is performed by comparing the loads obtained in both studies to the individual geometry variables, including dam shape, height, and porosity.
- Examine the associated flow conditions surrounding the debris dams, in terms of flow runup and depressions upstream and downstream of the debris dams, respectively.
- Analyze force coefficients and the relationship between debris dam geometry by isolating the debris dam geometry variables and comparing them to the determined force coefficients.
- Provide a range of values for the force coefficients in terms of the flow conditions and debris dam geometry.

1.3 Scope

This study investigates the impacts of debris damming on hydraulic loading and flow behaviour surrounding structures. This is achieved through the use of idealized debris dams attached to a column and tested in steady-state and transient flow conditions. The idealized debris dams vary in terms of dam height, dam porosity, and dam shape. Three dam heights, three dam porosities, and two dam shapes were tested in steady flows with three varying flow rates and a dam-break wave with three various impoundment depths.

The impacts of surrounding flow conditions and the loading acting on the column and debris dam are investigated to determine relationships between loading and debris geometry.

In order to compare the impact of debris geometry on loading, force coefficients are defined. The force coefficients allow for a comparison of the varying resistance created by the debris dams. The force coefficients are compared to the isolated geometry variables so that the debris geometry could be quantitatively compared to the induced loads. Defining force coefficients allows for further understanding of the loading due to debris dams and improved design guidelines for flood-resistant structures.

This research focused on the physical modelling of debris dams in extreme flooding events. There are several limitations of the study including:

- Only one model scale was tested throughout both research projects: this was a 1:30 scale based on Froude similitude. This scale was chosen to be as large as possible without being unreasonable in terms of the flow conditions in the available experimental setting.
- The idealized debris dams tested in this study were fixed to a column so buoyancy effects of the debris were neglected. Typically, debris dams are composed of buoyant materials.
- The idealized debris dams were assumed to be *smooth* as they were constructed of plastic and aluminum. In reality, debris dams have a roughness associated with them, however, this study focused on the impacts of debris dam *geometry*.
- Only three variations of height and porosity and two variations of debris shape were investigated due to time limitations of the study. A more comprehensive review of varying heights and porosity should also be investigated to further understand the debris dam geometry' impacts on loading and flow behaviour.
- The porosity of the debris dams, in the form of uniformly distributed holes was modelled such that they were parallel with the flow direction. In reality, the debris dams would have three-dimensional voids, causing greater resistance to the flow.

This project is a preliminary investigation regarding the effects of debris damming on structural loading and the surrounding flow behaviour. Further investigations should be undertaken to assess more variables related to debris dams such as roughness or permeability and varying debris length and width. The findings of this research provide a better understanding of the effects of debris dam height, porosity, and shape on the induced loadings and flow conditions.

1.4 Novelty and Contributions

Little research has been conducted on the loading effects of debris dams. In addition, research regarding debris dams has been conducted in the field of river engineering and, therefore, the research was conducted in steady-state flow conditions in a lower range of the Froude number. The present study investigates the loading effects of debris dams tested in both steady-state and transient flow conditions scaled to those observed in extreme flooding events. This study is one of the few studies regarding debris damming loads tested in a higher range of Froude numbers and in transient flow conditions. Particularly, this study provides further information on the influence of the debris dam geometry on structural loading in complex flow conditions. Idealized debris dams were purposely used in this study to model the various geometric debris dam variables. To the author's knowledge, this is the first study that utilizes idealized debris dam geometries to study the structural loading and flow behaviour surrounding debris dams in extreme flow conditions. Idealized debris dams allow for the isolation of geometric variables, which can be further used to quantitatively compare the tested variables to the experimental results.

Design guidelines prescribe debris damming loads to be predicted using the drag force equation. However, little research has been conducted on the drag coefficient of debris dams. This study presents force coefficients of debris dams in terms of the geometry of the debris dams and the surrounding flow conditions obtained, for the first time, in extreme flow conditions. This study also presents the novel definition of two force coefficients, termed as the *bulk resistance coefficient* and the *effective resistance coefficient*. The comparison on these two force coefficients allows for a further understanding of the impacts of porosity on debris damming loads.

1.5 Publications

Below are a list of publications where the current author is a contributor as part of this study conducted at the Hydraulic Laboratory at the University of Ottawa.

Journal Articles

1. Mauti, G., Stolle, J., Takabatake, T., Nistor, I., Goseberg, N., Mohammadian, M. (2019). *Experimental investigation of loading due to debris dams on structures*.
   Status: Accepted with the Journal of Hydraulic Engineering (JHE-ASCE).
2. Mauti, G., Stolle, J., Nistor, I., Mohammadian, M., Goseberg, N. (2019). *Experimental investigation of loading due to debris dams in transient flow conditions*.
   Status: Submission in progress.

Conference Proceedings

3. Mauti, G., Stolle, J., Nistor, I., Mohammadian, M. (2019). *Experimental investigation of debris damming in transient flow conditions.*
   Status: Accepted and presented at the IAHR World Congress 2019.

1.6 Outline of the Thesis

This thesis is organized as follows.

Chapter 1 provides an outline of the objectives, scope, and novelty of the research presented in the thesis.

Chapter 2 is a comprehensive review of the literature related to the field of the author's research. This chapter first outlines the methods of transportation of debris and the formation processes of debris dams. The chapter also explains the impact that debris dams have on structural loading and flow behaviour. The relationship of geometry and flow conditions on the drag coefficient of flow obstacles is examined. Finally, a discussion of the research needs drawn from the review of the body of literature investigated are provided, which includes an explanation regarding the loading and flow behaviour due to debris damming in extreme flow conditions.

Chapter 3 presents the experimental study conducted by the author on the impacts of the debris dam geometry on the surrounding flow conditions and hydraulic loading through the use of idealized debris dams. The idealized debris dams varied in terms of shape, height, and porosity. This study was conducted in steady-state flow conditions using three flow rates to obtain a better understanding of the fluid-structure interaction of debris dams. The results and analysis conducted demonstrated the various influences of debris dam geometry on the structural loading and surrounding flow behaviour. The work presented is a manuscript titled "Experimental investigation of loading due to debris dams on structures" which is currently accepted with the Journal of Hydraulic Engineering (ASCE).

Chapter 4 presents a study conducted in transient flow conditions on the impacts of debris dam geometry on structural loading through the use of a dam-break wave with three impoundment depths tested. The idealized debris dams, which varied in terms of shape, height, and porosity, were utilized to investigate these varying debris dam geometry variables. The results illustrated the affects that the debris dam geometry had on the loading tested in violent, turbulent flows. This work presented herein is a manuscript titled "Experimental investigation of loading due to debris dams in transient flow conditions" and the journal submission is currently in progress.

Chapter 5 presents the conclusions of this research projects. Recommendations for future work on the investigated research topic are also suggested and discussed.

Chapter 2. Literature Review

2.1 Physical Modelling

2.1.1 Scaling

Scaling of physical models has been a common issue in the field of hydraulic engineering. For hydraulic models to be considered similar to prototype, the model must display one of the three various similarities described below (Chanson, 2004):

- Geometric similarity: the ratios of model lengths to prototype lengths are equal.
- Kinematic similarity: the ratios of model velocities to prototype velocities are equal.
- Dynamic similarity: the ratios of model forces to prototype forces are equal.

By using the ratios of length, velocity, and forces, further ratios can be determined such as mass, time, discharge, and pressure. Dynamic similarity is recommended for use in open channel flow. The Froude number is commonly used to scale physical models so that dynamic similarity is achieved, which scales for inertial forces and gravity forces. The Froude number is particularly useful for scaling of models in open channel flows, as gravity effects are important in open channel flow. Other common scaling mechanisms include using the Reynolds number, which is typically used for fully enclosed flows as the pressure losses are essentially related to the Reynolds number, and the Weber number, which is commonly used to model air entrainment in water as surface tension is dominant (Chanson, 2004). For the present study, the Froude number was chosen to scale the physical models as the tests were conducted in open channel flow. To scale the length and velocity using Froude similitude, the multiplication factor, λ, can be used, respectively:

$$\frac{L_P}{L_M} = \lambda \tag{2.1}$$

$$\frac{V_P}{V_M} = \sqrt{\lambda} \tag{2.2}$$

where L_P is the prototype length, L_M is the model length, V_P is the prototype velocity, and V_M is the model velocity. Typically, physical models examining forces on solid bodies are scaled using ratios between 1:10 to 1:50 (Hughes, 1993). Scale effects may exist as distortions can be introduced due to the occurrence of physical processes (i.e. viscosity and surface tension) other than the dominant process (gravity driven flow), however, it is neither practical nor feasible to scale to several physical processes in physical models. To minimize the scale effects in terms of Reynolds number, it is recommended to obtain large Reynolds

number and fully turbulent flow in the physical models, with a Reynolds number exceeding 1.25×10^4 (Chow, 1959). In addition, to minimize any surface tensions effects, a Weber number greater than 100 is recommended (Peakall and Warburton, 1996).

2.1.2 Tsunami Modelling

Tsunami waves are long gravity waves caused by the rapid displacement of a large body of water (Rossetto et al., 2011). Tsunamis are triggered mainly by earthquakes, but can also be caused by landslides or volcanic eruptions. During the 2004 Indian Ocean Tsunami, the mean celerity of the tsunami waves reached 200 m/s and the mean wavelength was 500 km in the offshore region (Kulikov and Mendvedev, 2005). As the water depth decreases with onshore movement, the celerity decreases and the wave height increases. Tsunamis then result in significant inundation of coastal areas due to their very long wavelengths with wave heights of several metres.

After conducting field surveys of the 2011 Tohoku tsunami, Takahashi et al. (2011) identified four main inundations of tsunamis approaching shore, illustrated in Figure 2.1. The first is the breaking wave type where tsunami waves breaks near the shore, travel over sand dunes, and then propagate for several kilometres over low-lying land. The second type is the high runup type where the tsunami breaks and then produces high runup on a relatively steep slope. The third type is the slow-varying type, which occurs at high cliffs and results in the wave to not break but rather smoothly increase water levels up the face of the cliff. The fourth is the overtopping type in which tsunamis overtop and inundate land due to the deep sea levels and relatively flat land.

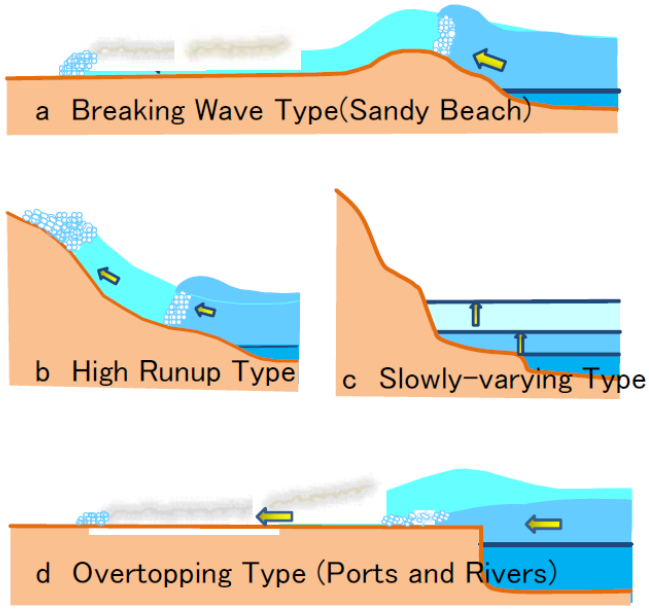

Figure 2.1: Typical intrusions of tsunami waves approaching the shore (adopted from Takahashi et al. (2011)).

Physical modelling of the onshore tsunami wave in terms of wave generation has been a commonly difficult issue due to the long wavelengths and time periods associated with tsunami waves. Solitary waves have been commonly used as it was discovered that a positive surface disturbance will eventually lead to the formation of solitary waves (Hammack, 1973; Hammack and Segur, 1974). In addition, solitary waves have constant form in constant depth (Goring, 1978). However, Madsen et al. (2008) demonstrated that solitary waves could not properly model the geophysical scales of tsunamis. It was concluded that the magnitude of the time-scales or space-scales that were observed in the 2004 Indian Ocean tsunami could not be obtained through laboratory solitary waves.

Another method of physically modelling onshore tsunamis is through the use of the dam-break wave. This method consists of a volume of water that is rapidly released from a reservoir into the channel. Chanson (2006) analyzed videos from the 2004 Indian Ocean Tsunami and concluded that a dam-break wave is similar to a tsunami bore propagating over a coastal plain. This method typically utilizes a vertical-lift gate releasing a volume of water from a reservoir into a channel. This system is beneficial due to its relative simplicity. Hager and Lauber (1996) stated that scaling effects are negligible when modelling a dam-break wave in a rectangular channel if the impoundment depth is greater than 0.30 m and that the flow is governed by Froude similarity. Dam-break waves modelled using a vertical lift gate have been successfully implemented in several studies including the modeling of columns in tsunami flows by Arnason (2005), an experimental investigation modelling boulder transportation in tsunami flows by Imamura et al. (2008), and an experimental study to determine the impact of extreme flows on structures by Liang et al. (2015). Recently, Stolle et al. (2018b) illustrated that a swing gate also appropriately models the dam-break wave. The modelling of the dam-break wave using a swing gate has been effectively utilized for investigating tsunami loading on freestanding structures (Nouri et al., 2010), an investigation on the drag coefficients of surface-piercing obstacles (Al-Faesly et al., 2012), and to physically investigate debris impact on structures in tsunami events (Derschum et al., 2017).

2.2 Flow Obstacles

2.2.1 Drag Force

The drag force is a commonly defined force in fluid mechanics and is described as a resistance force created by an obstacle opposing the motion of a fluid. The drag force acts opposite to the direction of the flow. The drag force consists of pressure drag, caused by the obstacle obstructing the flow field, and friction drag, which is caused by the friction of the object against the fluid. The widely known drag force equation is defined as:

$$F_D = \frac{1}{2} C_D \rho_f B h u^2 \tag{2.3}$$

where C_D is the drag coefficient, ρ_f is the density of the fluid, B is the flow obstacle width, h is the obstacle height submerged in the fluid, and u is the flow velocity.

2.2.2 Choked Flows

There has been significant research conducted on surface-piercing obstacles in open channel flow. A contribution to this research is characterizing the varying flow conditions surrounding the obstacle. Through a theoretical study conducted by Nagler (1918) and physical modelling conducted by Yarnell (1934a,b), a classification of the flow regarding the changes in upstream and downstream water depth was described, the two types being subcritical and choked. Subcritical flow refers to a flow where there is negligible changes in the flow depths upstream and downstream of the obstacle. Choked flow refers to flow where there is a large change in water depth upstream and downstream of the flow obstacle and is characterized by a hydraulic jump downstream of the obstacle. Choked flows usually occur at higher Froude numbers (Qi et al., 2014).

The drag coefficient is typically associated with an object that is fully submerged in the fluid. Due to the changes in water depth that occur in choked flows, the drag coefficient does not accurately describe the loading of an obstacle in choked flows. This change in water depth results in a change in hydrostatic pressure upstream and downstream of the obstacle, illustrated in Figure 2.2. Therefore, the loading acting on an obstacle can be described as a summation of the drag force and the force due to the change in hydrostatic pressure upstream and downstream of the obstacle (Qi et al., 2014). This force is defined as the resistance force:

$$F_R = \frac{1}{2} C_D \rho_f B h u^2 + \frac{1}{2} C_H \rho_f g B \left(h_u^2 - h_d^2\right) \tag{2.4}$$

where C_H is the hydrostatic coefficient, h_u is the upstream flow depth, and h_d is the downstream flow depth. Due to the difficulties associated with defining the hydrostatic coefficient, a resistance coefficient is defined as (Chaplin and Teigen, 2003):

$$F_R = \frac{1}{2} C_R \rho_f B h u^2 \tag{2.5}$$

where C_R is the resistance coefficient. Similar to the drag coefficient, a greater resistance coefficient indicates the obstacle is less hydrodynamically-efficient.

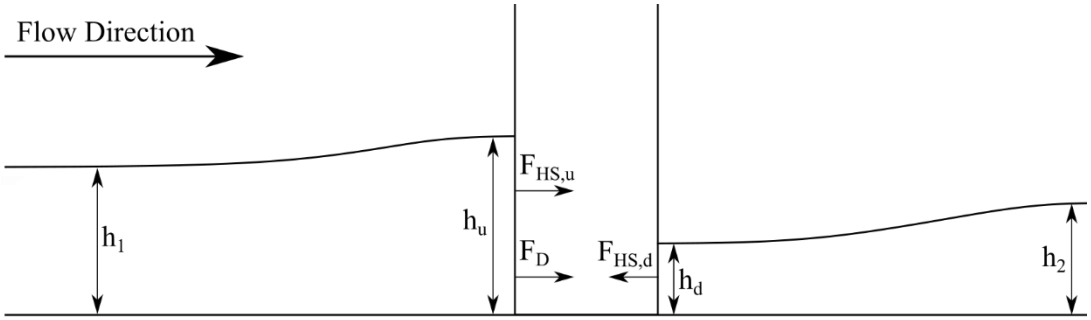

Figure 2.2: The side view of a column obstructing flow (adapted from Qi et al. (2014)). h_1 is the upstream water depth unaffected by the structure, h_2 is the far downstream water depth, $F_{HS,u}$ is the upstream hydrostatic force acting on the column, and $F_{HS,d}$ is the downstream hydrostatic force acting on the column.

Chaplin and Teigen (2003) investigated the flow behaviour surrounding a cylindrical surface-piercing obstacle. The runup on the front of the cylinder was analyzed and it was found that the runup increased with increasing Froude number. Hay (1947) also tested cylinders pulled in a tow tank at steady-state conditions. It was also found that the runup increased with Froude number. This study also measured the drawdown, which is the decrease in water depth downstream of the obstacle. The drawdown increased with increasing Froude number until the depression reached the elevation of the bottom of the cylinder and the whole rear face of the cylinder was exposed.

The fluid-structure interaction of a tsunami bore with a column has also been investigated. St-Germain et al. (2014) numerically investigated the flow behaviour of a dam-break wave travelling towards a square column using Smooth Particle Hydrodynamics (SPH). Derschum et al. (2017) compared the results of this study to experimental results, as illustrated in Figure 2.3. When the bore impacted the column, there was a significant amount of splash-up that occurred (Figure 2.3 (a)). The flow formed an area of reduced velocity directly in front of the column due to the blockage of the column. The flow travelling around the structure also had reduced velocity compared to when there was no structure present. The splash-up resulted in the formation of a surface roller to begin to form. The surface roller resulted in rotational motion upstream of the column, reducing the velocity in the surface roller. Eventually the surface roller began to propagate upstream (Figure 2.3 (d)).

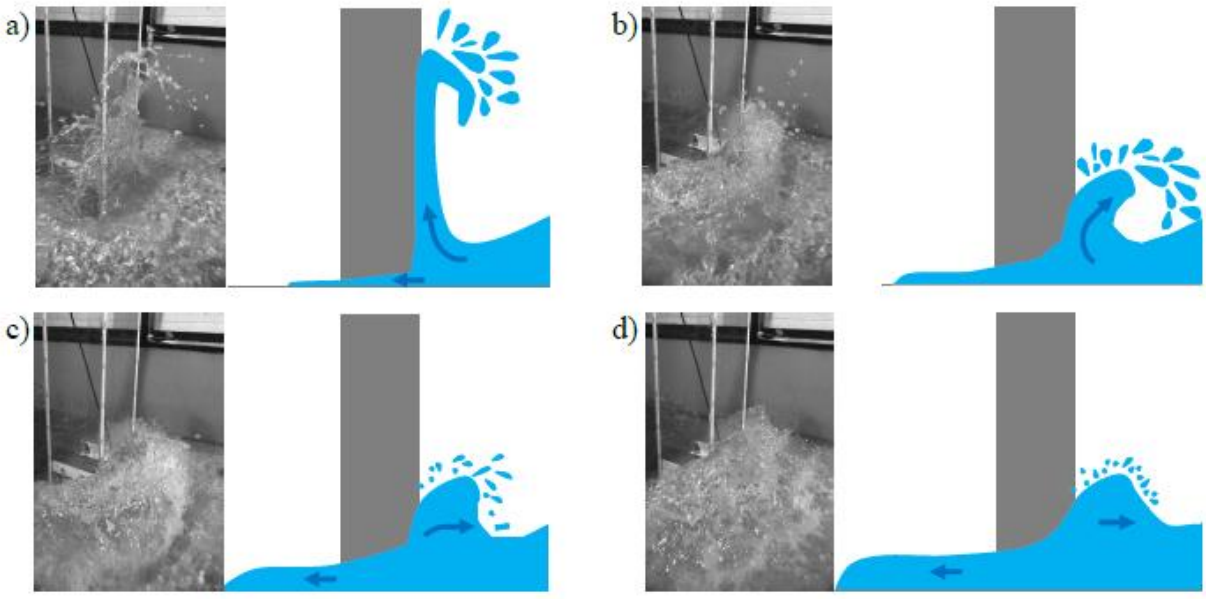

Figure 2.3: Fluid-structure interaction of a dam-break bore and a square column (adopted by Derschum et al. (2017)); a) initial splash-up of bore; (b) initial formation of the surface roller; (c) fully formed surface roller; (d) the surface roller propagating upstream.

2.2.3 Drag and Resistance Coefficient

The drag coefficient of flow obstacles has had a significant amount of research conducted in the field of fluid mechanics due to its wide range of applicability. The literature reviewed on this subject will mainly pertain to research relevant to the present study due to the large quantity of research conducted on this topic.

Chaplin and Teigen (2003) tested cylindrical columns towed at steady-state speeds to investigate the resistance coefficient in Froude numbers ranging from 0.5 to 1.6. It was found that the resistance coefficient is a function of the Reynolds number and the Froude number. The resistance coefficient was also compared for various elevations on the column. At lower Froude numbers, the resistance coefficient was essentially uniform for all elevations. At Froude numbers greater than 0.8, it was found that the resistance coefficient increases with increasing elevation until the resistance coefficient falls to 0 above the still water level. Similarly, Qi et al. (2014) determined the resistance coefficients of a square column tested in a range of Froude numbers in steady-state flow. It was found that the resistance coefficient was relatively constant for subcritical flow conditions and when the flow became choked, the resistance coefficient increased. This is likely due to the increased loading due to the changes in water depth upstream and downstream of the column. It was also found that the resistance coefficient was a function of the Froude number.

Arnason (2005) tested columns of varying size, shape, and orientation tested in dam-break waves of various impoundment depths. It was observed that the resistance coefficient was greater than the drag coefficient of fully submerged flow obstacles of the same size and shape tested in similar flow conditions. This is likely

due to the increased water depth upstream of the flow obstacle and the decreased water depth downstream of the flow obstacle, resulting in greater hydrostatic pressure acting in the flow direction. This study concluded that increasing impoundment depth resulted in a decrease in the resistance coefficient and that the resistance coefficient is a function of the Froude number and Reynolds number, as illustrated in Figure 2.4. In addition, the resistance coefficient increased with a decrease in the flow depth to column width ratio, as this resulted in greater flow redirection. The square columns had greater resistance coefficients in comparison to the cylindrical columns and greater resistance coefficients were observed when they were placed with the front face perpendicular to the flow.

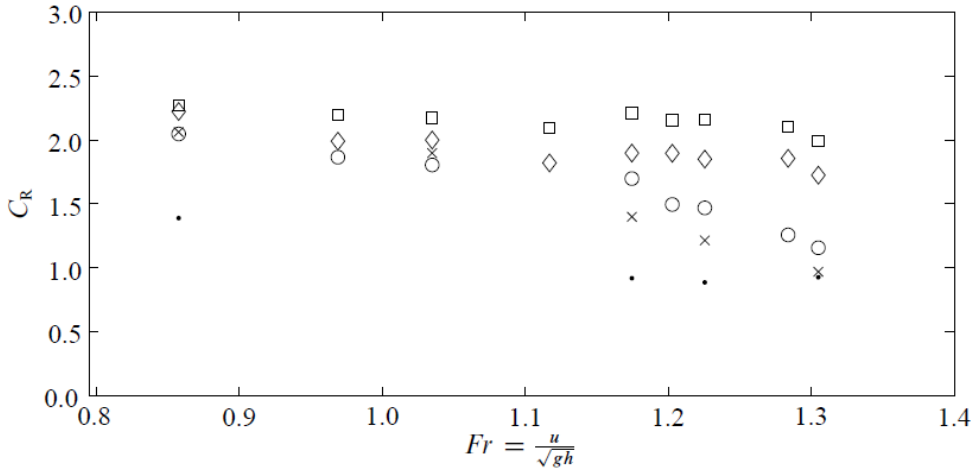

Figure 2.4: The resistance coefficients versus the Froude number of several columns (adopted from Arnason (2005)). □ and ◊ represent the square column with a side and corner facing the flow respectively, ○ represents the large cylinder, × represents the intermediate column and • represents the small one.

Asadollahi et al. (2018) conducted a similar study where a numerical model was utilized to investigate structural loading of flow obstacles in tsunami events. The columns were tested in dam-break waves of varying impoundment depths. This study concluded that increasing impoundment depths resulted in a decrease in the resistance coefficient. The orientation of the rectangular column affected the results; the greatest observed resistance coefficient occurred when the front face of the column was perpendicular to the oncoming flow. As the stream-wise length of the column to the width of the column increased, the resistance coefficient also increased. Similar to Arnason (2005), the resistance coefficients increased with a decrease in the flow depth to column width ratio.

2.3 Debris Transport

Naito et al. (2014) states that any rigid or deformable objects entrained in fluid flow can be classified as debris. The motion of debris is initiated when the flow hits debris' seaward face, transferring energy to the debris (Nistor et al., 2016). The modelling of debris motion has been challenging due to the large number

of variables influencing debris transport and due to its random nature. However, it has been shown that the process of debris transport is dependent on several parameters including the size of debris, gradient of land, flow depth, flow velocity, flow direction, and surrounding building layout (Naito et al., 2014).

Yao et al. (2014) conducted experiments to study debris motion in solitary waves. Polyethylene cubes were used to represent wooden houses in the experiments. The experiments were conducted in a wave flume that had a composite slope to represent a sloping beach. Yao et al. (2014) stated that debris would initiate movement with the flow when the drag force exceeds the friction force between the debris and the bed. When the debris are partially submerged and are still in contact with the bed, the debris will move slower than the flow. Once the debris are fully floating, they travel at a similar velocity to the water flow, assuming that there are no obstructions. When the flow began to reach the maximum inundation, the water depth decreased and the debris' velocity decreased in comparison to the flow velocity.

Imamura et al. (2008) conducted laboratory experiments to investigate the transport of boulders in tsunamis as the behaviour of floating and submerged debris varies significantly. A sloping water tank was used to simulate a shore. In the experiments, the bore was generated and proceeded up the slope until the maximum inundation length and then the flow retreated seaward. The debris were found to be transported by rolling and saltation rather than sliding. When the flow velocity decreased, the debris began to be transported by sliding. The debris were then moved seaward with the retreating flow and primarily were transported by sliding. The maximum displacement and maximum final positions were observed with greater flow velocities. Two different debris boulders were tested of varying mass. The displacement in the experiments overall was greater for the boulders with less mass when compared to a denser boulder of the same volume. Therefore, lighter debris will typically travel greater distances relative to heavier debris of the same volume. This conclusion can only be applied to submerged debris due to the varying characteristics of submerged and floating debris.

An experimental campaign conducted by Rueben et al. (2015) was performed in a tsunami wave basin. The waves were generated with a piston-type wave maker. The debris specimens were wooden boxes constructed from plywood. The boxes were scaled to 12 metres, the approximate length of a standard shipping container. One box was loaded with concrete slabs and was used as a stationary specimen to create an obstacle for other debris. It was observed that the motion of the debris in the onshore direction was similar for several trials until the stall point, the point at which the velocity of the debris are zero. The horizontal velocity was also compared and it showed that the onshore movement had similar velocity whereas the offshore velocity varied. Therefore, it can be concluded that onshore motion is repeatable, whereas offshore motion has more variance associated with it.

2.4 Debris Dam Formation

There has not been a significant amount of research conducted on debris dams in extreme flooding events, however, there has been substantial work done in the field of river engineering due to the large amount of woody debris observed in fluvial systems. Experiments were conducted by Bocchiola et al. (2008) using wooden dowels to model woody debris to investigate the process of debris dam formation. The wooden dowels were placed upstream of obstacles present in the flume. The first dowel to become trapped by the obstacle, resulted in the initiation of debris dam formation, and was characterized as the "key" log. The formation of the debris dam causes streamlines of flow to change direction around the debris, which initiates the debris to span the flume, increasing the width of the dam (Schmocker and Hager, 2011). This increase in width results in an increase in flow velocity, pushing the debris towards the bottom of the flume and increasing the depth of the debris dam. This process increases the blockage, resulting in an increase in the backwater rise and a decrease in velocity. Eventually this decrease in velocity results in an increase in the length of the dam. The process of debris dam formation is highlighted in Figure 2.5 by Stolle et al. (2017).

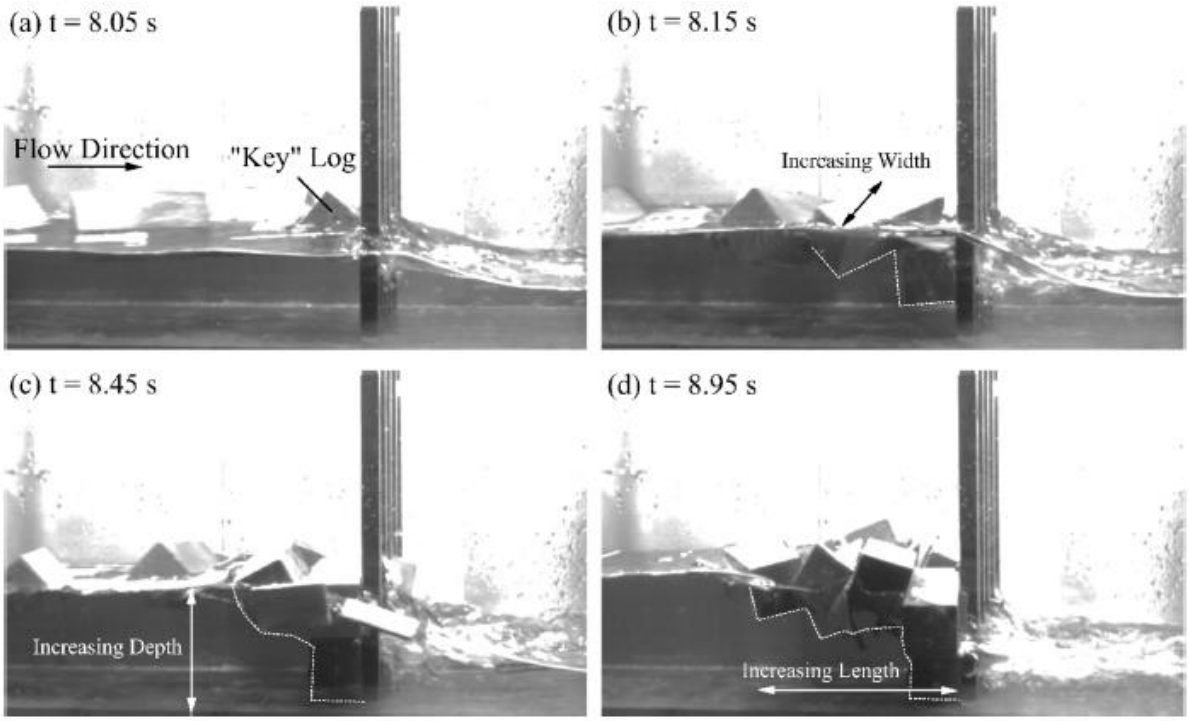

Figure 2.5: The process of debris dam formation; (a) initial capture of the key log; (b) increasing width of the debris dam; (c) increasing depth of debris dam; (d) increasing length of debris dam (adopted from Stolle et al., 2017).

Stolle et al. (2017, 2018a) examined the influence of individual debris geometry and size on debris dam formation. The obstacle utilized in these experiments was a set of columns. The experiments utilized scaled-down shipping containers, poles, and boards, which were tested in in steady-state and transient flow

conditions, respectively. Stolle et al. (2017, 2018a) compared the capture rate, which is defined as the percentage of debris captured, of each debris type. Larger debris resulted in greater capture rates relative to the smaller debris. Schmocker and Hager (2011) analyzed the probability of debris blockage occurring in river systems based on varying parameters, including debris size, flow velocity, and water depth. The research concluded that the probability of blocking increased when the distance between the water surface and bridge decreased and when the size of the debris increased. The research also illustrated that the probability of blocking also decreases when the Froude number increases. Schmocker and Hager (2011) state that this is likely because the debris are more easily freed at higher flow velocity. The blocking probability is also greater for rougher bridges compared to smooth bridges. Through laboratory investigations, Lyn et al. (2003) found that the depth had a large impact on debris accumulation. Shallower channels allow debris to come in contact with the bed, which increases the stability of debris accumulations. Lyn et al. (2003) suggests that the ratio between log lengths to local depth is a parameter than can be used to analyze debris accumulation potential. Similarly, when Pasha and Tanaka (2016) studied the capture efficiency of debris on inland forests in tsunami events, it was found that the capture efficiency increased with increasing debris length and decreasing flow velocity.

Stolle et al. (2017) observed an increase in dam size with an increase in debris volume, as expected. In some cases, the depth of debris was greater than the original water depth, due to the backwater rise as a result of the blockage. The length of the debris dam was greater at lower flow velocities as high flow velocities cause the dam to compact. Similarly, trials with high flow velocities resulted in deeper dams due to compaction. The width of the dam was related to the amount of debris supplied, however, the width was limited to the width of the flume. Stolle et al. (2017) observed that trials with the smaller debris formed deeper dams because the debris have less contact area with the obstacle, causing instability. Stolle et al. (2018a) conducted a similar experimental campaign as Stolle et al. (2017), conducted in transient flow conditions utilizing a dam-break wave. The process of debris dam formation was similar in both sets of flow conditions, however, there were some discrepancies in the dam formation relative to the steady-state experiments. The transient flow conditions resulted in a more compact and narrow dam relative to the dams observed in steady-state flow conditions. This is likely attributed to the violent, turbulent flow observed in transient flow conditions.

A photographic archive of various woody debris accumulations at bridge piers was developed by several different contributors throughout the United States to analyze debris prone bridges. Zevenbergen et al. (2006) analyzed this archive to determine the main geometry profiles of accumulated debris. The analysis of the archive determined two main geometric accumulations, triangular and rectangular. Zevenbergen et al. (2006) also observed a third geometric profile, which was the inverted conical profile. This accumulation

tends to occur after several floods when a triangular accumulation settles to the bed of the river. A fourth profile, the buried wedge, was also observed and tends to occur when an accumulation becomes embedded in the bed of a river channel.

The majority of debris observed in river systems are floating debris, meaning the debris accumulates at the water's surface (Diehl, 1997). Therefore, many laboratory investigations conducted related to woody debris considers debris dams as floating rafts, however, it has been observed that the height of the woody debris accumulation can grow vertically when debris are washed underneath the present accumulation. Based on experiments conducted by Parola et al. (2000), it was concluded that woody debris accumulations can develop to the bottom of the flow depth. Zevenbergen et al. (2006) analyzed the photographic archive of woody debris accumulations at bridge piers and also concluded that debris accumulations could grow and become fully submerged or partially submerged.

2.5 The Impacts of Debris Damming

Many recent extreme flooding events have highlighted the uncertainty in structural design due to unexpected failures or damage to infrastructure (Yeh et al., 2014). Previously, structures have been designed for the hydrostatic and hydrodynamic loads associated with tsunamis, while the impacts of debris have been ignored. Research has been conducted regarding debris impact loads in extreme flooding events (Haenal and Daly, 2002; Paczkowski et al., 2012; Naito et al., 2014), but there has been little research conducted on loading due to debris damming. The failure of structures, particularly reinforced concrete structures, has highlighted the need for a better understanding of the effect of debris dams on loading and surrounding flow conditions (Yeh et al., 2014).

2.5.1 Debris Dams' Impacts on the Flow Field

Pagliara and Carnacina (2013) analyzed the flow field surrounding debris accumulated on a bridge pier through physical modeling. Four different types of debris dams were attached to a bridge pier and tested. The debris varied in roughness but all debris had a constant frontal area. The research found that debris results in a decrease in the flow area, increasing the flow velocity. The debris also causes a boundary layer to form underneath the debris. This boundary layer contributes to an additional reduction of the flow area, resulting in greater increases in velocity. The size of the boundary layer increased as the roughness of debris increased. This boundary layer also causes the velocity profile to shift towards the bed. The shift in the velocity profile increases the shear stress, resulting in an increase of scour. The debris dams also affect the flow field by changing the average direction of the flow. When debris were present, the flow field had a greater maximum vertical velocity compared to when there was no debris present. The increase in downward vertical velocity results in an increase of scour and increases of upward vertical velocity can

create greater lift forces. The effects of debris on the flow field surrounding a column is illustrated in Figure 2.6.

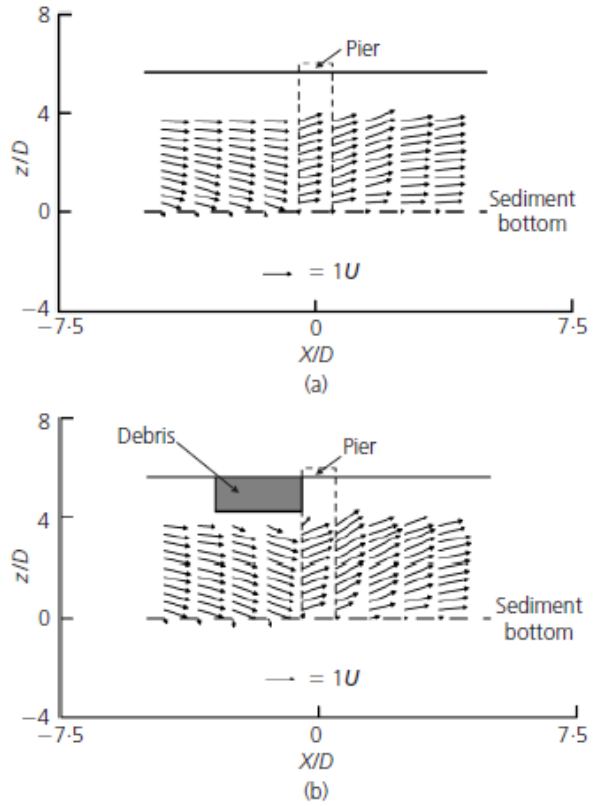

Figure 2.6: Changes in the flow field due to debris, where X is the longitudinal coordinate, z is the vertical coordinate, D is the pier diameter, and U is the velocity (adopted from Pagliara and Carnacina (2013)).

Lagasse et al. (2010) conducted experiments to assess the impact of various woody debris dam geometries on the flow field. The experiments tested two different debris dam shapes, rectangular floating debris and triangular floating debris, with a variety of length, width, and height. The accumulations were attached to a bridge pier. The flow field surrounding the bridge pier and debris differed depending on the type of debris. The flow lines observed for the isolated bridge pier descend down the front face of the pier and then bend around the pier forming a horseshoe vortex pattern, a widely known process associated with flow obstructions. The rectangular debris dams caused the flow to have greater obstruction relative to when only the column was present. This results in the flow to descend when interacting with the debris, which is shown in Figure 2.7 (a). This created an upstream scour trough that was observed in all experiments conducted with rectangular debris. The flow lines still descend down the front face of the pier and then bends around the pier forming the horseshoe vortex like the unobstructured pier, however, the magnitude of the downward flow is greater. A rise in the water level can also be observed upstream of the debris due to the decrease in

flow area. The triangular debris dam was also investigated, as this is a common shape of debris accumulation observed in field surveys (Zevenbergen et al., 2006). The triangular debris dam had greater width at the pier, decreasing upstream of the pier, which is a common configuration of triangular debris accumulations. The scour observed in these experiments varied from the shape of the scour with rectangular debris. No upstream scour troughs formed with triangular debris. The triangular debris caused the flow to plunge downwards creating larger scour when compared to the unobstructed pier.

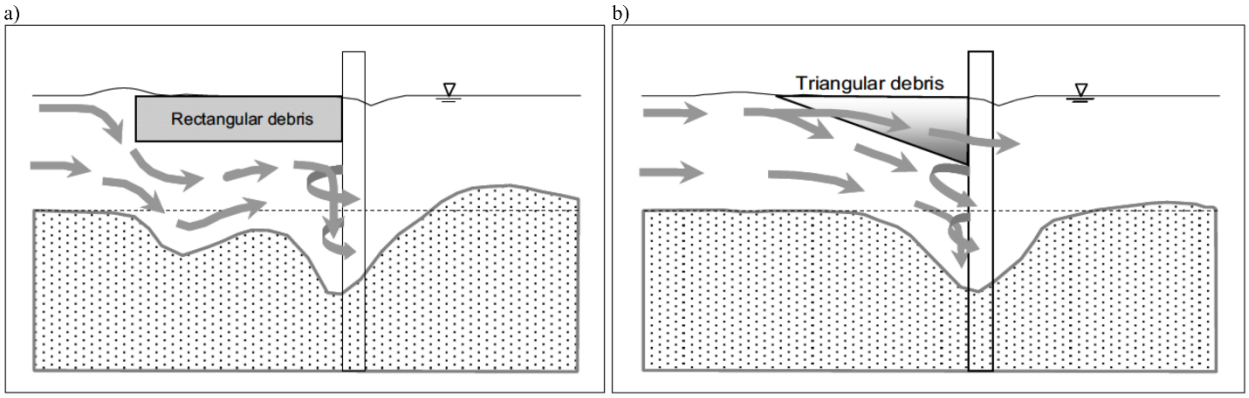

Figure 2.7: Flow lines at the bridge pier with (a) rectangular debris dam; (b) triangular debris dam (adopted from Lagasse et al. (2010)).

Schmocker and Hager (2013) investigated the backwater rise due to woody debris. Scaled logs were released in the flume and accumulated on a set of column obstacles. This study illustrated that the backwater rise increased with time until the debris dam stabilized. It was observed that greater dam volume resulted in greater backwater rise. The backwater rise also increased with increasing Froude number. Similarly, Stolle et al. (2017) analyzed the backwater rise and it was concluded that the backwater rise increased with an increasing Froude number and an increase in debris dam size. Stolle et al. (2018a) studied the runup of debris accumulated on a set of columns tested in a dam-break wave. It was found that the runup was proportional to the Froude number.

2.5.2 Debris Damming Loads

Until recently, there was no consistent set of guidelines or standards prescribed in mandatory language regarding the design of structures in extreme flooding events. The American Society of Civil Engineers (ASCE) published the Chapter 6: Tsunami Loads and Effects in the ASCE 7-16. This chapter provides standards for the design of critical structures in tsunami events. The ASCE considers four main loads regarding tsunami events: hydrostatic forces, hydrodynamic forces, debris impact forces, and scour effects (Chock, 2016). Debris damming loads are included within hydrodynamic forces, however, the loading due to debris damming needs to be considered in greater depth (Chock, 2015).

The formation of debris dams creates an increased drag force on structures due to the increased area exposed to the flow. The hydrodynamic loading acting on the debris dams is then transferred to the structure or surrounding structures that the debris have accumulated on. The drag force due to debris damming can be calculated using the typical drag force equation, listed in Equation (2.3) (FEMA, 2012).

Panici and Almeida (2018) experimentally investigated the formation of woody debris accumulations on a single bridge pier testing individual woody debris objects. The loading due to the debris accumulations on the pier were recorded and compared to the dam formation and stability, as illustrated in Figure 2.8. It was found that the drag force increases exponentially during the unstable phase of debris dam growth and oscillations of the drag force are observed during this period. Once stable debris dam formation occurs, the drag force stabilizes and reaches a maximum force value. When the debris dam is on the brink of failure, there will be a decrease in the drag force. The drag force will then abruptly be reduced in the event of dam failure.

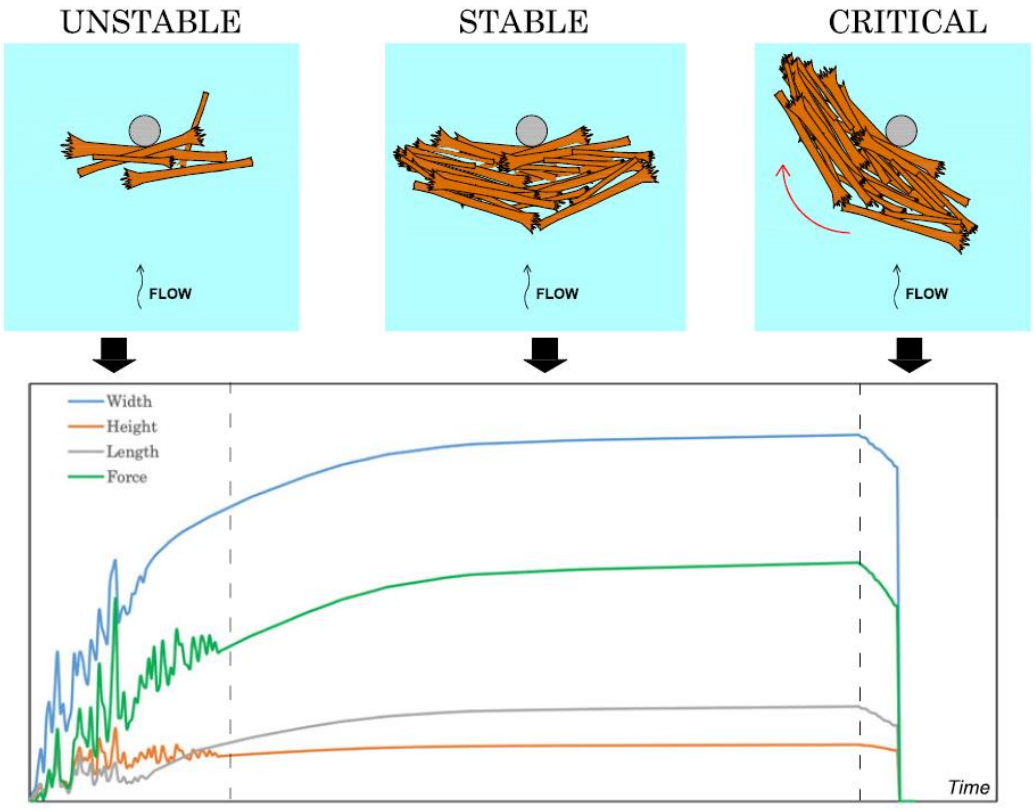

Figure 2.8: Sketch of the three growth phases of debris dams (top). Plot of growth and force of debris dams with time (bottom) (adopted from Panici and Almeida (2018)).

Parola et al. (2000) conducted a series of experiments to predict the drag force due to debris dams based on the blockage ratio and the Froude number. The experiments were conducted using woody debris

accumulating on various bridge piers. The experiments were conducted using woody debris with a variety of blockage ratios and Froude numbers. Predictions for drag coefficients were obtained for the debris dams accumulated on the bridge piers. It was concluded that as the Froude number increases, it results in a decrease in the drag coefficient. It was also found that greater blockage ratios result in lesser drag coefficients.

Stolle et al. (2017) assessed the drag force due to varying dam formations using different debris tested in steady-state flow conditions. The various amount and type of debris resulted in differing force-time histories. The force-time history was also not repeatable for all dam formations, due to the random nature of debris dam formation. It was expected the drag force would increase with an increase in blockage, as the debris dam area is a function of the blockage ratio, however, this was not observed in the experiments conducted. Stolle et al. (2017) states that these unexpected results are likely due to increased backwater rise caused by the increase in blockage. As the backwater rise increases, the flow velocity decreases. The drag force is directly proportional to the dam width and the squared velocity, resulting in counteracting influences of the two properties. The drag coefficient was also determined for the tests. The drag coefficient was found to decrease with blockage until a blockage of 0.46. Blockages greater than 0.46 resulted in a relatively constant drag coefficient.

Stolle et al. (2018a) conducted a similar investigation on debris damming formation and loads in tsunami waves. Contrary to the results of the steady-state experiments conducted by Stolle et al. (2017), the debris dams consisting of debris with high surface area to volume ratios resulted in a decrease in loading. This is likely due to the high surface area to volume ratios resulting in less stable dams and for less debris to be captured. This study also showed that the presence of debris resulted in an earlier occurrence of the maximum force relative to when there was no debris present. The resistance force coefficient was also calculated in this study. The resistance coefficient displayed a log-log linear relationship with the product of the Reynolds and Froude number. This research highlighted the uncertainty regarding the voids or porosity of the debris dams. Stolle et al. (2018a) assumed the debris dams to be nonporous when calculating the resistance coefficient due to the difficulties associated with determining the porosity of the dams. It was stated that this might be the cause of discrepancies in the relationship of the resistance coefficient.

2.6 Discussion

The presented literature review summarizes the most current research relating to flow obstacles, debris motion, debris dam formation, and debris damming loads. There are still several uncertainties relating to these processes, highlighting the need for further research on this topic. Based on the literature review conducted, the following are important to consider in terms of modelling debris damming loads:

- Froude similitude is best suited to scale physical models representing surface piercing obstacles in open channel flow (Chanson, 2004).
- The use of the dam-break wave to model on-land tsunami bores is suitable due to its similarity to a tsunami wave propagating over a coastal plain (Chanson, 2006).
- Changes in water depth associated with flow obstacles tested in relatively high Froude numbers result in increased hydrostatic forces acting in the flow direction. Therefore, the drag coefficient should not be applied but rather the resistance coefficient, which encompasses both forces caused by drag and hydrostatic pressure (Qi et al., 2014).
- The drag and resistance coefficient are not only a function of the shape of the flow obstacle, but also the surrounding flow conditions, the obstacle length to width ratio of the flow obstacle, and the flow depth to obstacle width ratio (Chaplin and Teigen, 2003; Arnason, 2005; Asadollahi et al., 2018).
- Debris transport and debris dam formation are random processes; however, in some cases, these processes are repeatable. Debris transport and debris dam formation are a function of debris size, surrounding flow obstacles, and flow conditions (Schmocker and Hager, 2011; Rueben et al., 2015; Stolle et al., 2017).
- Debris dams result in increased obstruction of the flow channel, resulting in increased drag forces acting on adjacent structures (Parola et al., 2000; Stolle et al., 2017). In addition, debris dams increase the magnitude of vertical flow velocities, resulting in greater scour, and increased water depths upstream of structures, resulting in overtopping (Pagliara and Carnacina, 2013; Schmocker and Hager, 2013).
- The loading due to debris damming is a function of roughness, debris dam size, debris dam geometry, the Froude number, and the Reynolds number (Parola et al., 2000; Stolle et al., 2017; Stolle et al., 2018a).
- As Froude similitude is best suited to scale open channel flow and debris damming loads are a function of the Reynolds number, special care must be implemented to ensure minimal impacts due to scaling. For steady-state flow, it is recommended that a Reynolds number greater than 1.25×10^4 be achieved, as this is when fully turbulent flow occurs (Chow, 1959). A Weber number greater than 100 is also suggested, to avoid surface tension influences (Peakall and Warburton, 1996). In addition, when generating a dam break wave, the impoundment depth should be greater than 0.30 m for scaling using Froude similitude (Lauber and Hager, 1996).

To further aid in the design of flood resistant structures, further research is required regarding debris damming loads. Based on the literature review conducted, the present study will focus on the following gaps in research:

- Little research has been conducted regarding the loading due to debris damming. The research that has been conducted on debris damming has been primarily conducted in the field of river engineering, meaning it was conducted in steady-state flow conditions in a lower range of Froude numbers. Further research relating to debris damming in extreme flooding events is required. Therefore, this *study will complete tests conducted in higher Froude numbers and in transient flow conditions*.
- Due to the complex geometry and the variability of debris dams, it is difficult to analyze how the size and porosity of debris dams influence the loading due to debris. Therefore, *this research aims to investigate how the dam shape, height, and porosity affect the loading due to debris*.
- Furthermore, *the surrounding flow conditions of the debris dams will be investigated* as little research has been conducted on how the geometry of the debris dam influences backwater rise and downstream depressions in the flow.
- In design standards, such as the FEMA P-646 (2012), it is recommended to estimate debris damming loads using the typical drag force equation. Little research has been conducted regarding the drag coefficient of debris dams, particularly in extreme flooding conditions. Therefore, *this research will investigate how varying flow conditions and debris dam geometry influence the drag/ resistance coefficients*.

Chapter 3. Experimental investigation of loading due to debris dams on structures

3.1 Introduction

Extreme storm surges and tsunamis can lead to significant loss of life and destruction of coastal communities. Many recent events, including the 2004 Indian Ocean Tsunami, the 2005 Hurricane Katrina, and the 2011 Tōhoku Tsunami, have resulted in unexpected damage or failure to infrastructure. These events demonstrated the need for improved structural design guidelines (Yeh et al., 2013; Nistor et al., 2017). Until recently, there were no consistent sets of guidelines or standards used for the design of critical infrastructure in extreme flooding events. Recently, the American Society of Civil Engineers (ASCE) published the Chapter 6: Tsunami Loads and Effects in the ASCE 7-16 (Chock, 2016). This chapter prescribes, in mandatory language, how to design against tsunami hydrodynamic loading and the subsequent loading due to debris entrained within tsunami-induced coastal inundation. This standard is a step towards novel structural design procedures against tsunamis effects; however, the loading due to accumulations of debris on structures requires a more comprehensive review (Chock, 2015).

Debris entrained by storm surges or tsunami-induced inundation can form accumulations in-between or in front of structures, which is a process commonly referred to as *debris damming* (Yeh et al., 2014). Debris dams increase loading on structures due to an enlarged cross-sectional area exposed to the incoming flow. Debris dams have also been known to result in convective flow accelerations, an increase in the magnitude of vertical velocities, as well as an increase in the horizontal velocity gradient; all which result in increased scour of the soil surrounding the foundation of structures (Melville and Dongol, 1992; Pagliara and Carnacina, 2011). Increased flow depths upstream of structures have also been observed due to increased flow obstruction: such increases of the water level can cause overtopping of the structure (Schmocker and Hager, 2013; Stolle et al., 2017).

The loading due to debris damming is typically considered in design prescriptions as a quasi-steady force. The drag force equation can be used to estimate loading due to debris damming (FEMA, 2012):

$$F_D = \frac{1}{2} C_D \rho_f B h u^2 \qquad (3.1)$$

where ρ_f is the density of the fluid, C_D is the drag coefficient, B is the cross-stream width of the debris dam, h is the water depth, and u is the flow velocity.

Limited research has been conducted on loading due to debris dams in extreme flooding events where transient conditions prevail. However, substantial work has been performed in the field of river engineering due to woody debris commonly observed in fluvial systems. Parola et al. (2000) reported on the increased loading due to debris accumulations on highway bridges. These authors concluded that the drag coefficient varies with the blockage ratio of the channel (the ratio of the area of flow obstruction to the area of the channel). Their study also found that the drag coefficient is a function of the Froude number.

Qi et al. (2014) studied the obstruction of a rigid rectangular column in free surface channelized flow. A one-dimensional model was developed to analyze the relationship between the forces acting on the column and the changes in the free surface. Two main types of flows were analyzed: subcritical and choked flows. For subcritical flows, there were negligible changes in the water depth upstream and downstream of the column. Choked flows are characterized by a significant increase in the water depth upstream of the column and a decrease in the water depth downstream of the column (Qi et al., 2014), as illustrated in Figure 3.1. This increase in water depth upstream of the column is known as backwater rise (El-Alfy, 2006). Changes in water depth upstream and downstream of a column were shown to be proporational to the flow velocity (Fenton, 2003; Qi et al., 2014). The change in water depth in choked flow conditions results in an increase in the hydrostatic force acting on the column in the flow direction. The resistance force is estimated as the sum of the form drag force due to the flow obstruction and the increased hydrostatic force due to the change in water depth directly in front of and behind the column:

$$F_R = \frac{1}{2} C_D \rho_f B h u^2 + \frac{1}{2} C_H \rho_f g B \left(h_u^2 - h_d^2\right) \tag{3.2}$$

where C_H is the hydrostatic coefficient, h_u is the water depth upstream of the column, and h_d is the water depth directly downstream of the column. Chaplin and Teigen (2003) defined a total resistance coefficient for the force acting on a column due to flow obstruction. The resistance force was defined as:

$$F_R = \frac{1}{2} C_R \rho_f B h u^2 \tag{3.3}$$

where C_R is the resistance coefficient. The resistance coefficient is a dimensionless value used to quantify flow resistance. Similar to the drag coefficient, a less hydrodynamically-efficient obstacle would exhibit a greater resistance coefficient. Chaplin and Teigen (2003) concluded that the resistance coefficient is also a function of the Froude number.

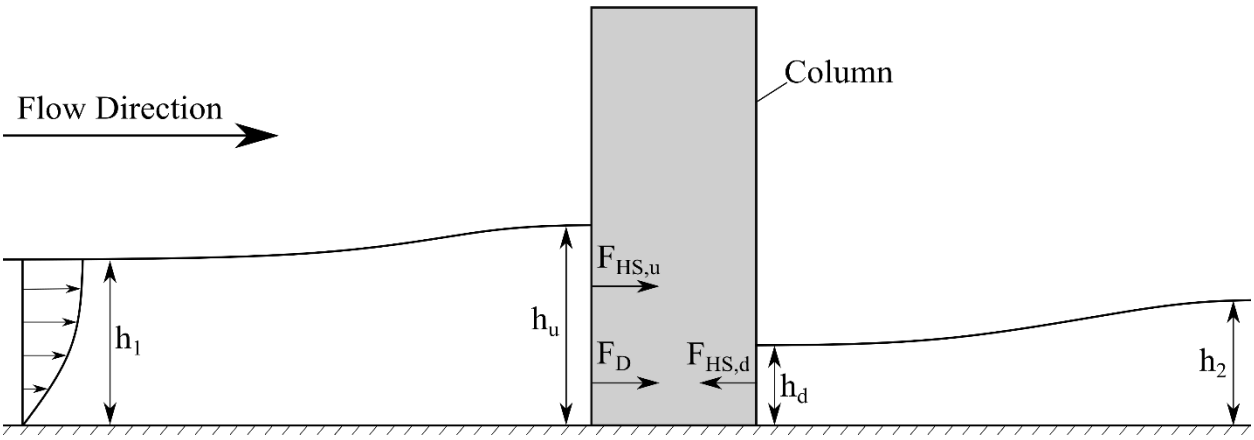

Figure 3.1: The side view of a column obstructing flow (adapted from Qi et al., 2014), where h_1 is the upstream water depth unaffected by the structure, h_2 is the far downstream water depth, h_u is the water depth directly upstream of the column, h_d is the water depth directly downstream water depth, $F_{HS,u}$ is the upstream hydrostatic force acting on the column, and $F_{HS,d}$ is the downstream hydrostatic force acting on the column.

Debris dam formation can be considered a random process during which independently moving debris congregate and their agglomeration/ accumulation commences relatively unpredictable. However, there are several patterns during the debris dam formation that can be observed. Debris dam formation is affected by several parameters including debris size, debris geometry, flow velocity, and channel size (Schmocker and Hager, 2011). Stolle et al. (2017) examined the impact of debris geometry and debris composition on the formation of debris dams and observed an increase in dam size with an increase in the individual debris volume. Tests with higher flow velocities resulted in dams of greater length and depth due to the higher velocities causing compaction. The width of the dam was related to the amount of debris supplied. Stolle et al. (2017) observed that tests with debris types of lesser surface area formed deeper dams since they had less contact area with the obstacle, thus causing instability. Bocchiola et al. (2008) tested the accumulation of logs with varying sizes and also found that the probability of a log to become jammed increased with increasing length and diameter of logs. Schmocker and Hager (2011) analyzed the probability of debris blockage occurring on bridge decks based on varying parameters, such as the debris size, flow velocity, and water depth. Their study found that the probability of blocking decreased with an increase in the Froude numbers. Schmocker and Hager (2011) state that this is likely because the debris are more easily re-entrained at higher flow velocity.

There is still uncertainty regarding the geometry of debris dams. Based on experiments conducted using woody debris, Parola et al. (2000) concluded that debris accumulations can develop to the bottom of the flow depth, despite previous researchers considering them as floating rafts (Diehl, 1997). Zevenbergen et al. (2007) analyzed a photographic archive of woody debris accumulations at bridge piers in the United States and concluded that debris accumulations could grow and become fully submerged or partially

submerged. The study also found that debris accumulations typically formed in two main shapes: rectangular or triangular.

Previous research on debris damming has primarily focused on the formation of debris dams. Little attention has been focused on the loading conditions of structures adjacent to debris dams. Understanding the loading exerted on vertical structures as well as providing stipulations in guidelines and building design codes is paramount for adequate design in hazard-prone regions. The research that has been conducted on the loading due to debris dams primarily focused on bridge piers in rivers/ channels. There are several challenges related to assessing the effects of debris dam loads post-disaster, including the disintegration of debris dams with retreating flow and several uncertainties related to surveying flood events. Therefore, experimental investigations are required to develop a further understanding of this process and associated effects under such complex hydrodynamic conditions.

This study examines the impacts of debris damming through the use of idealized, fixed debris dams attached to a column in steady-state flow conditions. This research will provide further understanding of how the debris dam geometry affects structural loading conditions and will eventually aid in formulating recommendations for future design guidelines. To the authors' knowledge, this study is the first attempt to address debris dam properties subjected to flow conditions based on idealized dam conditions. Several debris dam parameters were investigated, including porosity, relative dam height, and dam shape. The debris dams were tested with various Froude numbers as the resistance coefficient is typically evaluated as a function of the Froude number (Chaplin and Teigen, 2003; Arnason, 2005). The ultimate aim of this study is to help develop engineering guidelines and recommendations for the design of critical infrastructure against loading due to debris damming. The objectives of this study are:

- To examine the influence of debris dam porosity, height, and shape on induced loads.
- To investigate the resistance coefficient due to debris damming in terms of Froude number and debris dam geometry.
- To evaluate the effect of debris dam geometries on the surrounding flow conditions.

The use of idealized debris dams, strategically used in this study, allows for the isolation of debris dam variables such as their height relative to the water surface and its porosity. Using first steady-state conditions is hence fundamental to understand the flow-structure interaction, prior to focusing on transient conditions often found in extreme flows. Transient flow conditions are currently investigated by the authors in a separate study. This research project will provide further understanding regarding the impacts of debris dams' characteristics on changes to the free water surface and associated loading and ultimately aid in the

design of flood resistant-structures. The units of measure utilized throughout this paper are those currently used by the International System of Units (SI).

3.2 Methodology

3.2.1 Experimental Facility

The experimental program was performed in the Hydraulic Flume at the University of Ottawa, Canada. As illustrated in Figure 3.2, the flume is 30.0 m long, 1.5 m wide, and 1.0 m deep. The flume has two flow straighteners upstream of the testing area to ensure flow uniformity. The experimental setup was placed on a 0.30 m false floor and consisted of a smooth acrylic cylinder that represents a column and which was suspended from a bridge resting on the side walls of the flume. Various types of idealized debris dams were fixed to the column using a collar, representing the debris dam.

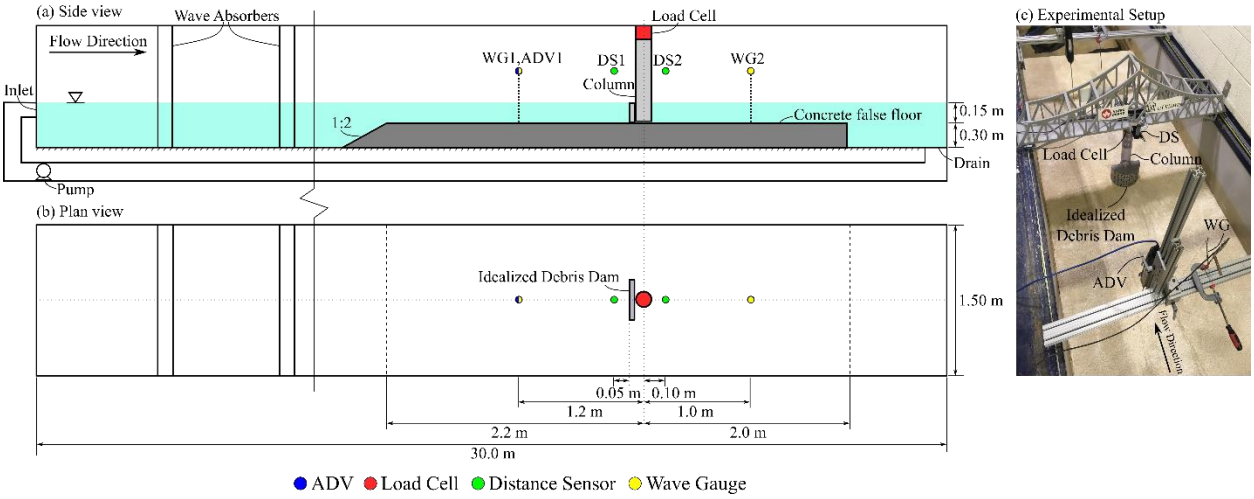

Figure 3.2: The hydraulic flume used for the experimental program: (a) side view of the flume; (b) plan view of the flume; (c) the experimental setup.

3.2.2 Instrumentation

Various instruments recorded the experimental data, which were employed to analyze the flow conditions and forces acting on the column. Details regarding the instruments used are listed in Table 3.1. Wave gauges were used to measure the water depth at four locations, as illustrated in Figure 3.2. Two types of wave gauges were used: ultrasonic distance sensors (DS) and capacitance wave gauges (WG). WG1 and WG2 were located 1.2 m and 1.0 m upstream and downstream of the column, respectively. DS1 was located 0.05 m upstream of the obstacle while DS2 was located 0.10 m downstream of the column. The ultrasonic distance sensors were placed as close to the debris dams and column as possible without any interference from the dams and column.

Table 3.1: Instrumentation used in experimental test program.

Instrument	Model	Sampling Rate (Hz)	Accuracy (±, %)	Instrument designation
MasaSonic PulStar Ultrasonic Distance Sensor (DS)	M-5000/ 220	300	0.25	DS1, DS2
Wave Height Gauge (WG)	WG-50	300	0.4	WG1, WG2
6-Axis Multi-Axis Load Cell by Interface	6A68	300	0.1	Load Cell
Acoustic Doppler Velocimeter (ADV)	Vectrino	100	0.5	ADV
Data Acquisition System (DAQ)	QuantumX MX440B and MX840B	-	-	-

A 6-axis load cell recorded the time history of the forces acting on the column. The load cell was attached to the top of the column and connected to a rigid mounting bridge. The time histories of the force and the water depth were recorded using a data acquisition system, while ensuring that all instruments were properly synchronized. The data from the load cell was filtered using a time-varied Empirical Mode Decomposition (EMD) filter. Huang et al. (1998) developed the EMD method and Li et al. (2017) then improved upon it by applying a time-varied approach, which was shown to be more robust in terms of signal noise removal. This method decomposes the input signal into a series of signal components, which allows for noise removal of the components. The filter removes signal noise from the time history of the force data by using a zero crossing method. This method splits the signal into several oscillations based on local extrema, which are known as mode functions. The filter then eliminates oscillatory terms based on the separation between modes, established by an assigned bandwidth. This filter is beneficial due to its ability to work well with non-stationary data, which characterizes the force-time history recordings. It was checked manually that the filtered signal contained the essential information recorded by the instruments, with no significant changes other than removing noise.

The Vectrino ADV recorded flow velocities upstream of the column once the flow reached an equilibrium state. Measurements were taken at six points located above the bottom of the flume bed to obtain an adequate velocity profile. These points were set at 0.005, 0.01, 0.015, 0.03, 0.04, and 0.07 m from the

bottom of the bed. The sampling length of the Vectrino ADV used in the experiments was 7 mm. The ADV data was filtered to remove noise using a filter developed by Rennie and Hay (2010). The filter utilizes a despiking algorithm to remove spikes from the velocity data and provides a time averaged velocity value at each point of measurement.

3.2.3 Hydrodynamics

Steady-state flow conditions were utilized in this study to evaluate the impacts of debris damming in uniform flow conditions. Each debris dam was tested in three various flow rates. A constant water depth (*d*) was used in the experiments of 0.15 m. The standard deviations for water depth was 0.011 m. The velocity profiles for the three flow rates in the stream-wise, cross-stream, and vertical directions were plotted against the depth of the channel, as shown in Figure 3.3. The maximum root mean square deviation of the flow velocities recorded with no dam present was 0.12 m/s and the mean root mean square deviation was 0.05 m/s. The flow is free of lateral influence and vertical accelerations, as illustrated in Figure 3.3 (b) and (c). The free stream velocity was calculated for the three corresponding flow rates with no obstacles present, which were 0.74, 0.69, and 0.45 m/s. The free stream velocities were calculated using a depth-averaged mean of the six stream-wise velocity measurements at the various depths. The free stream velocity was used in most of the calculations in this study (unless otherwise indicated) to ensure that the flow obstruction did not influence the upstream velocity.

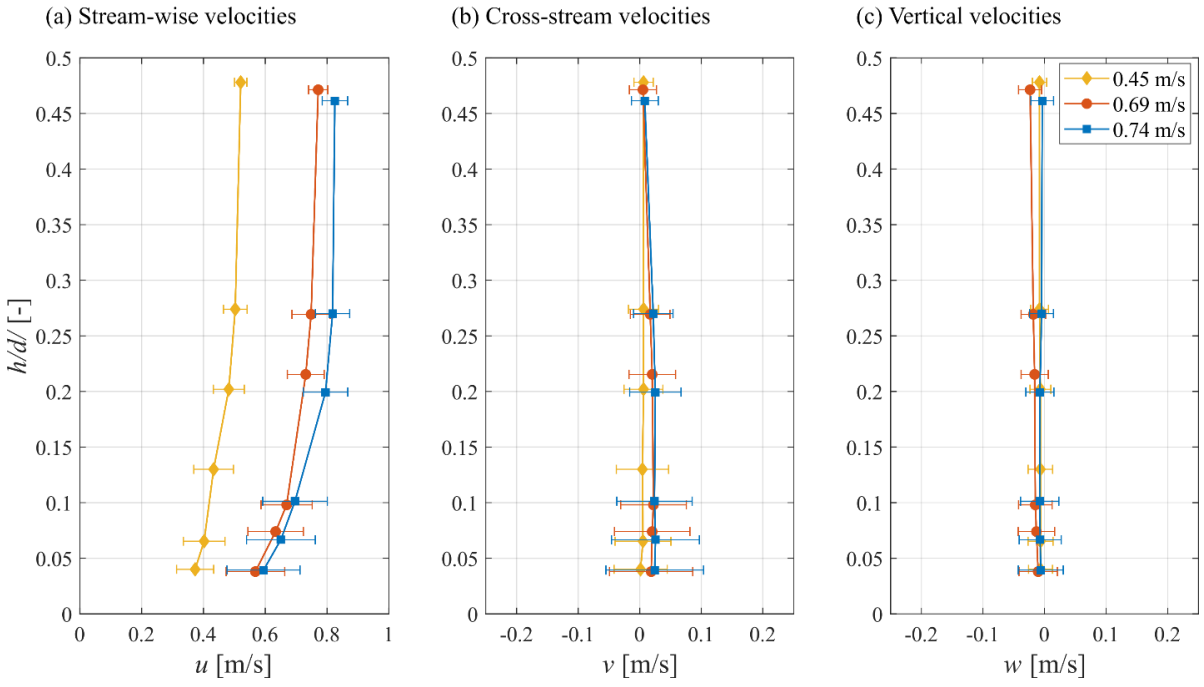

Figure 3.3: Velocity profiles of the three various flow rates used in experimental campaign with error bars representing the root mean square deviation: (a) stream-wise velocities (u); (b) cross-stream velocities (v); (c) vertical velocities (w). The flow depth of the velocity recordings was non-dimensionalized by the total water depth (0.15 m).

Associated Froude numbers ranged from 0.37 to 0.61, with Reynolds numbers ranging from 4×10^4 to 2×10^5. A wide variety of Froude numbers can be observed during flood events. The reported Froude number for extraordinary flood events recorded in the United States ranged from 0.25 to 2.49, with velocities ranging from 1.98 to 9.90 m/s and water depths ranging from 0.58 to 11.00 m (Costa and Jarrett, 2008). The experimental campaign used a 1:30 scale based on the Froude number. This resulted in flow velocities at prototype scale that ranged from 2.5 to 4.1 m/s and a water depth of 4.5 metres, which is comparable to some of the extreme flood events observed in the United States. The lower range of Froude numbers was tested in this study as lower Froude numbers result in more stable debris dam formation (Schmocker and Hager, 2011; Stolle et al., 2018). Therefore, this range was judged to be more relevant for preliminary investigations regarding debris damming loads.

3.2.4 Debris Dam Specimens

A cylinder made of acrylic plastic with a wall thickness of 0.011 m was used to represent a cylindrical column. The cylinder had an outer diameter of 0.09 m. Semi-cylinders and plates constructed of acrylic plastic or aluminum were used to represent debris dams (Figure 3.4). All plate dams and nonporous cylindrical dams were constructed of acrylic plastic. For constructability reasons, the porous cylindrical dams were constructed of aluminum. As the drag force of cylindrical and plate obstacles is pressure-dominated, the material was not considered of significant relevance in modelling the idealized debris dams (Nakayama and Boucher, 1998). In addition, the materials were chosen to facilitate the manufacturing of the fixed debris dams. Fixed debris dams were opted for since Stolle et al. (2017, 2018) have found that modelling the development phase of debris dams requires a very large number of experimental repetitions to produce statistically-meaningful results and it was difficult to determine the voids of these debris dams. The plates represented rigid debris dams that formed a rectangular shape. The semi-cylinders represented ductile debris which, as previously observed, may wrap around a structure and may form a cylindrical or triangularly-shaped dam. All debris dams had a constant width of 0.27 m, which was based on a multiple of three times the width of the column. The width of debris dams is dependent on debris supply so the choice of the debris width used in this study is arbitrary (Stolle et al., 2017).

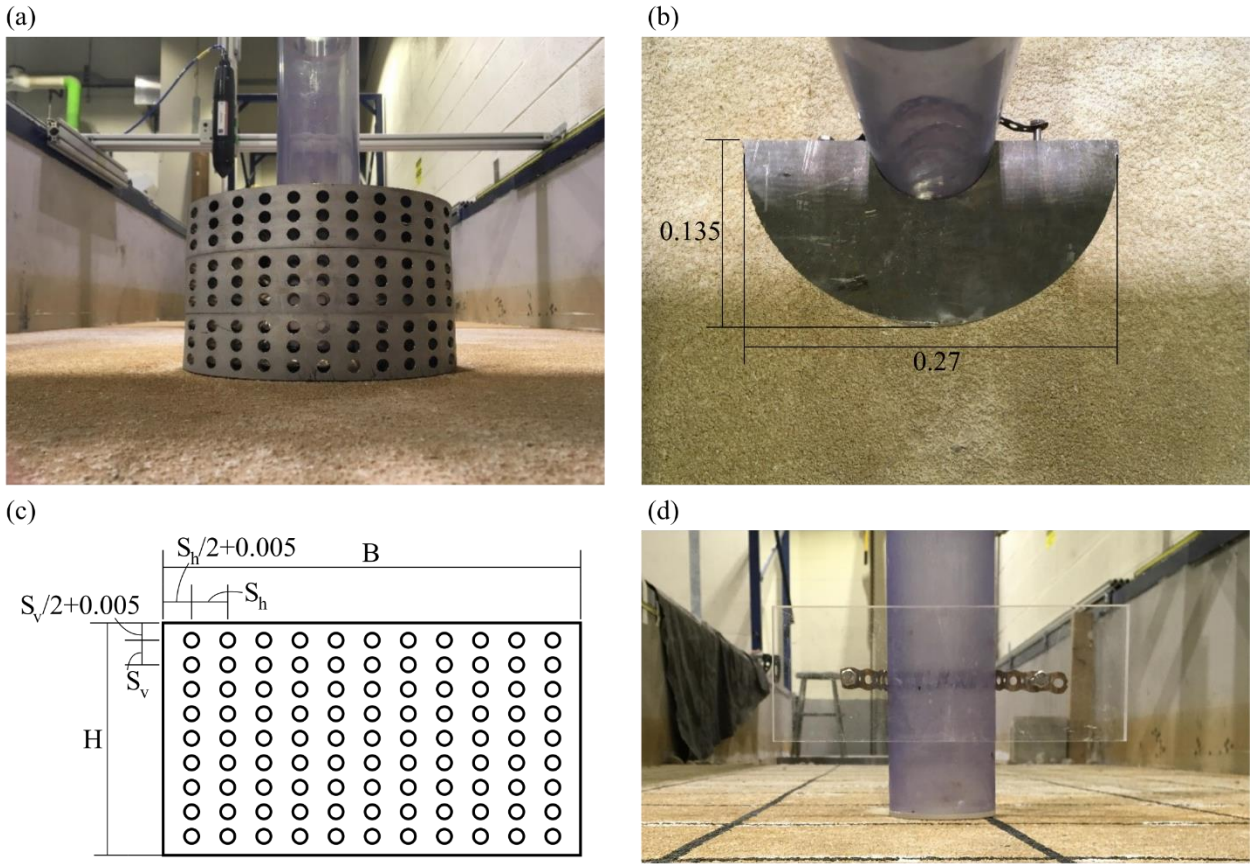

Figure 3.4: Debris dam specimens (all units are in metres): (a) front view of cylindrical dam with 0.2 porosity and 0.15 m height; (b) top view of cylindrical dam; (c) spacing of holes for porous debris dams; (d) front view of plate of 0.10 m height.

Three various heights and porosities were applied to the idealized debris dams resulting in 18 variations of the idealized debris dams, which are described in Table 3.2. The height of the plates and cylinders were fractional multiples of the water depth during tests, which was d= 0.15 m. The multiples of the water depth used for the height of the debris specimens were 1/3d, 2/3d, and 1d. All debris dams were suspended so that the top of the dam would always be at the top of the water surface (0.15 m), as illustrated in Figure 3.4 (d). All plates were 0.013 m (0.5 inches) thick. The thickness of the semi-cylindrical dams was 0.09 m, resulting in an external radius of 0.135 m. The thickness of the plate dams and the radius of the semi-cylindrical dams will be referred to as the length of the dams throughout this paper. The porosities applied to the dams were 0, 20, and 40 percent. The porosity defined here is the ratio of the cross-sectional area of the holes to the cross-sectional area perpendicular to the flow of the debris dams. The diameter of the holes used in the porous dams was 0.01 m. A smaller hole size was chosen to simulate the dam porosity such that disturbance to the flow paths was reduced. Smaller hole sizes are also more likely to form in debris dams as larger voids result in dam instability (Stolle et al., 2018). The same hole size was applied to dams with 20 and 40 percent porosity to maintain a similar flow pattern between the two different porosities. Hole

configuration was optimized to ensure uniform hole distribution and achieving thus the maximum porosity (40 percent). The spacing of the holes is described in Figure 3.4 (c) and Table 3.3.

Table 3.2: Variations of idealized debris dams.

Type of Dam	**Dam Height, *H* (m)**	**Dam Width, *B* (m)**	**Dam Porosity, *n***
Plate	0.15	0.27	0
	0.10	0.27	0
	0.05	0.27	0
	0.15	0.27	0.2
	0.10	0.27	0.2
	0.05	0.27	0.2
	0.15	0.27	0.4
	0.10	0.27	0.4
	0.05	0.27	0.4
Cylindrical	0.15	0.27	0
	0.10	0.27	0
	0.05	0.27	0
	0.15	0.27	0.2
	0.10	0.27	0.2
	0.05	0.27	0.2
	0.15	0.27	0.4
	0.10	0.27	0.4
	0.05	0.27	0.4

3.2.5 Experimental Protocol

For the work presented herein, the experiments were performed in steady-state flow conditions. Three experiments were conducted using no obstacles with three different flow velocities to obtain the free stream

velocity for the case of each flow rate. The free stream velocity was determined to ensure that the presence of the idealized debris dam did not affect the upstream velocity. The experiments were run with only the column present (reference tests) and with the 18 various idealized debris dams (Table 3.2) for each of the three various flow velocities. The load cell and wave gauges recorded the forces acting on the column and water depth, respectively. The experiments were run for durations of 2 minutes to ensure that flow steady conditions had been reached. Following this, experiments were run for 2 additional minutes so that adequate time was given to obtain the mean flow depths and forces acting on the column. The ADV, located upstream of the column, then recorded 12000 data points with a sampling rate of 100 Hz. This sample size ensured that the mean flow velocity was recorded.

Table 3.3: Spacing of holes in porous debris dams.

	Porosity= 0.2		**Porosity= 0.4**	
Dam Height (m)	**Vertical hole spacing, S_v (mm)**	**Horizontal hole spacing, S_h (mm)**	**Vertical hole spacing, S_v (mm)**	**Horizontal hole spacing, S_h (mm)**
0.15	16.0	23.3	16.0	12.2
0.10	15.7	23.3	15.7	12.2
0.05	15.0	23.3	15.0	12.2

3.2.6 Resistance Force Coefficients

The resistance force coefficients were calculated utilizing the data of each test by applying Equation (3) introduced in the Introduction section. Two various resistance coefficients were defined, namely the *bulk resistance coefficient* (C_{RB}) and the *effective resistance coefficient* (C_{RE}). The bulk resistance coefficient was determined bearing in mind difficulties facing engineers tasked with determining the expected porosity of a debris dam in the design process. In premiere, the effective resistance coefficient was proposed to assess the impact of porosity on the resistance coefficient. In addition, this analysis can determine if the area of voids should be deducted from debris dam area when determining the resistance force. The velocities used to calculate both these resistance coefficients were the free stream velocities, which were measured with no obstacles present in the flow. This ensured that the presence of an obstacle did not affect the flow velocity used in the calculation of the resistance coefficients. For both resistance coefficients, the cross-sectional area was calculated using the water depth directly upstream of the column and dam (DS1, Figure 3.2). For dams of partial height or for any overtopping of the debris dams, the corresponding width of the debris dam or column was multiplied to the corresponding water depth to determine the cross-sectional area. The porosity was not deducted from the cross-sectional area when calculating the bulk resistance coefficient. The bulk resistance coefficient and bulk area, respectively, are calculated as:

$$C_{RB} = \frac{2F_R}{\rho_f A_B u^2} \tag{3.4}$$

$$A_B = (h_u - H)D + HW \tag{3.5}$$

where h_u is the water depth measured directly upstream of the column and debris dam, H is the dam height, D is the column diameter, and W is the debris dam width. For the calculation of the effective resistance coefficient, the porosity of the dams was deducted from the cross-sectional area. The effective resistance coefficient and the effective area, respectively, are calculated as:

$$C_{RE} = \frac{2F_R}{\rho_f A_E u^2} \tag{3.6}$$

$$A_E = (h_u - H)D + HW - nHW \tag{3.7}$$

where n is the debris dam porosity.

3.3 Results

3.3.1 Resistance Forces

The horizontal force recorded by the load cell attached to the column, termed as the *resistance force*, is proportional to the flow velocity, the cross-sectional area exposed to the flow, and the resistance coefficient, as described by Equation (3) in the Introduction section. To assess the increased loading due to the debris dams, the resistance forces exerted on the column and debris dams at equilibrium were plotted against the Froude number (Figure 3.5). The resistance forces of the same debris dam were represented as a series of points. The Froude number was calculated using the free stream velocity without the presence of the column or debris dams. This was done to ensure that the presence of the obstacles did not affect the velocity used to calculate the Froude number.

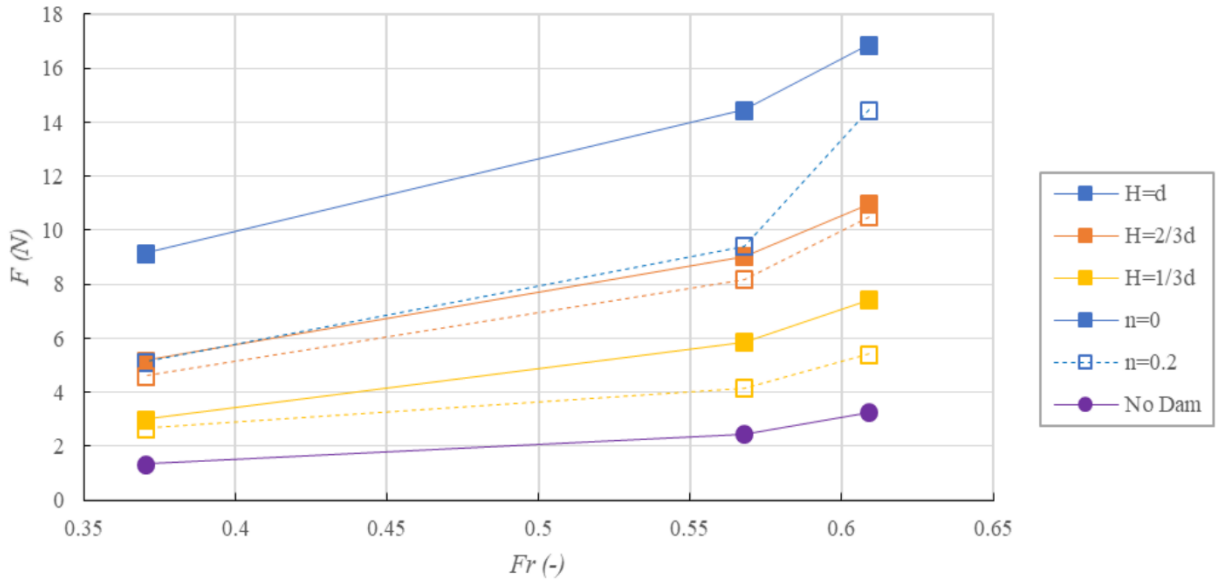

Figure 3.5: Horizontal resistance forces exerted on the column and the debris dam for tests with plate dams of n=0 and n=0.2. The marker shape represents the dam shape, the various colours represent the dam height, and the marker fill and line type represents the dam porosity.

Figure 3.5 indicates a significant increase in loading with the presence of the debris dam compared to when only the column is tested. There is a substantial change in loading for nonporous dams of full height to porous dams or dams of partial height. This is likely due to the nonporous dams of full height causing greater flow redirection in comparison to the partial height dams or the porous dams. The relationship between the variables of the debris dams is illustrated in Figure 3.5. As shown in this figure, the measured loading increases with an increase in the dam height. The porosity also results in a reduction of the magnitude of the hydrodynamic loading; however, the porosity has a lesser impact on the resistance force relative to the decrease observed for a debris dam of decreasing height. Generally, the hydrodynamic loading increases with an increase in the Froude number. The resistance force is proportional to the square of the velocity such that the loading increases at a greater rate as the velocity increase. Most experimental runs exhibited this behaviour; however, as shown in Figure 3.5 there are some outliers, likely due to errors associated with the instruments or flow conditions. Overall, the behaviour of the loading due to flow obstruction follows the outcome of Equation (3) discussed in the Introduction section of this paper.

3.3.2 Resistance Coefficients

The resistance coefficients were calculated as outlined in the Methodology. The bulk resistance coefficient is the resistance coefficient with only the height of the dam deducted from the cross-sectional area. The effective resistance coefficient is the resistance coefficient with the dam porosity and dam height deducted from the cross-sectional area. The resistance coefficients ranged from 0.72 to 1.02 for the column with no debris dam present, tested in Froude numbers ranging from 0.37 to 0.61. This is comparable to a similar set

of experiments conducted by Hay (1947). In this study, the resistance coefficients are compared to the variables tested throughout the experimental campaign including Froude number, debris dam shape, debris dam height, and debris dam porosity.

Welch's *t*-tests were completed to quantitatively analyze the impacts of each individual variable on the resistance coefficients. The variables considered were the dam shape, the Froude number, the relative dam height, and the dam porosity. As described by McDonald (2009), *t*-tests provide the probability (*P*) of the null hypothesis occurring. In this study, the null hypothesis is the mean difference between the resistance coefficients of the paired variables being equal to zero. A lower probability means that there is a correlation between the variable and the resistance coefficients. The *t*-test also determines the statistical and critical *t*-value. The statistical *t*-value (t_{Stat}) is equal to the mean of the differences between resistance coefficients for the corresponding variables divided by the sample variance. The critical *t*-value ($t_{critical}$) is based on the assigned confidence interval, which was selected to be 90% in this analysis. When the absolute statistical *t*-value is greater than the critical *t*-value, there is 90% confidence that the difference in the resistance coefficient for the paired variables is not due to chance. A positive statistical *t*-value also indicates that the resistance coefficient generally increases from the corresponding first variable to the second variable. An assumption of this test is that the variances of the resistance coefficient between the compared variables are unequal. A summary of the results of the *t*-tests is listed in Table 3.4 and Table 3.5, for the bulk and effective resistance coefficient, respectively.

Table 3.4: Results of the t-tests for the bulk resistance coefficient.

Variables	**Variables Compared**	***P* (-)**	$t_{critical}$	t_{Stat}	**90% Confidence ($\lvert t_{Stat}\rvert > t_{critical}$)**
Dam Shape	Plate and Cylindrical Dam	0.3592	1.6829	0.9273	No
Froude Number	*Fr*=0.61, *Fr*=0.57	0.6560	1.7033	0.4505	No
	Fr=0.61, *Fr*=0.37	0.0115	1.7207	-2.7693	Yes
	Fr=0.57, *Fr*=0.37	0.0106	1.7139	-2.7811	Yes
Dam Height	*H*=*d*, *H*=2/3*d*	0.1962	1.7341	1.3424	No
	H=*d*, *H*=1/3*d*	0.0562	1.7392	2.0492	Yes
	H=2/3*d*, *H*=1/3*d*	0.0802	1.6955	1.8087	Yes
Dam Porosity	*n*=0, *n*=0.2	0.0160	1.7081	2.5836	Yes
	n=0, *n*=0.4	0.0010	1.7291	3.8691	Yes
	n=0.2, *n*=0.4	0.1287	1.7139	1.5760	No

Table 3.5: Results of the t-tests for the effective resistance coefficient.

Variables	Variables Compared	P (-)	$t_{critical}$	t_{Stat}	90% Confidence ($\|t_{Stat}\| > t_{critical}$)
Dam Shape	Plate and Cylindrical Dam	0.3166	1.6849	1.0145	No
Froude Number	*Fr*=0.61, *Fr*=0.57	0.5836	1.7011	0.5546	No
	Fr=0.61, *Fr*=0.37	0.0016	1.7171	-3.6055	Yes
	Fr=0.57, *Fr*=0.37	0.0005	1.7081	-3.9948	Yes
Dam Height	*H*=*d*, H=2/3*d*	0.0625	1.7341	1.9855	Yes
	H=*d*, *H*=1/3*d*	0.0037	1.7247	3.2815	Yes
	H=2/3*d*, *H*=1/3*d*	0.0447	1.7109	2.1186	Yes
Dam Porosity	*n*=0, *n*=0.2	0.4246	1.6991	0.8099	No
	n=0, *n*=0.4	0.9490	1.7207	0.0648	No
	n=0.2, *n*=0.4	0.4193	1.7109	-0.8218	No

3.3.2.1 Froude Number

The resistance coefficients were plotted against the Froude number (Figure 3.6 and Figure 3.7) as the resistance coefficient is known to vary with Froude number (Chaplin and Teigen, 2003). Both plots of the resistance coefficients illustrated that the resistance coefficient generally decreases with Froude number for corresponding dam parameters. The results of the *t*-tests for both coefficients also indicate that the resistance coefficient decreases from the Froude number of 0.37 to Froude numbers of 0.57 and 0.61. However, there are negligible significance in the resistance coefficients between the Froude number of 0.61 and the Froude number of 0.57, which is likely due to the similarity of these Froude numbers.

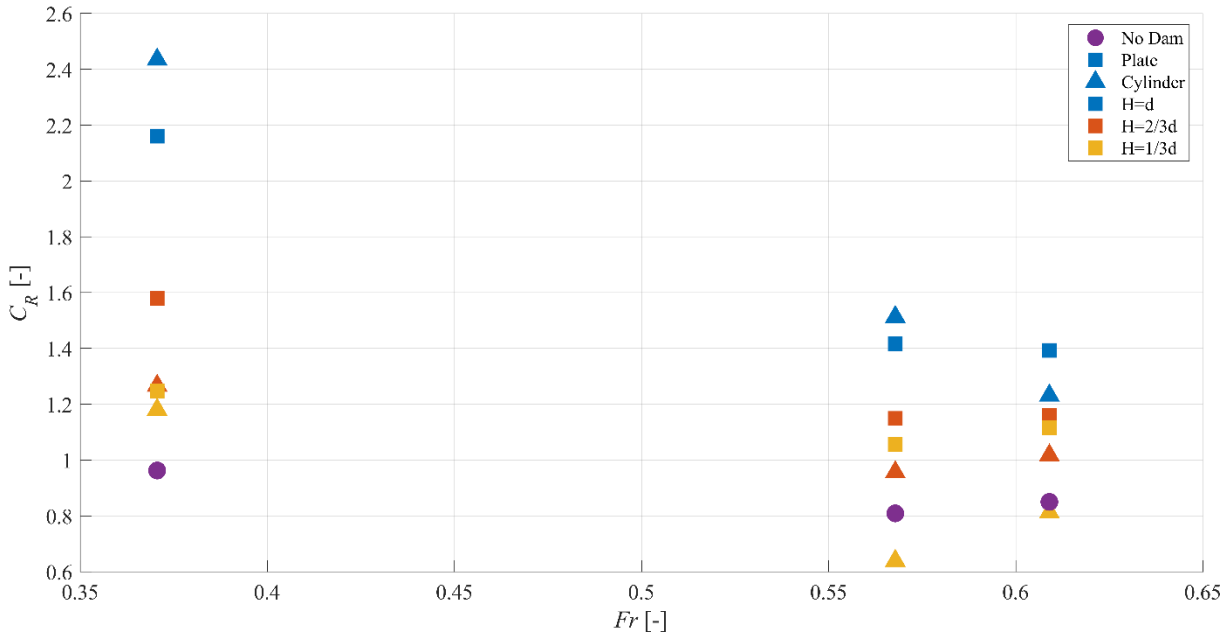

Figure 3.6: The resistance coefficient versus the Froude number illustrating the effects of dam height. Only the nonporous dams are included in this plot. The various marker shapes indicate the dam shape and the various marker colours indicate dam height.

3.3.2.2 Debris Dam Shape

There is generally an increase of the resistance coefficients in the presence of debris dams compared to when only the column is present in the flow. This is expected as a cylinder has a lesser drag coefficient relative to a plate or semi-cylinder. Some of the tests in the presence of the porous debris dams resulted in a bulk resistance coefficient that was less than the bulk resistance coefficient obtained for the case when only the column is present at corresponding Froude numbers. The resistance coefficient is inversely related to the cross-sectional area of the flow obstruction so this result can be expected because the porosity is not deducted from the cross-sectional area. A significant increase in the effective resistance coefficients can be observed in Figure 3.7 (b) for the plate and cylindrical dam relative to when only the column is present.

There is no significant change in the resistance coefficients between the plate and cylindrical dams, as indicated by both *t*-tests. While one would expect that the plate dams would result in a greater resistance coefficient relative to the cylindrical dams, the results obtained in this study showed that this was not the case: this may be attributed to the variance in the length to width ratio of the plate and cylindrical dams. The length to width ratio of the plate and cylindrical dams is 0.05 and 0.5, respectively. Laneville and Yong (1984) observed an increase in the drag coefficient for increasing length to width ratios within the range of 0 to 0.8 for rectangular columns. In addition, the cylindrical debris dams have a greater surface area relative to the plate dams, which could result in greater resistance forces of the cylindrical dams due to skin friction. This may be the reason for the lack of difference of the resistance coefficients between the plate and cylindrical dams.

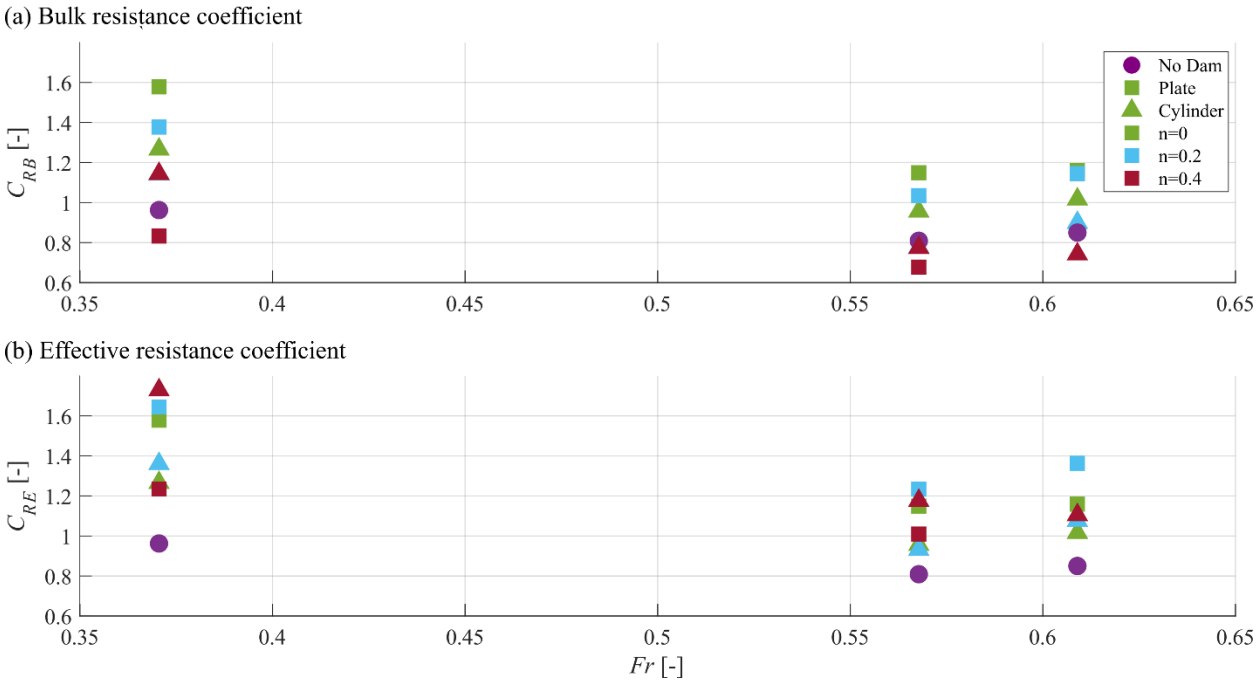

Figure 3.7: The resistance coefficient versus the Froude number illustrating the effects of dam porosity: (a) the bulk resistance coefficient; (b) and the effective resistance coefficient. Only the dams of H=2/3d are included in this plot. The various marker shapes indicate the dam shape and the various colours indicate dam porosity.

3.3.2.3 Debris Dam Height

Generally, the resistance coefficient increases with an increase in height, as illustrated in Figure 3.6. This results can be expected because as the dam height decreases, the aspect ratio (height to width) and flow blockage also decreases, resulting in a decrease in the drag coefficient (Alridge et al., 1978). In addition, as the height decreases, the exposure of the column increases. A cylinder has a lesser drag coefficient in comparison to a plate or semi-cylinder, which would result in a reduction in the resistance coefficient.

The *t*-tests comparing the effective resistance coefficients between the relative dam heights showed a strong relationship between the effective resistance coefficient and the dam height. All statistical *t*-values were greater than the corresponding critical *t*-values (Table 3.5). The *t*-tests conducted for the bulk resistance coefficient indicate that the height of the dam affects the coefficient between the relative dam heights of 1 to 1/3 and 2/3 to 1/3; however, there is no significant variation between the relative dam heights of 1 to 2/3 (Table 3.4). Due to the negligible differences in bulk resistance coefficients between the relative dam heights of 1 to 2/3, an additional *t*-test separated by porosity was conducted between these two variables, as shown in Table 3.6. This *t*-test indicated that while there is a variation in the bulk resistance coefficient for nonporous dams with the relative dam heights of 1 to 2/3, there are still negligible changes between the porous dams. This could be attributed to the variance in backwater rise between porous and nonporous dams. There are more significant changes in backwater rise for nonporous dams compared to porous dams

for the relative dam heights of 1 to 2/3. This is because there is a greater variance in the blockage of flow for the nonporous dams. This results in a greater change in the cross-sectional area and as the bulk resistance coefficient is inversely related to the cross-sectional area, it results in greater impacts on the resistance coefficients of nonporous dams. The impacts of dam geometry on backwater rise will be further discussed in a following subsection, titled Flow Conditions.

Table 3.6: Results of the t-tests for the bulk resistance coefficient between H=d and H=2/3d, for the porosities used.

Variables Compared	Porosity	P (-)	$t_{critical}$	t_{Stat}	90% Confidence ($\|t_{Stat}\| > t_{critical}$)
H=d, H=2/3d	n=0	0.0572	1.8946	2.2737	Yes
	n=0.2	0.8247	2.0150	-0.2334	No
	n=0.4	0.9678	2.3534	0.0438	No

3.3.2.4 Debris Dam Porosity

Increasing porosity of the debris dams results in a decrease in the bulk resistance coefficient (Figure 3.7 (a)). The *t*-tests indicate that there is a decrease in the bulk resistance coefficient from nonporous dams to the dams of 20 and 40 percent porosity. There are no significant changes in the bulk resistance coefficient between dams of 20 and 40 percent porosity. This illustrates that the presence of the holes affects the bulk resistance coefficient; however, there are no significant differences between the porous dams. The porosity significantly decreases the aspect ratio with respect to the flow, however, there is not a significant reduction in the aspect ratio from dams of 20 percent porosity to dams of 40 percent porosity. The drag coefficient is known to decrease with a decrease in the aspect ratio of obstacles (Alridge et al., 1978).

The *t*-test for the effective resistance coefficient demonstrates that the porosity does not follow the null hypothesis for all paired porosities (Table 3.5). This indicates that there is high variability regarding the impact of porosity on the effective resistance coefficient. The porosity lowers the aspect ratio of the flow, which would result in an overall decrease in resistance (Alridge et al., 1978). However, the porous holes would create an increase in skin friction resulting in greater resistance forces. These two opposite influences may counteract one another, resulting in the porosity having inconsistent impacts on the resistance coefficient. In many cases, the effective resistance coefficient is greater for porous dams in comparison to nonporous dams, as illustrated in Figure 3.7 (b).

3.3.2.5 Overall Influence of Tested Variables

Multiple linear regressions were performed to assess the influence of the experimental variables on the resistance coefficients. These values were obtained using the Regression tool available in Microsoft Excel. The first regression was performed for the bulk resistance coefficient and the effective resistance coefficient

as a function of the Froude number, relative dam height, and porosity. The second regression was performed for the resistance coefficients as a function of standardized variables. The results of both regressions are listed in Table 3.7. The Froude number, the relative dam height, and porosity were standardized using *z*-scores, which was conducted using the *z*-score function in MATLAB. The *z*-score determines the mean and standard deviation of a data set. The function then determines the number of standard deviations that a value is away from the mean. Determining the *z*-scores of the independent variables allows for the comparison of various regression coefficients. Only one regression was conducted for the plate and cylindrical dam as the *t*-tests indicated that there was no significant difference between the resistance coefficients of the varying dam shapes.

Table 3.7: Coefficients of the multiple linear regressions for the bulk and effective resistance coefficients.

	Intercept	***Fr* (-)**	***H/d* (-)**	***n* (-)**	R^2
C_{RB}	1.797	-1.634	0.471	-1.125	0.608
C_{RB} **(*z*-score)**	1.043	-0.170	0.128	-0.186	0.608
C_{RE}	1.799	-1.850	0.634	-0.178	0.578
C_{RE} **(*z*-score)**	1.214	-0.193	0.172	-0.029	0.578

The regressions illustrate that the resistance coefficient decreases with the Froude number. The Froude number has a similar impact on the bulk and effective resistance coefficient. The regression also indicates that the effective resistance coefficient increased with the relative dam height. Similarly, the bulk resistance coefficient increased with the relative dam height. However, the effects of this variable are not as significant in comparison to the effective resistance coefficient. This was also indicated by the *t*-tests as the relative dam height from 1 to 2/3 did not follow the null hypothesis for the bulk resistance coefficient (Table 3.4). The dam porosity was shown to have a significant impact on the bulk resistance coefficient but had little impact on the effective resistance coefficient, which was also illustrated by the *t*-tests conducted for the resistance coefficients (Table 3.4, Table 3.5). The porosity was deducted from the cross-sectional area used to determine effective resistance coefficient. This reduction in the cross-sectional area did not account for the increase in skin friction due to porosity, resulting in increased effective resistance coefficients of porous dams. Porosity also resulted in a decrease in the aspect ratio with respect to the flow and therefore, it reduced the bulk resistance coefficient.

3.3.3 Flow Conditions

The change in water depth upstream and downstream of obstacles in choked flows results in increased hydrodynamic loading (Qi et al., 2014). Debris dams can cause greater backwater rise as a result of a

decrease in the flow area, thus obstructing the flow. The flow pattern around the debris dams tested in this study is shown in Figure 3.8. As shown in this figure, the flow depth increases upstream of the flow obstacle and a wake forms downstream of the flow obstacle, resulting in a decrease in water depth. The change in the water depth directly upstream and downstream of the column and debris was determined and normalized by the initial water depth (0.15 m). This value is labelled as $\Delta h/d$:

$$\frac{\Delta h}{d} = \frac{h_u - h_d}{d} \tag{8}$$

where h_u is the water depth measured by DS1 and h_d is the water depth measured by DS2.

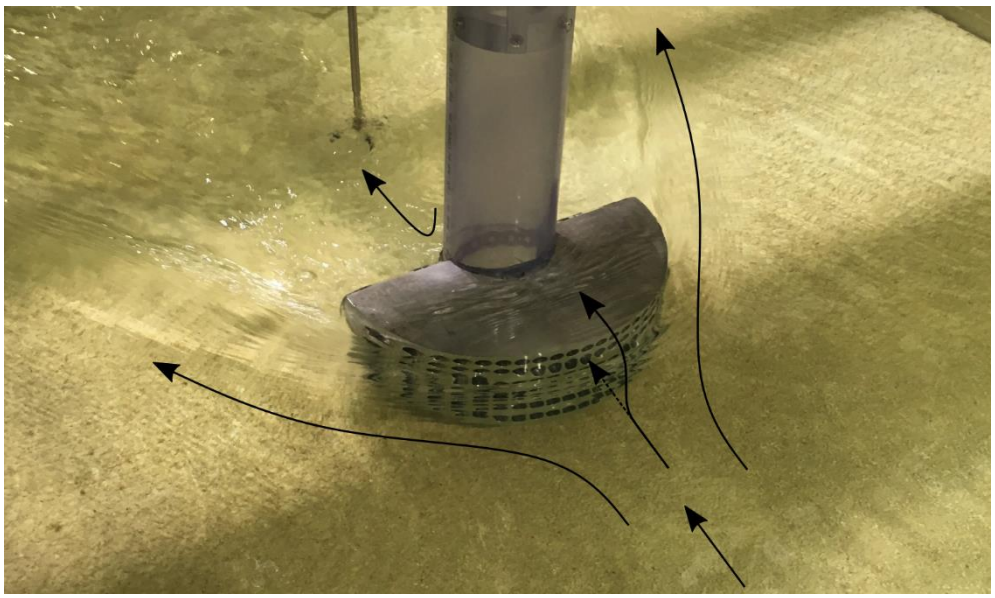

Figure 3.8: Observed flow pattern surrounding the debris dam and column - view from upstream. Arrows indicate the overall flow directions around and through the debris dam.

The normalized change in water depth was compared to the Froude number in Figure 3.9. As there was significant overlap of the data points, the results were slightly varied in terms of Froude number using the *jitter* function in MATLAB. *T*-tests were conducted to assess the impacts of debris dam variables on the normalized change in water depth, as summarized in Table 3.8. There is significant variances between the nonporous dams and the porous dams. As illustrated by the *t*-tests, the porosity of 0 to 0.2 and 0.4 impacts the change in water depth; however, there is no significant variances between porosities of 0.2 and 0.4. This is likely due to the significant changes in flow blockage between the nonporous dams to porous dams, but insignificant changes in flow blockage for the dam porosity varying from 0.2 to 0.4. There is generally a decrease in the change in water depth as the dam height decreases. This is likely due to greater backwater rise occcuring when there is greater blockage occurred at the location of the dam (Stolle et al., 2017). Hay (1947) analyzed the decrease in water depth downstream of a column with various submergence. His study

found that the depression behind the column significantly increased as the column increased submergence. This created a greater disturbance in the flow path resulting in greater changes in water levels.

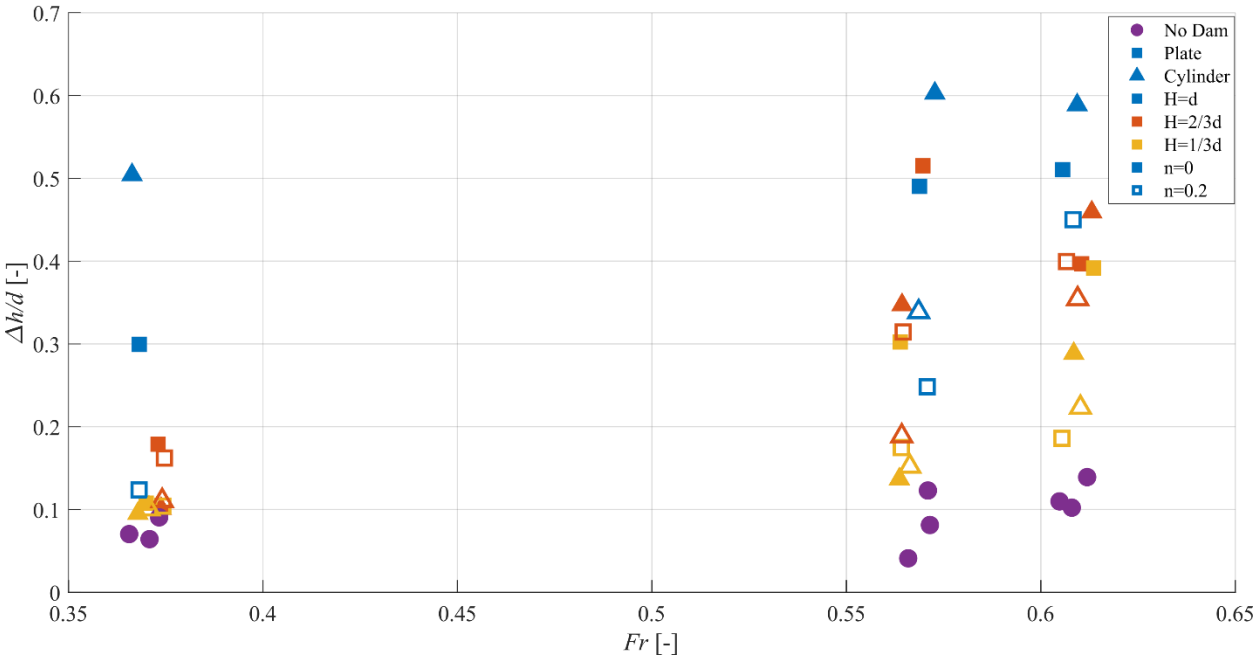

Figure 3.9: Changes in upstream and downstream water depth normalized by total water depth versus the Froude number. The marker shapes represent the dam shape, the colours represent the dam height, and the marker fill represents the debris porosity. Only the dams of n=0 and n=0.2 are included in this plot. Due to significant overlap of the data points, the results were slightly varied in terms of Froude number for better presentation of the results.

Overall, the *t*-tests indicated that there is no correlation between the change in water depth and the dam shape. However, when comparing the change in water depth due to the presence of the plate and cylindrical dam, there were greater changes in water depth for the case of nonporous cylindrical dams with full dam height compared to the corresponding plate dams at all Froude numbers. This could be due to the greater length of the cylindrical dams compared to that of the plate dams (Laneville and Yong, 1984). The ratio of dam length to dam width impacts the streamlines surrounding the flow obstruction. Laneville and Yong (1984) found that wake vortices form closer to the base area for rectangular prisms with increasing length to width ratios from 0 to 0.8. The length to width ratio for the plate and cylindrical dam is 0.05 and 0.5, respectively. As wake vortices form closer to the dam, there is a greater decrease in water depth. This could result in greater changes of the water depth for the cylindrical dam relative to the corresponding plate dams.

Table 3.8: Results of the t-tests for the normalized change in water depth directly upstream and downstream of the column and debris dam.

Variables	**Variables Compared**	***P* (-)**	$t_{critical}$	t_{Stat}	**90% Confidence ($\lvert t_{Stat}\rvert > t_{critical}$)**
Dam Shape	Plate and Cylindrical Dam	0.3166	1.6839	0.3781	No

Froude Number	*Fr*=0.61, *Fr*=0.57	0.1531	2.0518	1.4702	No
	Fr=0.61, *Fr*=0.37	0.0001	1.7011	4.5793	Yes
	Fr=0.57, *Fr*=0.37	0.0102	1.7011	2.7553	Yes
Dam Height	*H*=*d*, *H*=2/3*d*	0.0625	1.7109	1.9546	Yes
	H=*d*, *H*=1/3*d*	0.0037	1.7171	4.2078	Yes
	H=2/3*d*, *H*=1/3*d*	0.0447	1.7011	2.1398	Yes
Dam Porosity	*n*=0, *n*=0.2	0.0572	1.7056	1.9902	Yes
	n=0, *n*=0.4	0.0531	1.7171	2.0441	Yes
	n=0.2, *n*=0.4	0.9552	1.7081	-0.0568	No

A multiple linear regression was conducted for the change in upstream and downstream water depth normalized by the free stream water depth (0.15 m) as a function of the Froude number, relative dam height, and porosity, which is listed in Table 3.9. Another multiple linear regression was conducted using the standardized values of the Froude number, relative dam height, and porosity (Table 3.9). The values were standardized by applying a *z*-score to each value as previously discussed. The multiple linear regressions were performed using the Regression tool in Microsoft Excel.

The regressions illustrate the relationship of the various testing parameters and the change in water depth. An increase in the Froude number, an increase in the relative dam height, and a decrease in the dam porosity resulted in an increase in the change in water depth. The standardized linear regression illustrated that the Froude number and relative dam height have a similar influence on the normalized change in water depth. The porosity had a lesser impact on the change in water depth likely due to the negligible changes between the porosities of 0.2 and 0.4, as indicated by the *t*-test (Table 3.8). However, porosity still influenced the change in upstream and downstream water depth, as shown in Figure 3.9.

Table 3.9: Coefficients of the multiple linear regressions conducted for the change in water depths upstream and downstream of the column.

	Intercept	***Fr* (-)**	***H/d* (-)**	***n* (-)**	R^2
⊿h/d	-0.231	0.737	0.228	-0.307	0.710
***⊿h/d* (*z*-scoring)**	0.270	0.077	0.075	-0.051	0.710

3.4 Discussion

The experiments were scaled using Froude similitude so there is potential for scaling issues as the drag coefficient is a function of the Reynolds number (Sumer and Fredsøe, 1997). The Reynolds number in this study ranged from 4.0×10^4 to 2.0×10^5. The characteristic length used to determine the Reynolds number was the width of the dam (0.27 m) or the width of the column (0.09 m) if no dam was present. This range significantly exceeds the critical value for the transition to turbulence of 1.25×10^4 (Chow, 1959). However, the range of Reynolds numbers in this study does not exceed the critical Reynolds number of 3×10^5 for the transition from laminar to turbulent flow of the boundary layer surrounding a column stated by Kundu (1990).

Typically, debris entrained in flood events and in rivers are buoyant (Diehl, 1997; Matsutomi et al., 2006; Nistor et al., 2017). A limitation of this study is that the idealized debris dams were not constructed of buoyant materials and were tightly secured to the column – the authors chose to represent the formation of a stable debris dam under various flow conditions. Although all debris dams were secured such that the top of the dam was set at 0.15 m (the total flow depth), the occurring backwater rise resulted in the overtopping of the debris dams. This may have influenced the magnitude of the resistance forces that were recorded in the experiments. The buoyancy of debris dams may also influence the observed changes in water levels (Stolle et al., 2017).

The debris dams were constructed using two different materials, namely acrylic plastic and aluminum. All of the plate dams and the nonporous cylindrical dams were constructed of acrylic plastic while the porous cylindrical dams were constructed of aluminum. These two materials have slightly different surface roughness and, though assumed minimal, may have also affected the flow resistance of the dams. However, the impacts of this are likely insignificant as the drag force of cylinders and plates is dominated by pressure drag rather than skin friction (Nakayama and Boucher, 1998).

The variances in the length of the cylinder and the plate dam may cause discrepancies when comparing the resistance coefficients between the dam shapes. The resistance coefficient was calculated in two-dimensions, which is common in the field of fluid mechanics (Chaplin and Teigen, 2003; Stolle et al., 2018). In reality, the length of the object obstructing flow affects the resistance forces. By considering the resistance coefficient in only two-dimensions, the effects of skin friction in the stream-wise direction were ignored. As the cylindrical dams have a greater surface area relative to the plate dams, larger resistance forces due to skin friction acting on the cylindrical dams may occur. Therefore, increased loading due to skin friction could have led to the lack of variation between the loads exerted onto the two dam shapes. The drag coefficient of an obstacle also varies with the length to width ratio of the flow obstruction due to the

formation of streamlines and the separation of flow from the obstruction (Laneville and Yong, 1984; Yu et al., 2013). Laneville and Yong (1984) concluded that the drag coefficient of a rectangular obstruction increases when the length to width ratio of the flow obstruction ranges from 0 to 0.8 in Reynolds numbers greater than 6×10^4. The length to width ratio of the plate and cylindrical dam was 0.05 and 0.5, respectively. Therefore, a relative increase in the resistance coefficient of the cylindrical dam compared to the plate dam due to the increased length to width ratio could have occurred. However, it is important to note that the study conducted by Laneville and Yong (1984) only tested rectangular shapes so there is still uncertainty when comparing these values to the plate and cylindrical dams used in the present study.

A limitation in this study resides in that the holes of the idealized debris dams were oriented parallel with the flow direction. In a flood event, the voids of debris dams have 3-dimenisional flow paths due to the random formation of debris accumulations. The varying flow paths within the voids of such natural dams can result in a transition from turbulent to close to laminar flows, which could modify the overall flow behaviour. More complex flow paths would also likely increase flow resistance, resulting in an augmentation of the resistance coefficient. This is especially important to consider when assessing the results of the bulk resistance coefficient, as the authors concluded that the porosity had negligible impacts on the effective resistance coefficient. As indicated in the *t*-tests for the bulk resistance coefficient (Table 3.4, Table 3.6), the porosity resulted in a decrease in the bulk resistance coefficient. In reality, the porosity of a debris dam may have a lesser impact on the bulk resistance coefficient due to the 3-dimensional voids in the dam. Similarly, this can be applied to the change in water depth upstream and downstream of debris dams. The changing flow paths in the voids of debris dams could result in greater changes in water depth upstream and downstream of the debris dam and structure due to greater resistance.

The effects of the blockage ratio (the area of the flow obstruction to the area of the channel) on the resistance coefficients and the backwater evolution were not investigated in this study. The blockage ratio is known to affect the drag coefficient of flow obstructions (Parola et al., 2000). The objective of this study was to investigate the impacts of various debris dam parameters on flow conditions and, therefore, there should be no impacts on flow conditions due to flow blockage or wall effects. The maximum ratio of flow obstruction to channel width used in the experiments was 0.18. Achenbach (1974) investigated the impacts of wall effects on the drag coefficient of a sphere. The study concluded that there was no significant impact of blockage ratio on the drag coefficient until the blockage ratio exceeded 0.4 with Reynolds number of 2×10^5. Therefore, the results obtained in this experimental campaign should not be impacted by wall effects due to the low blockage ratios of the experiments.

3.5 Conclusions

This study investigated flow structure and associated hydrodynamic loading around idealized debris dams in steady-state flow conditions. Various debris dam heights, porosities, and shapes were tested against a variety of flow velocities to assess the induced hydrodynamic loading on debris dams attached to a column. Bulk and effective resistance coefficients were determined to assess the impact of debris dam geometry on total force coefficients. Conclusions stemming from this study and its results are:

- The resistance forces acting on the debris dams and column increased with increasing Froude number and dam height, and decreased with increasing dam porosity.
- It was found that, as anticipated, the resistance coefficient is dependent on the Froude number.
- The height of the debris dams generally influenced the resistance coefficients as an increase in the dam height resulted in a less hydrodynamically-efficient shape – due to a greater aspect ratio and greater blockage. The porosity of the debris dams resulted in a reduction of the bulk resistance coefficient. No significant correlation was observed between the dam porosity and the effective resistance coefficient due to increased skin friction created by the holes.
- Changes in water depth upstream and downstream of the column were related to the dam height and their porosity; with an increase in water depth correlated with increased flow blockage.

This study represents a preliminary investigation towards assessing the impacts of debris damming on flow conditions and the associated hydrodynamic loading on structures. These results illustrate that when designing structures against debris damming loads, the potential flow conditions should be predicted when applying a resistance/ drag coefficient. The potential height of the debris dam should be considered in the design process while the porosity may have a lesser impact on loading. As a conservative assumption in the design process, the dam should be considered to be nonporous and its height to be equal with the full depth of the water column where more specific information on the dam characteristics is lacking. The variables used in this study were three flow velocities, two dam shapes, three dam heights, and three dam porosities. Further investigations are needed to assess the effect of other debris dam parameters, such as debris dam roughness, width, length, and shape. Tests utilizing a wider range of Froude numbers should also be conducted to obtain a more comprehensive understanding of debris damming loads under various flow conditions. The results of this study provide incipient insight regarding flow behaviour surrounding debris

dams and their impacts on structures. As this study was performed in steady-state conditions, the results can be applied to fluvial/ riverine systems with debris damming issues.

Chapter 4. Experimental investigation of loading due to debris dams in transient flow conditions

4.1 Introduction

Tsunamis and extreme flooding events often have devastating and damaging impacts on coastal communities as extreme turbulent floods induced by such events inundate coasts. This occurred during many recent events, including the 2004 Indian Ocean Tsunami, the 2005 Hurricane Katrina, and the 2011 Tohoku Tsunami, all which resulted in large-scale damage and loss of life (Matsutomi et al., 2006; TCLEE, 2006; Suppasri et al., 2012). During the 2011 Tohoku Tsunami, there were several unexpected structural failures, particularly in the case of reinforced concrete structures, which were previously thought to be indestructible in tsunami events (Yeh et al., 2013). These failures highlighted the need for a more comprehensive understanding of extreme loads in order to better design flood-resistant structures (Yeh et al., 2015; Chock, 2016). A specific type of loading that is often difficult to assess, especially in terms of post-flood field surveys, is that due to debris (Yeh et al., 2013; Naito et al., 2014; Nistor et al., 2017).

Debris entrained in storm surges or tsunamis often accumulate onto the face of a structure or structural element or in between such elements. When single pieces of debris accumulate and subsequently form a larger body in close vicinity to structures, a *debris dam* forms. Debris dams can result in a significant increase in loading on structures as debris dams increase the surface area of a structure exposed to the flow (Yeh et al., 2015; Stolle et al., 2017; Stolle et al., 2018). Increased flow obstruction due to debris damming can also result in greater water depths upstream of the structure, which can result in overtopping of the impacted structures (Bricker et al., 2012; Stolle et al., 2017, Schalko et al., 2019a). Debris dams can generate an increase in the magnitude of the vertical flow velocities and accelerations, resulting in increased scour (Pagliara and Carnacina, 2011, Schalko et al., 2019b).

While research conducted on debris damming in extreme coastal floods is scarce, there has been a wide array of research conducted in the field of river engineering. Most often, this research uses constant flow conditions to evaluate the effects that debris dams generate. Debris dam formation occurs when debris accumulate on or around structures. The formation of debris dams can be considered a random process. However, there are several observed variables that influence debris dam formation including debris geometry, debris size, flow conditions, and channel blockage. Schmocker and Hager (2011) analyzed the probability of debris dam formation. Their study concluded that the probability of dam formation increased with a decrease in the Froude number. Schmocker and Hager (2011) stated that this was due to the debris becoming more easily re-entrained with increased flow velocities. Stolle et al. (2017) observed that debris

of greater individual size resulted in a greater probability of entrapment. Tests with greater flow velocity resulted in dams of lesser thickness (in the stream-wise direction) and greater height due to progressive compaction of the dam. The width of the debris dam was dependent on the amount of debris supplied. Similarly, when Pasha and Tanaka (2016) studied the capture efficiency of debris on inland forests in tsunami events, they found that the capture efficiency increased with an increase in debris length and with a decrease in flow velocity.

Differences were observed in debris dam formations between the case of debris tested in steady-state and those tested under transient flow conditions. Stolle et al. (2017, 2018a) conducted two experimental studies in which debris accumulating onto a structure were tested: first in steady-state flow conditions, with Froude numbers ranging from 0.3 to 0.6, and then in transient flow conditions, with Froude numbers ranging from 1.3 to 2.0. Overall, the process of debris dam formation was similar in both sets of flow conditions; however, there were some discrepancies in the dam formation relative to the steady-state experiments. The transient flow conditions led to a more compact and narrow dam relative to the dams formed in steady-state flow conditions. This was attributed to the higher velocities and turbulent flow observed in the case of the transient flow conditions.

St-Germain et al. (2014) investigated the fluid-structure interaction of a tsunami-induced bore numerically using the Smoothed Particle Hydrodynamics method in which a square column was subjected to dam-break waves. Derschum et al. (2017) conducted an experimental program regarding debris impact on a column tested in dam-break waves and compared their results with the numerical results of St. Germain et al. (2014). When the bore impacted the column, there was a significant amount of splash-up that occurred during the initial impact of the bore. Subsequently, the flow formed an area of reduced velocity directly in front of the column due to the blockage generated by the column. The flow moving around the structure also experienced a reduction in velocity compared to when there was no structure present. Significant runup resulted in the formation of a surface roller onto on the front face of the structure. This surface roller resulted in rotational motion upstream of the column, reducing the horizontal velocity of the surface roller. Eventually, the surface roller began to propagate upstream, resulting in negative horizontal velocities. The presence of vertical accelerations as a result of the roller, as well as redirection of the flow around the column, resulted in the destabilization of the debris caught upstream of the column, reducing thus the potential for the debris dam formation (Derschum et al., 2017).

There is still significant uncertainty relating to debris dam geometry due to the random nature of debris dam formation. Zevenbergen et al. (2007) investigated a photographic archive of woody debris accumulated around bridge piers throughout the United States of America. This study concluded that two main debris dam cross sections typically form: a triangular shape and rectangular shape. Despite previous researchers

considering debris dams to be floating rafts, this study determined that debris dams can also form at the bottom of a river channel due to downward-oriented vertical fluid accelerations and thus the occurrence of a momentum transfer which submerges debris and pushes them towards the channel bottom. Similarly, a study regarding debris damming conducted by Parola et al. (2000) also concluded that debris dams can form at the bottom of the flow channel.

Debris damming loads in river engineering applications are typically characterized as a quasi-steady force as they are associated with stable debris dams that have already accumulated and/or consolidated. The loading due to debris damming can be estimated using the typical drag force equation:

$$F_D = \frac{1}{2} C_D \rho_f B h u^2 \tag{4.1}$$

where C_D is the drag coefficient, ρ_f is the density of the fluid, B is the cross-stream width of the debris dam, h is the water depth, and u is the flow velocity. Parola et al. (2000) conducted a study in steady-state conditions on loading due to debris accumulated on bridge piers. This study illustrated that the drag coefficient of debris dams is a function of the blockage ratio and of the Froude number.

The drag coefficient is typically used to describe the hydrodynamic efficiency of a fully submerged object. Structures such as the columns of buildings inundated or bridge piers during flooding events can be considered surface piercing obstacles, as they are typically not fully submerged. Because of this, the drag force does not accurately describe the hydraulic loading of such structures during extreme flood events. Qi et al. (2014) conducted a study on the loading due to a free surface channelized flow onto a column. Two types of flow were defined: choked flow and subcritical flow. Choked flow is defined by an increase in water depth upstream of the structure and a decrease in water depth downstream of it. The changes in water depth upstream and downstream of the structure result in an increase in the hydrostatic pressure acting in the flow direction, which then results in increased loading acting on the column. In their study, the stream-wise force acting on the flow obstacle was termed the *resistance force* (Qi et al., 2014):

$$F_R = \frac{1}{2} C_D \rho_f B h u^2 + \frac{1}{2} C_H \rho_f g B \left(h_u^2 - h_d^2\right) \tag{4.2}$$

where C_H is the hydrostatic coefficient, h_u is the water depth upstream of the column, and h_d is the water depth directly downstream of the column. Due to the difficulties associated with determining the hydrostatic coefficient, Chaplin and Teigen (2003) also defined the resistance force as:

$$F_R = \frac{1}{2} C_R \rho_f B h u^2 \tag{4.3}$$

where C_R is the resistance coefficient. The resistance coefficient is a dimensionless quantity used to define the hydrodynamic efficiency of objects.

Chaplin and Teigen (2003) investigated the resistance coefficient of towed columns in steady flows and concluded that the resistance coefficient is a function of the Froude number. Similarly, Arnason (2005) concluded that the resistance coefficient is a function of the Froude number when studying various columns impacted by dam-break bores. In addition, the resistance coefficient increased with a decrease in the impoundment depth and with a decrease in the flow depth to column width ratio, as this resulted in greater flow redirection. When analyzing the resistance coefficient of debris dams, Stolle et al. (2018a) found that the coefficient was a function of the product of the Froude number and Reynolds number. However, there were some discrepancies in the relationship between the force coefficients and the Froude-Reynolds number. Stolle et al. (2018a) stated that this could be attributed to the unknown porosity of the debris dams that were tested, as it was assumed in the calculations of the resistance coefficient that there was no dam porosity due to difficulties associated with determining the voids of the dam models. The porosity of a debris dam reduces the cross-sectional area exposed to the flow, which, in its turn, could reduce loading associated with debris dams.

When reviewing literature regarding debris damming, it was found that research has primarily been conducted for steady-state flow conditions. In extreme flooding events such as tsunamis or storm surges however, transient conditions typically prevail. In such conditions, it is currently not clear as to how large the maximum force due to debris damming develops in these conditions. Furthermore, research regarding debris damming has particularly focused on debris dam formation and the associated scour effects, while little research on the loading behaviour of debris dams. Further research regarding the loading due to debris dams in transient flow conditions is required to better understand debris dam loading in complex flow conditions.

This study hence investigates debris damming loads on structures in transient flow conditions and focusses on dam characteristics using idealized debris dam properties. These debris dams were attached to a column subjected to dam-break waves generated by the rapid release of water in a reservoir with varying impoundment depths. The dam-break waves were utilized as they were demonstrated to reasonably model the hydrodynamics of on-land tsunami bores (Chanson, 2006). The idealized debris dams varied in terms of debris dam shape, height, and porosity. The ultimate goal of this study is to assist in the development of engineering guidelines for extreme flood events. To the authors' knowledge, this is the first study that uses idealized debris dams tested in *transient flow conditions*. The specific objectives of this study are:

- To investigate the loading due to debris dams and the effect on loading of the debris dam geometry, including dam shape, dam height, and porosity.
- To analyze the influence of varying debris dam geometries on resistance force coefficients.
- To provide a range of values of the resistance force coefficients in terms of debris dam geometry and the flow conditions.

This project utilizes idealized debris dams deliberately so that the variables investigated can be isolated and quantitatively compared. The variables in this study include three different flow conditions based on three impoundment depths, two debris dam shapes, three dam heights, and three dam porosities. As mentioned, transient flow conditions were utilized as there is a significant gap in research regarding debris damming loads in extreme flooding events.

This paper is organized as follows: Section 2 presents the experimental setup, which describes the test facilities at the University of Ottawa, the instrumentation used, and the characteristics of the various debris dams tested. Section 3 presents the results of the tests including the hydrodynamics, the resistance forces, and the resistance coefficients and their relationship to the debris dam properties. Section 4 discusses the results while Section 5 presents the conclusions stemming from this study.

4.2 Experimental Setup

4.2.1 Experimental Facility

This experimental program was conducted in the Dam-Break Flume at the University of Ottawa, Canada. This flume utilizes a rapidly opening swing gate, which is used to generate dam-break waves with well-controlled hydraulic characteristics (Stolle et al, 2018b; Häfen et al, 2019). The flume is 30.0 m long, 1.5 m wide, and 0.80 m deep, as illustrated in Figure 4.1. The corresponding locations of the instruments placed around the model column are listed in Table 4.1. The reservoir extends 22.0 m upstream of the gate and the model test section is installed on an 8.5 m long false floor. A smooth acrylic cylinder was used to represent a structural column. The cylinder was attached at its upper end to a load cell, which was itself mounted onto a rigid instrument bridge firmly attached to the side flume walls. Three various impoundment depths (h_o) in the reservoir upstream of the swing gate were tested to produce varying flow conditions. The impoundment depths were 0.3, 0.4, and 0.5 m.

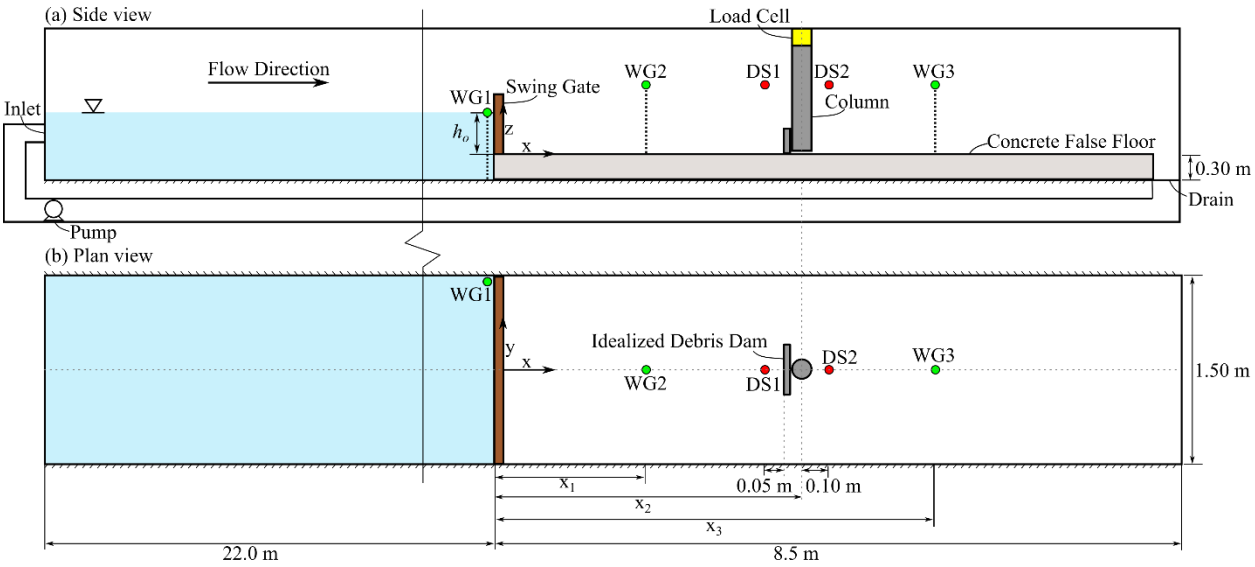

Figure 4.1: The experimental set-up in the University of Ottawa Dam-Break Flume: (a) side view; (b) plan view.

Table 4.1: Location of the instruments for each test using a different impoundment depth.

Impoundment depth, d (m)	x_1 **(m)**	x_2 **(m)**	x_3 **(m)**
0.3	1.5	3.0	4.2
0.4	2.0	4.0	5.6
0.5	2.5	5.0	7.0
Non-dimensional Distance	5.0	10.0	14.0

4.2.2 Swing Gate

Broken tsunami waves inundating the coastline are commonly modelled using a dam-break wave as it was shown to be similar to the behaviour of an on-land tsunami bore (Chanson, 2006). The experiments conducted in this study used a rapidly opening hinged swing gate to generate the dam-break wave through the sudden release of a volume of water impounded behind it. Gate opening times were carefully controlled such that the opening process would not influence the generation of proper dam-break waves (Stolle et al., 2018b; Häfen et al., 2019). The gate was built of marine plywood attached to a rigid steel frame. A watertight seal was placed around the steel frame of the gate to ensure that there was no leakage of water from the reservoir. The gate was 0.80 m high and 1.40 m wide. The maximum impoundment depth (h_o) used was 0.50 m due to the depth restrictions of the flume. The gate is locked while the reservoir is filling to the desired impoundment depth. Once this impoundment depth is achieved, the gate opening mechanism was manually released. At each impoundment depth, 15 repetitions were conducted with no column installed to ensure that the dam break wave was repeatable, which is further discussed in Section 3.1.

4.2.3 Instrumentation

Several instruments were utilized to allow the recording of data needed to develop a better understanding of debris damming loads – these instruments are listed in Table 4.2. All the instruments were connected to a data acquisition system to ensure that all data was time synchronized. Three capacitance wave gauges and two ultrasonic distance sensors were used to record the water depths along the propagation direction of the dam-break wave. The locations of the wave gauges and distance sensors ae shown in Figure 4.1. The locations of the instruments varied, depending which impoundment depth was tested, such that the distances from the swing gate were non-dimensionalized. The positions of the instruments based on the impoundment depths and non-dimensional distances are listed in Table 4.1.

Table 4.2: List of the instruments used in the experimental tests.

Instrument / Manufacturer	**Model**	**Sampling Rate (Hz)**	**Accuracy (±, %)**	**Instrument designation**
Ultrasonic Distance Sensor (DS) / MasaSonic PulStar	M-5000/ 220	300	0.25	DS1, DS2
Capacitance Wave Gauge (WG)	WG-50	300	0.4	WG1, WG2, WG3
6-Axis Load Cell / Interface	6A68	300	0.1	LC
Acoustic Doppler Velocimeter (ADV) / Nortek	Vectrino	200	0.5	ADV
Data Acquisition System (DAQ) / HBM GmbH	QuantumX MX440B and MX840B	-	-	-

An Acoustic Doppler Velocimeter (ADV) was utilized to record the flow velocities. The ADV was only used when no debris dam or column were present and was installed at the location at which the column was to be located. The ADV recorded at three various flow depths, which were 60, 50, and 40 percent of the theoretical flow depth at each location for the three impoundment depths (Chanson, 2006). The velocity data was filtered using the Wavelet Thresholding Method, developed by Donoho and Johnstone (1994), which was done by using the *wmulden* function in MATLAB (MathWorks, 2019). This filter is commonly

used to filter ADV data (Goring and Nikora, 2002; Razaz and Kawanisi, 2011) and is beneficial due to its ability to work with non-stationary data.

A 6-axis load cell was utilized to record the total forces (in *x*-, *y*-, and *z*-direction), as well as the total moment (with respect to axis *x*, *y*, and *z*) acting on the column and debris dams. The load cell was attached to the top of the column, which in turn was firmly attached to a rigid mounting bridge. The data from the load cell was filtered using a time-varied Empirical Mode Decomposition (EMD) filter to remove signal noise from the force data (Huang et al., 1998; Li et al., 2017). This filter is beneficial due to its ability to work well with non-stationary data, which characterizes the force-time history recordings. The authors also manually checked to ensure that the filtered data contained the proper information recorded by the load cell, with no significant alterations other than removing signal noise. Particular care was laid to ensure retaining the maximum forces contained in the force signals.

4.2.4 Idealized Debris Dam Specimens

Several variations of debris dam specimens were manufactured and then tested to develop a further understanding of the impacts of debris dam geometry on the column loading. A rigid acrylic cylinder was utilized to represent a column. The cylinder had an outer diameter of 0.09 m and an inner diameter of 0.068 m. The debris dams were attached to the column using a metal collar. The debris dams varied in terms of shape, height, and porosity. Two debris dam shapes were tested: one was in the form of a rectangular dam and a second type in the form of a semi-cylindrical dam, as shown in Figure 4.2. The rectangular dams were used to represent rigid debris forming a rectangular shape while the semi-cylindrical dams represented an agglomeration of malleable debris accumulating around a structure. The rectangular dams were constructed of acrylic plastic plates and the nonporous cylindrical dams were constructed of acrylic plastic semi-cylinders. The porous cylindrical dams were constructed of aluminum semi-cylinders for constructional purposes associated with drilling the holes to model their porosity. All plates were 0.013 m (0.5 inches) thick. The semi-cylindrical dams were 0.09 m thick, resulting in an external radius of 0.135 m. All debris dams had a width of 0.27 m, which is a multiple of three times the column diameter. The width of debris dam is dependent on the debris supply so the choice of debris dam width was arbitrary (Stolle et al., 2018a).

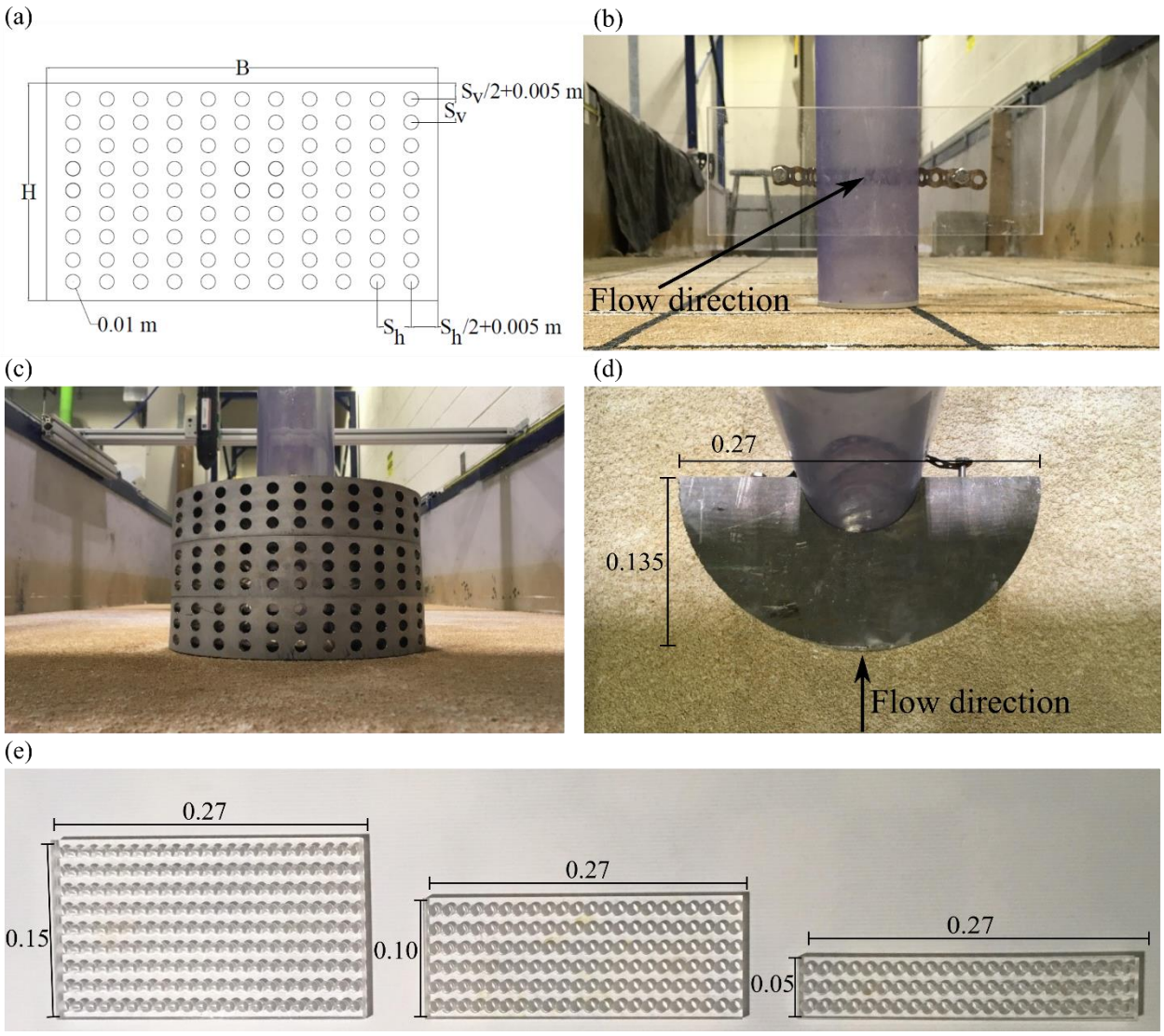

Figure 4.2: Debris dam specimens utilized in the experimental test (all dimensions in the figures are in meters): (a) spacing of the holes of the porous dams; (b) rectangular debris dam attached to the column with the flow direction; (c) front view of porous cylindrical debris dam; (d) top view of cylindrical debris dam; (e) various heights of debris dams utilized in experimental tests.

The three dam heights were used: 0.05 m, 0.10 m, and 0.15 m. The debris dams with the height of 0.05 and 0.10 m were suspended so that the top of the debris dam was at 0.15 m from the flume floor, illustrated in Figure 4.2 (b). To create the porous dams, circular holes were drilled parallel to the flow direction. The dam porosities (*n*) were calculated as the ratio of the sum of all cross-sectional areas of the circular holes to the total cross-sectional area of the debris dam surface perpendicular to the flow direction. The three various porosities that were used were 0.0, 0.2, and 0.4. The diameter of the holes was 0.01 m. This smaller hole size was chosen as smaller holes are more likely to form in debris dams as larger voids result in dam instability (Stolle et al., 2017). The spacing of the holes is illustrated in Figure 4.2 (a) and described in Table 4.3. A summary of all of the debris dam specimens is listed in Table 4.4.

Table 4.3: Spacing of holes for porous debris dams.

	Porosity (n) = 0.2		n = 0.4	
Dam Height (m)	**Vertical hole spacing, S_v (mm)**	**Horizontal hole spacing, S_h (mm)**	**Vertical hole spacing, S_v (mm)**	**Horizontal hole spacing, S_h (mm)**
0.15	16.0	23.3	16.0	12.2
0.10	15.7	23.3	15.7	12.2
0.05	15.0	23.3	15.0	12.2

4.2.5 Experimental Protocol

An experimental protocol was designed and implemented to ensure the repeatability of the experiments conducted. There were two sets of experiments conducted: the first tests were conducted with no column or debris dams installed in the flume to assess the hydrodynamic conditions and to analyze the repeatability of the experiments. For this set of experiments, three capacitance wave gauges and one distance ultrasonic sensor recorded the flow depths throughout the testing area. The ADV was installed at the centre of the location of where the column was later installed for the second experiments. The ADV recorded at various flow depths generated by each impoundment depth. Five repetitions were conducted for each flow depth at each impoundment depth, resulting in 45 tests when no column/ debris dam were present. The second set of tests were conducted with the obstacle (column/ debris dam) installed. These tests utilized the three capacitance wave gauges, the two distance ultrasonic sensors, and the load cell. Tests were initially completed with only the column installed (no debris dam attached to it). Five repetitions for each impoundment depth were conducted with only the column present. The tests were then completed with the various debris dams attached to the column. Three repetitions were completed using each debris dam, as shown in Table 4.4, for each impoundment depth. For all tests, the DAQ system was initiated to record and then the lift gate was opened (Stolle et al., 2018b). The gate opening time was determined for each test using a change in the water level at the location of the gate, based on the recording of WG1. The moment of gate opening is defined as the 0.0 seconds (time origin) in the time-histories of all results. The DAQ system recorded for a minimum of 60 seconds for each test.

Table 4.4: Variations of idealized debris dams used in the experimental tests.

Type of Dam	Dam Height, H (m)	Dam Width, B (m)	Dam Porosity, n (-)
	0.15	0.27	0
	0.10	0.27	0

Rectangular	0.05	0.27	0
	0.15	0.27	0.2
	0.10	0.27	0.2
	0.05	0.27	0.2
	0.15	0.27	0.4
	0.10	0.27	0.4
	0.05	0.27	0.4
Cylindrical	0.15	0.27	0
	0.10	0.27	0
	0.05	0.27	0
	0.15	0.27	0.2
	0.10	0.27	0.2
	0.05	0.27	0.2
	0.15	0.27	0.4
	0.10	0.27	0.4
	0.05	0.27	0.4

4.2.6 Resistance Force Coefficients

The time-history of the resistance coefficient was calculated for each test using Equation (4.3). The relevant resistance force used for the computations was the force time-history in the *x*-direction for each idealized debris dam and the flow velocity was the time-history of the mean stream-wise velocity recorded when no obstacle was installed in the flume. The cross-sectional area was calculated using the time-history of the mean water depth recorded when no obstacle was installed in the flume. This was utilized to be consistent with the mean flow velocity that was applied. The width used to determine the cross-sectional area is a depth-averaged width based on the time-history of water depth and the width of the debris dam and column. Two resistance coefficients were calculated: the first one is the *bulk resistance coefficient* (C_{RB}). The cross-sectional area utilized to calculate the bulk resistance coefficient does not account for the porosity of the dams. This resistance coefficient was proposed due to the difficulties associated with determining the

expected porosity of debris dams during the design process. The bulk resistance coefficient and the bulk cross-sectional area applied, respectively, are:

$$C_{RB} = \frac{2F_R}{\rho_f A_B u^2} \tag{4.4}$$

$$A_B = (h - H)D + HB \tag{4.5}$$

where h is the water depth, H is the debris dam height, D is the diameter of the column, and B is the debris dam width.

The second resistance coefficient calculated is the *effective resistance coefficient* (C_{RE}). The cross-sectional area utilized to calculate the effective resistance coefficient was obtained by subtracting the porous area from the total cross-sectional area of the debris dam. This resistance coefficient was determined to assess the impact of the dam porosity. The effective resistance coefficient and the effective area, respectively, are:

$$C_{RE} = \frac{2F_R}{\rho_f A_E u^2} \tag{4.6}$$

$$A_E = (h - H)D + HB - nHB \tag{4.7}$$

where n is the dam porosity.

4.3 Results

4.3.1 Hydrodynamics

The transient flow conditions were modelled using a dam-break wave: as previously mentioned, this method is commonly used to represent on-land tsunami bores (Chanson, 2006). The waves were generated using a rapidly opening swing gate, in an experimental facility that had previously been proven to effectively model dam-break waves (Stolle et al., 2018b; Häfen et al., 2019). Hydrodynamic tests with no debris dam model and column installed were conducted to evaluate the unobstructed hydrodynamic conditions created in the flume. The water depth was recorded at several locations throughout the testing area. The standard deviation of the water depth was assessed using the data from the hydrodynamic tests to assess repeatability, illustrated in Figure 4.3 (a). The standard deviation for the water depth was 0.0068 m, based on the 15 tests conducted for each of the flow conditions. Given the low value of the standard deviation, the results of the tests could hence be considered highly repeatable. The local velocity in the *x*-, *y*-, and *z*-axis was recorded using an ADV at three water depths for each individual impoundment depths used. The mean velocities were calculated using a depth-averaged mean of the recorded velocities in the propagation direction (*x*-velocity), which are shown in Figure 4.3 (b). Due to problems associated with ADVs utilized in aerated or

turbulent flow (Mori et al., 2007), the initial velocity data recorded had a low signal-to-noise ratio. Therefore, theoretical values proposed by Leal et al. (2006) were calibrated to the recorded velocities once adequate signal to noise ratios were obtained. The velocities were calibrated by determining the roughness as proposed by Leal et al. (2006) that best fitted the flow velocities based on the lowest error between the calibrated curves to the adequate velocity data. The theoretically-derived velocity values were used in the analysis until the maximum velocity recorded by the ADV matched the theoretical ones. The bore front velocity was derived from finite difference analysis of arrival time at consecutive wave gauges and was also plotted as solid circles in Figure 4.3 (b), illustrating that the theoretical velocity compared well with the recorded results.

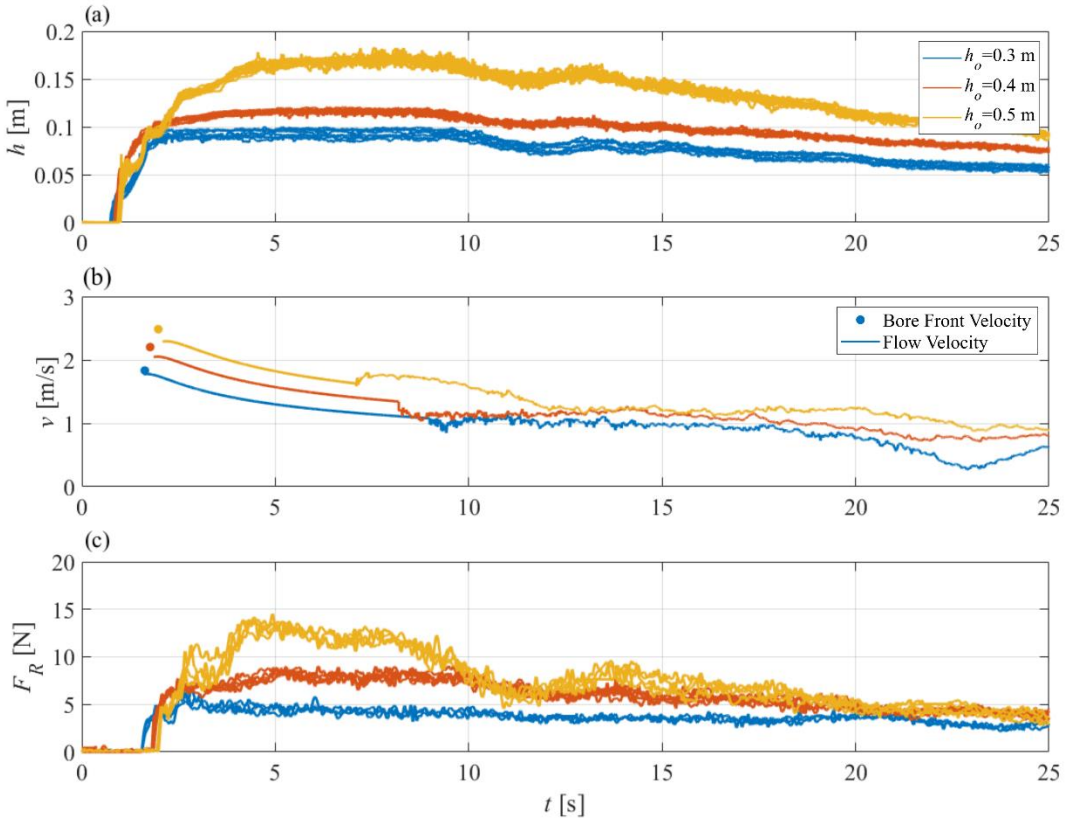

Figure 4.3: Time-history of experimental parameters; (a) time-history of the flow depth for each impoundment depth from WG3 for 5 repetitions; (b) time history of the average, stream-wise flow velocity (x-axis) and the bore front velocity for each impoundment depth; (c) time-history of the stream-wise force with only the column present for each impoundment depth for 3 repetitions.

Flow velocities observed from the filtered ADV data ranged from 0.7 to 1.9 m/s. When no obstacle (column/ debris dam) was installed in the flume, the water depth ranged from 0.0 to 0.18 m throughout the hydrodynamic tests. This results in a range of Reynolds numbers from 7.62×10^4 to 4.87×10^5, where the characteristic length is the instantaneous water depth, and Froude numbers varying between 0.92 and 1.56 (calculated using instantaneous water depth and velocity). Froude numbers observed in real-world tsunami

events ranged between 0.6 to 2.0 (Fritz et al., 2006; Matsutomi and Okamoto, 2010). The experimental tests reported in this work were scaled using Froude similitude with a 1:30 geometric scale. At prototype scale, this results in velocities ranging from 4.7 to 9.0 m/s. This is comparable to flow velocities (3 to 8 m/s) observed by Matsutomi et al. (2006) in the 2004 Indian Ocean Tsunami. The observed water depths with no obstacles present scale up to 5.4 m at prototype scale, which is within the range of water depth of up to 9 m observed in the 2004 Indian Ocean Tsunami (Borrero, 2005). The results pertaining to the hydrodynamic conditions of the generated dam-break waves with no debris dam or column present illustrate that they were repeatable and were scaled adequately so that the loading due to debris damming could be properly assessed in these testing conditions.

The fluid-structure interaction of the nonporous dam of 0.15 m is illustrated in Figure 4.4, which displays the same expected behaviour as that outlined by St-Germain et al. (2014) and Derschum et al. (2017). There is initial splash-up that occurs upon the bore's arrival at the structure. The bore then begins to develop rotational motion with a horizontal axis upstream of the column, resulting in a reduction of the forward velocities and the generation of vertical velocities along the column's/ debris dam's front. This rotational motion begins to form a surface roller upstream of the debris dam and column. Eventually there is upstream propagation of the surface roller, which can cause negative (return) horizontal velocities directly upstream of the column/ debris dam.

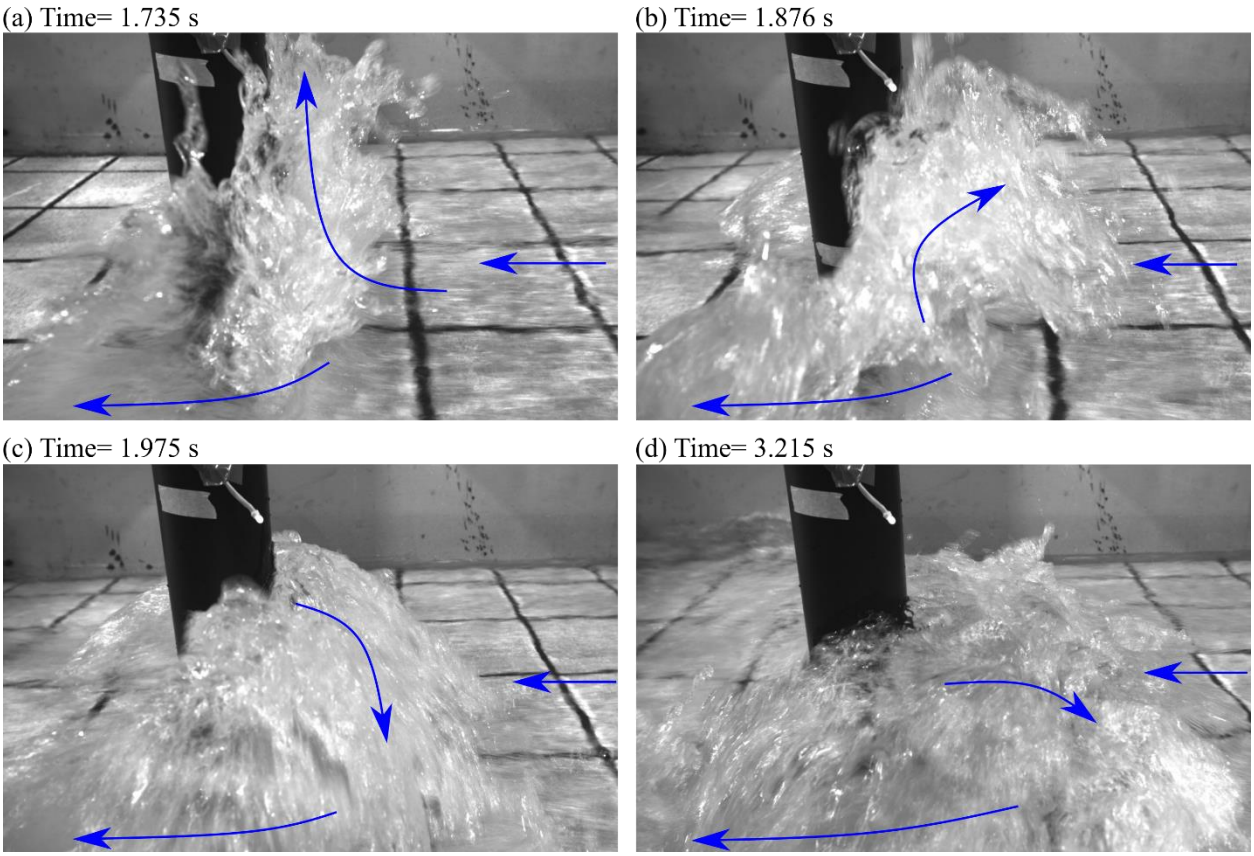

Figure 4.4: Bore-structure interaction with the rectangular dam attached to the column: (a) initial splash up; (b) development of negative wave motion; (c) formation of the surface roller; (d) fully formed surface roller with horizontal axis.

4.3.2 Resistance Forces

The time-history of the stream-wise force recorded by the load cell attached at the top of the column was termed *resistance force* and was recorded for all debris dams tested. The mean of the resistance forces was determined starting with 7.0 seconds after the time of the wave arrival, as this is the time when the upper reservoir boundary is reached, as described by Lauber and Hager (1998). The mean forces were compared to the mean product of the Froude number and water depth to obstacle width ratio, $Fr\frac{h}{w}$, 7.0 seconds after wave arrival, which is illustrated in Figure 4.5. The resistance forces and resistance coefficients were compared to the Froude number-water depth to obstacle width ratio as it has been shown that the resistance coefficient is a function of these variables (Arnason, 2005; Asadollahi et al., 2018) This was preferred over the comparison of the Froude-Reynolds number product used by Stolle et al. (2018a).

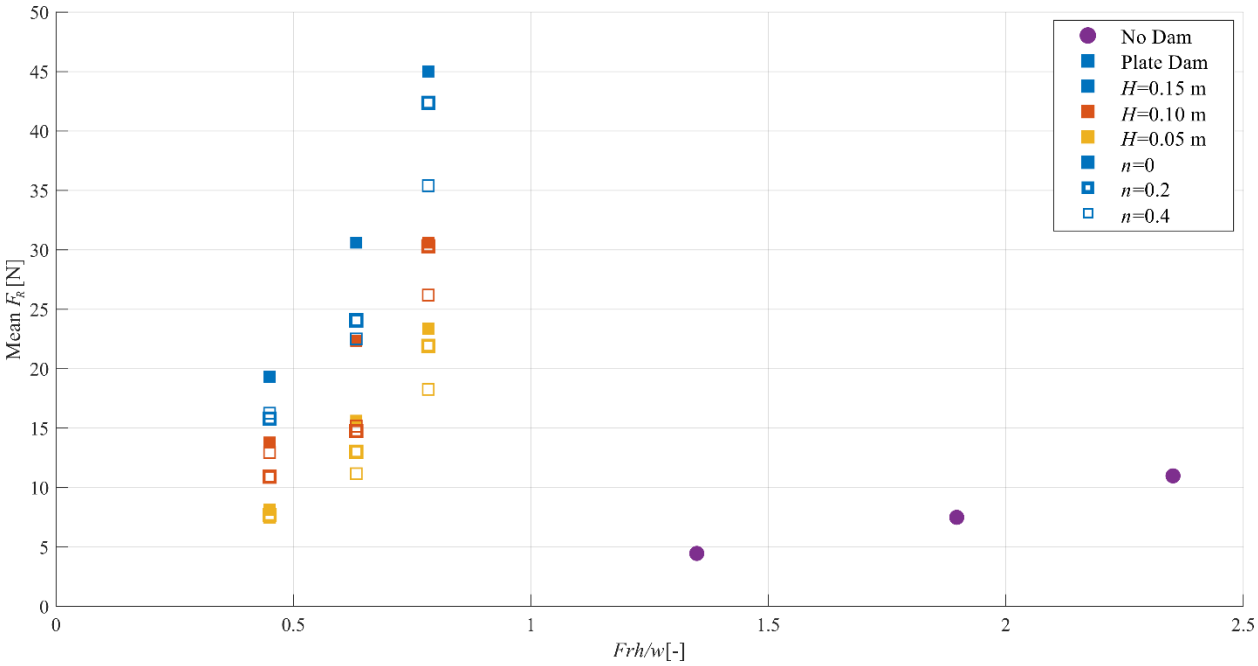

Figure 4.5: The mean resistance forces versus the Froude number-water depth to obstacle width ratio for tests with rectangular debris dams. The marker shape represents the dam shape, the various colours represent the dam height, and the marker thickness/ fill represents the various porosities used.

Due to the low standard deviations and similarity exhibited by the resistance force for each flow obstacle at each impoundment depth (Figure 4.3 (c)), the mean of the time-history for the three repetitions of each idealized debris dam was determined and used for all calculations of the resistance force and resistance coefficients. The comparison shown in Figure 4.5 suggests that the mean resistance force generally increases with an increase in $Fr\frac{h}{w}$. As $Fr\frac{h}{w}$ is a function of the flow velocity and water depth this is expected because the resistance force is a function of the square of the velocity and the depth over which the obstacle is exposed to. The presence of the debris dam results in a significant increase in the resistance force acting on the column-debris dam system, due to a greater cross-sectional area exposed to the flow. The rectangular dam resulted in greater resistance forces compared to the cylindrical dam with the same area exposed to the flow since dam curvature yielded a stagnation point closer to the column axis, thus necessitating a larger lateral acceleration of the flow. It is well-known that rectangular objects are less hydrodynamically-efficient compared to cylindrical objects resulting in greater resistance forces. As expected, the resistance force was found to be proportional to the dam height and inversely proportional to the dam porosity, as the resistance force is a function of the cross-sectional area exposed to the flow.

A multiple linear regression of the resistance force was completed using MATLAB to determine the influence of the independent variables on the resistance force The resistance force was assessed in terms of $Fr\frac{h}{w}$, dam curvature (κ), relative dam height ($\frac{H}{h}$), and porosity (n), as these were the variables tested in this

study. The curvature of the debris dams was used to allow for a quantitative comparison between the debris dam shapes. The curvature of the rectangular debris dams was 14.75 while the curvature of the semi-cylindrical ones was 7.41. The relative dam height was defined as the ratio of the dam height to the mean water depth for each corresponding impoundment depth measured when no column/ debris dam was installed. This was determined such that all independent variables used in the regression were non-dimensionalized. A multiple linear regression was also completed using standardized variables so that their influence on the resistance force could be compared, through the use of *z*-scores (De Smith, 2018). The *z*-score determines the number of standard deviations that a parameter is away from the mean of a given data set. By determining the *z*-score of the independent variables, the values of the regression coefficients can be compared to each another to assess the influence of independent variables on the dependent variables. The results of the regressions and the R^2 values are listed in Table 4.5.

Table 4.5: Coefficients of the multiple linear regression for the resistance forces.

	Intercept	***Frh/w* (-)**	κ	***H/h* (-)**	***n* (-)**	R^2
F_R	-38.35	64.28	0.73	12.70	-10.22	0.87
F_R **(standardized)**	19.48	8.93	2.67	5.39	-1.69	0.87

The regression coefficients listed in Table 4.5 indicate that the resistance force is proportional to $Fr\frac{h}{w}$, the dam height, and the curvature of the dams and that the resistance force is inversely proportional to the porosity. The standardized regression results illustrate that flow conditions and the dam height have a more significant impact on the resistance force in comparison to effect of the porosity and the curvature of the dams. Although dam porosity and dam height result in a change in the cross-sectional area of the flow obstacle, the porosity likely results in lesser impacts on the resistance forces due to the friction forces created by the holes. This likely results in an increase in resistance forces, counteracting the equivalent reduction in the cross-sectional area.

4.3.3 Resistance Coefficients

The bulk and effective resistance coefficient were determined for each test. The mean of the bulk resistance coefficient and effective resistance coefficient were calculated starting from 7.0 seconds after wave arrival and were compared to $Fr\frac{h}{w}$, as shown in Figure 4.6 and Figure 4.7. Due to the low standard deviations for the results of each debris dam type, the mean of the time history for the repetitions testing each idealized debris dam was determined and used for the presentation of the resistance coefficients.

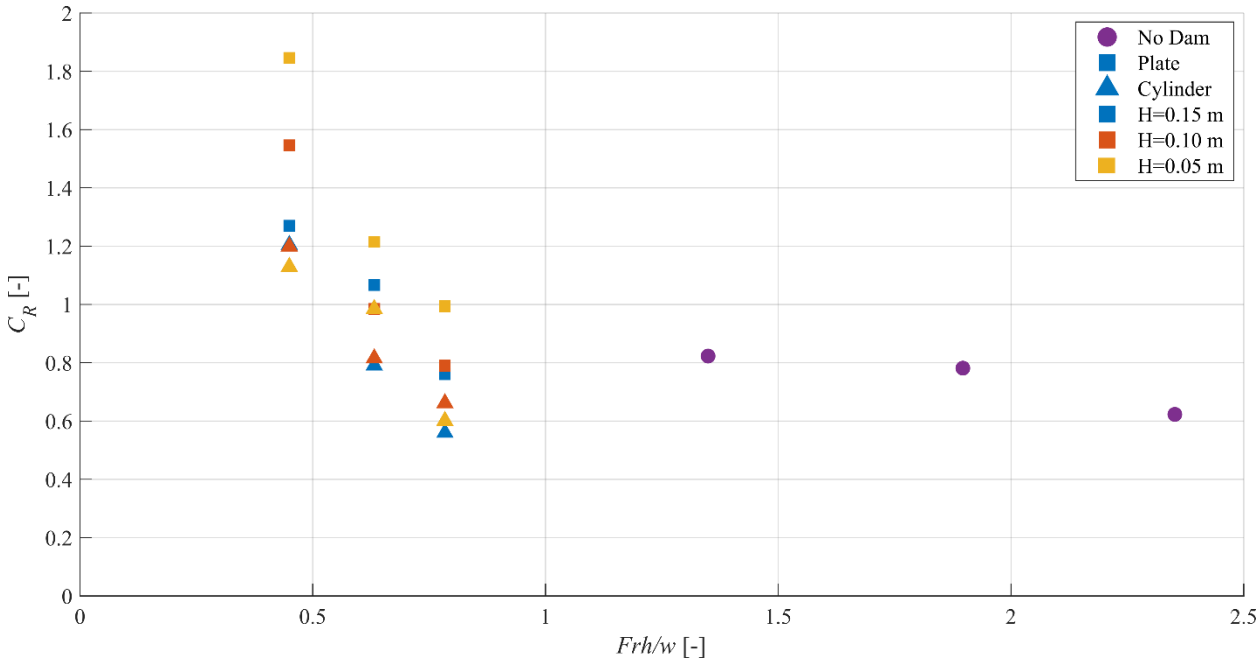

Figure 4.6: The resistance coefficient versus the Froude number-water depth to obstacle width ratio illustrating the effects of dam height. Only the nonporous dams are included in this plot. The various marker shapes indicate the dam shape and the various marker colours indicate dam height.

To compare the impact of the variables on the resistance coefficients, Welch's *t*-tests were conducted. Welch's *t*-tests were utilized as they determine if there is a quantitative difference on the influence of two different independent variables of unequal variances. The null hypothesis in this study is that the mean difference of the paired variables is equal to zero. Lower probabilities indicate that the paired variables influence the resistance coefficient. Welch's *t*-test also provides a statistical and critical *t*-value. The statistical *t*-value (t_{Stat}) is equal to the mean of the differences between resistance coefficients for the corresponding variables divided by the sample variance and the critical *t*-value. The critical *t*-value ($t_{critical}$) is based on the assigned confidence interval of 90%. When the absolute statistical *t*-value is greater than the critical *t*-value, there is 90% probability of the null hypothesis occurring. The results of the *t*-tests are listed in Table 4.6 to Table 4.9.

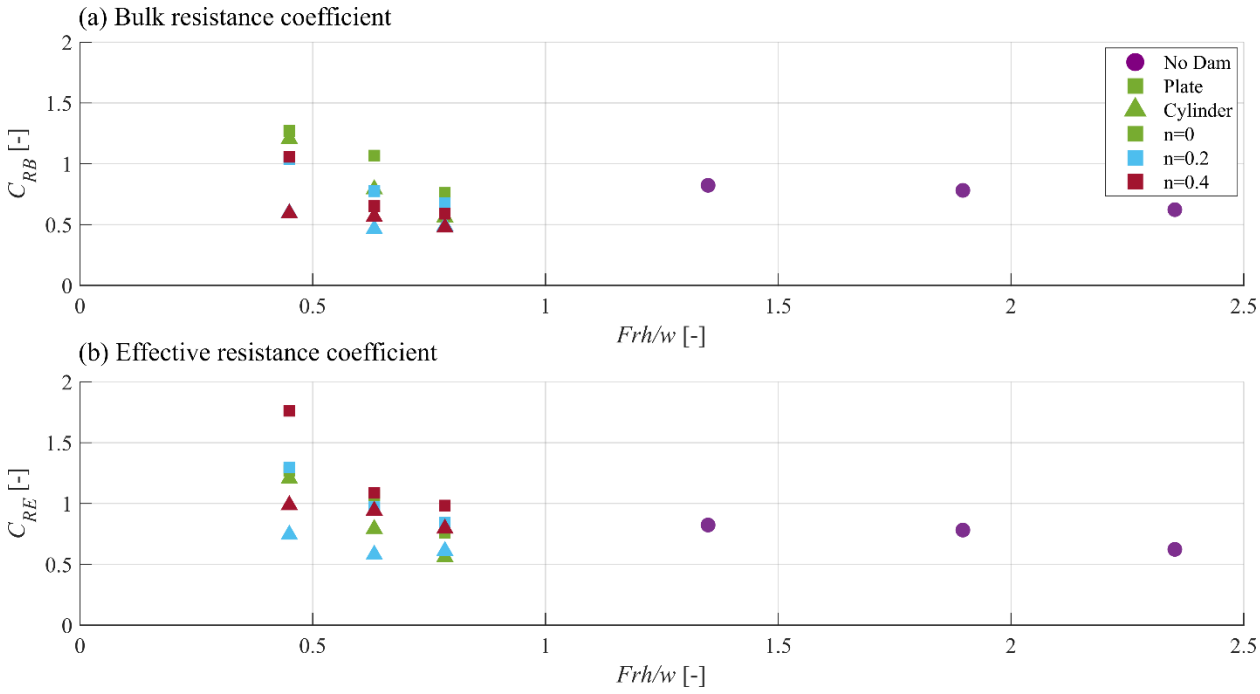

Figure 4.7: The resistance coefficient versus the Froude number-water depth to obstacle width ratio illustrating the effects of dam porosity: (a) the bulk resistance coefficient; (b) and the effective resistance coefficient. Only the dams of H=0.15 m are included in this plot. The various marker shapes indicate the dam shape and the various colours indicate dam porosity.

4.3.3.1 Flow Conditions

It can be observed that both the bulk and effective resistance coefficient decrease with increasing $Fr\frac{h}{w}$, as shown in Figure 4.6 and Figure 4.7. This is expected, as the resistance coefficient is a function of the Froude number and the water depth to obstacle width ratio (Arnason, 2005). Table 4.6 also illustrates a decrease in the resistance coefficient with an increase in the impoundment depth. This has been previously observed by Arnason (2005) and Asadollahi et al. (2018) on columns subjected to dam-break waves generated by the release of water with impoundment depths.

Table 4.6: Results of the Welch's t-tests conducted corresponding to results from the three impoundment depths.

Variables	**Variables Compared**	***P* (-)**	t_{stat}	$t_{critical}$	**90% Confidence**
C_{RB}	h_o=0.3 m, h_o= 0.4 m	0.002	3.356	1.706	Yes
	h_o=0.3 m, h_o=0.5 m	0.000	2.959	1.697	Yes
	h_o=0.4 m, h_o=0.5 m	0.006	5.374	1.721	Yes
C_{RE}	h_o=0.3 m, h_o= 0.4 m	0.002	3.356	1.706	Yes

	h_o=0.3 m, h_o=0.5 m	0.002	3.300	1.691	Yes
	h_o=0.4 m, h_o=0.5 m	0.000	4.809	1.717	Yes

4.3.3.2 Debris Dam Shape

The plots of the resistance coefficients show that the resistance coefficient increases in the presence of the debris dams. Aside from the reduced hydrodynamic efficiency of a rectangular or semi-cylindrical shape of the debris dams used, they have a lesser flow depth to width ratio relative to the column, resulting in greater flow redirection (Arnason, 2005). The *t*-test indicates that the rectangular dams result in greater resistance coefficients relative to the cylindrical dams of the same dam properties (Table 4.7). As mentioned, this is expected as rectangular objects are typically less hydrodynamically-efficient relative to semi-cylinders.

Table 4.7: Results of the Welch's t-tests conducted comparing the debris dam shape for the same area exposed to the flow.

Variables	**Variables Compared**	***P* (-)**	t_{stat}	$t_{critical}$	**90% Confidence**
C_{RB}	Rectangular and Cylindrical	0.002	-3.317	1.681	Yes
C_{RE}	Rectangular and Cylindrical	0.000	-3.977	1.683	Yes

4.3.3.3 Debris Dam Height

The height of the dams did not have a significant influence on the resistance coefficients, as demonstrated by the *t*-tests (Table 4.8). This can be expected as the resistance coefficient is normalized by the cross-sectional area of the dam. The *t*-test for the bulk resistance coefficient shows that there is an increase in the bulk resistance coefficients from the dams with a height of 0.15 m to heights of 0.05 m. In addition, when comparing dams of similar properties with the varying dam heights in Figure 4.6, the resistance coefficient is greater for dams of lesser height. This is attributed to the increased runup observed in the case of dams of greater height. The resistance force is a function of the squared velocity and the water depth. Flow obstacles placed in the path of dam-break waves induce the formation of a surface roller on their upstream side, as illustrated in Figure 4.4. Surface rollers can result in negative (return) horizontal flow velocities (St -Germain et al., 2014; Derschum et al., 2017), reducing the resistance forces acting on the debris dam, as shown by Stolle et al. (2017). Therefore, the observed surface rollers could result in greater resistance coefficients for dams of decreasing height.

Table 4.8: Results of the Welch's t-tests conducted comparing debris dam height.

Variables	Variables Compared	P (-)	t_{stat}	$t_{critical}$	90% Confidence
C_{RB}	H=0.15 m, H=0.10 m	0.230	-1.222	1.691	No
	H=0.10 m, H=0.05 m	0.200	-1.309	1.694	No
	H=0.15 m, H=0.05 m	0.021	-2.424	1.696	Yes
C_{RE}	H=0.15 m, H=0.10 m	0.452	-0.761	1.691	No
	H=0.10 m, H=0.05 m	0.760	-0.308	1.691	No
	H=0.15 m, H=0.05 m	0.293	-1.067	1.691	No

4.3.3.4 Debris Dam Porosity

The dam porosity progressively decreases the bulk resistance coefficient from n=0 to n=0.2 and 0.4 (Figure 4.7 (a)). This result is expected as the cross-sectional area utilized to determine the bulk resistance coefficient does not account for porosity. The porosity results in a significant decrease in the blockage of the flow, while the cross-sectional area remains the same as a nonporous dam, decreasing the bulk resistance coefficient. However, there is not a significant change in the bulk resistance coefficient from n=0.2 to n=0.4 (Table 4.9). Although there is a decrease in cross-sectional area by 20 percent, the decrease in blockage is lesser relative for n=0 comparing to n=0.2. In addition, the holes, which simulate the porosity of the debris dam, lessen the impact of porosity on the loading and the bulk resistance coefficient due to added skin friction.

Porosity has no significant impact on the effective resistance coefficient, as illustrated in Table 4.9. Subtracting the area of the porosity from the area used to calculate the effective resistance coefficients results in an inconsistent impact of the porosity on the coefficient. Although the presence of the holes decreases blockage and the cross-sectional area exposed to the flow, the presence of holes increases the skin friction of the dam and, that, in turn, increased the resistance force. This additional friction force created by the holes results in greater resistance forces compared to a dam with a reduced cross-sectional area of equivalent magnitude and no porosity.

Table 4.9: Results of the Welch's t-tests conducted comparing debris dam porosity.

Variables	Variables Compared	P (-)	t_{stat}	$t_{critical}$	90% Confidence

C_{RB}	n=0, n=0.2	0.080	1.808	1.692	Yes
	n=0.2, n=0.4	0.642	0.469	1.691	No
	n=0, n=0.4	0.035	2.190	1.691	Yes
C_{RE}	n=0, n=0.2	0.552	0.601	1.692	No
	n=0.2, n=0.4	0.225	-1.236	1.692	No
	n=0, n=0.4	0.565	-0.581	1.691	No

4.3.3.5 Overall Influence of the Variables

Multiple linear regressions were conducted to assess the influence of the variables on the resistance coefficients. The resistance coefficients were assessed in terms of $Fr\frac{h}{w}$, dam curvature, relative dam height, and porosity. The multiple linear regressions were, again, conducted using MATLAB. As outlined in Section 3.2, multiple linear regressions were also conducted using standardized independent variables by determining the *z*-score of each variable. The results of these regressions are listed in Table 4.10 below.

Table 4.10: Coefficients of the multiple linear regression for the bulk and effective resistance coefficients.

	Intercept	***Frh/w* (-)**	κ	***H/h* (-)**	***n* (-)**	R^2
C_{RB}	1.69	-1.43	0.037	-0.19	-0.69	0.621
C_{RB} **(Standardized)**	0.95	-0.20	0.13	-0.078	-0.11	0.621
C_{RE}	1.38	-1.22	0.040	-0.028	0.091	0.523
C_{RE} **(Standardized)**	1.08	-0.17	0.15	-0.011	0.015	0.523

The regressions utilizing the standardized variables show that all of the variables, other than porosity, have similar impacts on both the effective and bulk resistance coefficient. The regressions illustrate that increasing the Froude number and water depth to width ratio results in a decrease in the resistance coefficients, which has been observed in previous studies (Arnason, 2005; Asadollahi et al., 2018). The debris dam curvature has a similar effect on both the bulk and effective resistance coefficient, resulting in a significant increase in the coefficients, as expected because rectangular obstacles have greater resistance coefficients relative to cylindrical obstacles with the same area exposed to the flow (Arnason, 2005). The standardized regressions indicate that the flow conditions and dam shape have the largest overall impact on the resistance coefficient relative to the other variables. The standardized regressions also indicate that the

relative dam heights have little influence on both resistance coefficients, as shown previously by the Welch's *t*-tests (Table 4.8). This is expected as the resistance force is normalized by the cross-sectional area exposed to the flow of the debris dams. Increasing the debris dam height could result in decreasing resistance coefficients as greater surface rollers are observed in the case of dams with greater heights. Surface rollers can result in a decrease in flow velocities directly upstream of flow obstacles, therefore, resulting in a decrease in the drag force acting on the flow obstacle (St-Germain et al., 2014; Derschum et al., 2017). The dam porosity resulted in a large decrease in the bulk resistance coefficient whereas the porosity had little impact on the effective resistance coefficient. The bulk area used to calculate the bulk resistance coefficient does not account for the porosity, therefore, the porosity results in a decrease in loading. This will result in a decrease in the bulk resistance coefficient, whereas the cross-sectional area of the holes subtracted from the effective area results in an insignificant impact of the porosity on the effective resistance coefficient.

4.4 Discussion

In this study, the debris dam specimens utilized were secured to the column using a collar, fixing rigidly the debris dam to the column. The debris dams were modelled as stable debris dams because debris damming loads can be considered quasi-steady. However, in extreme flooding events, debris typically consist of buoyant materials (Matsutomi et al., 2006). This implies that debris dams could change position or their evolution with changing flow conditions and could hence potentially influence the magnitude of loading as well as that of the surrounding flow conditions. For submerged flow conditions at the debris dam site, runup that overtopped the debris dams was observed during testing. Hence, any potential debris dam could have experienced buoyant forces to restore its vertical force equilibrium.

A limitation of this study is that the porosity of the idealized debris dams was modelled by only using holes that were parallel to the flow direction. In reality, the porosity of debris dams has three-dimensional flow paths due to the random nature of debris dam accumulation, as well as a range of flow cross-sections within the debris dam. These random voids could reduce the impact of the porosity of the debris dams even further as three-dimensional flow paths could create greater skin friction and flow obstructions, increasing the resistance forces. It could also result in greater resistance coefficients of the porous debris dams, which is especially important when considering the bulk resistance coefficient. This study concluded that the bulk resistance coefficient decreased with the presence of porosity, as illustrated by the *t*-tests conducted for the bulk resistance coefficients. However, this may not have occurred had the debris dams been modelled with three-dimensional voids.

The debris dam specimens were constructed of two different materials. Rectangular dams and nonporous cylindrical dams were constructed of acrylic plastic while the porous cylindrical dams were constructed of aluminium due to constructability issues. Although both materials are relatively smooth, they have slightly different surface roughness, which could affect the resistance forces. However, as the drag force of cylinders and plates predominantly consists of pressure drag rather than skin friction it is assumed that these differences are insignificant (Nakayama and Boucher, 1998).

The experiments were scaled using Froude similitude so there may be scaling issues as the resistance coefficient is a function of the Reynolds number (Arnason, 2005). The Reynolds number achieved in this study ranged from 7.62×10^4 to 4.87×10^5. These values significantly exceed the Reynolds number of 1.25×10^4 in which the flow is fully turbulent, as stated by Chow (1959) and Bricker et al. (2015). However, the full range of Reynolds numbers in this study does not exceed the Reynolds number of 3×10^5 for the transition to turbulent flow of the boundary layer surrounding a cylinder (Kundu, 1990), which may affect the results. The maximum impoundment depth of this study is 0.5 m due to limitations associated with the flume height. Therefore, Reynolds numbers exceeding 3×10^5 could not be obtained for the full time series and the range of impoundment depths utilized given the experimental facilities.

4.5 Conclusions

This study investigated the loading due to debris dams in extreme flooding events. Several idealized debris dams with varying height, porosity, and shapes were tested. These debris dams were impacted by dam-break waves generated through the release of water impounded in a reservoir for three impoundment depths to assess the hydrodynamic loading of debris dams attached onto a column. Force coefficients including the bulk resistance coefficient and the effective resistance coefficient were determined to assess the impacts of debris dam geometries on loading conditions. Based on the results of the experimental campaign and analysis, several conclusions drawn from this study are:

- Increasing Froude number, water depth to obstacle width ratio, debris dam height, dam curvature, and decreasing porosity resulted in an increase in resistance forces acting on the debris dam and column.
- Increasing the dam curvature and decreasing the Froude number-water depth to obstacle width ratio resulted in an increase in the resistance coefficients.
- The dam porosity had inconsistent impacts on the effective resistance coefficient; however, the presence of holes reduced the bulk resistance coefficient.

- The dam height had negligible impacts on the resistance coefficients as the resistance force is normalized by the cross-sectional area of the obstacles.

The results of this study represent an initial investigation on the loading behaviour of debris dams and the influence of debris dam geometry on the loading. When trying to protect structures against the loading due to debris dams, the potential flow conditions should be well investigated. When there is little specific information regarding debris characteristics, as a conservative estimation, the debris dams should be considered to form over the full height of the flow depth and be nonporous. The variables tested in this study included three dam heights, three dam porosities, and two dam shapes tested in a dam-break wave of three impoundment depths. Additional research must be conducted to obtain a further understanding of the induced loads of debris dams by investigating more of the variables tested here as well as other variables, such as roughness, dam width, and dam length.

Chapter 5. Conclusions

5.1 Conclusions

A comprehensive physical modelling program was conducted to investigate the loading onto structures due to the presence of debris dams. This study utilized idealized debris dams suspended to a column tested in steady-state and transient flow conditions. The debris dam models varied in terms of geometry, where two dam shapes, three dam heights, and three porosities were tested in these experiments. The first set of experiments was conducted in steady-state flow conditions, with Froude numbers ranging from 0.37 to 0.61. The second set of experiments was conducted in transient flow conditions, tested in a dam-break wave, with Froude numbers ranging from 0.92 to 1.56. Several conclusions were drawn from the results of this study:

Steady-State Flow Conditions

- Increasing the flow velocity and water depth resulted in an increase in the hydrodynamic load acting on the debris dams and column, as shown in Figure 3.5. It was also found that the resistance coefficients typically varied with the Froude number, as illustrated in Figure 3.6 and Figure 3.7.
- Increasing dam height resulted in an increase in the resistance forces as the cross-sectional area of the flow obstruction increased. The height of the debris dams affected the resistance coefficients as increasing height results in greater flow redirection and aspect ratios. In addition, greater dam heights resulted in lesser contact of the column, which is more hydrodynamically-efficient relative to the rectangular or semi-cylindrical debris dams.
- An increase in the porosity of the debris dams resulted in lesser forces acting on the dams and column, as an increase in porosity resulted in less flow redirection. The porosity of dams resulted in a reduced bulk resistance coefficient. The porous holes reduced the loading, which caused the bulk resistance coefficient to decrease, as the area of the holes is not accounted for in the bulk area. There was no correlation between the effective resistance coefficient and porosity. As the porous holes result in an increase in skin friction, the decrease in area due to porosity does not result in an equivalent reduction of loading of an equal reduced area. Therefore, the porosity had little impact on the effective resistance coefficient as the area of the holes was deducted from the effective area.
- The changes in water depth upstream and downstream of the column increased with increasing Froude number, increasing dam height, and decreasing porosity.

Transient Flow Conditions

- Increasing the impoundment depth resulted in larger forces acting on the flow obstacles, due to the greater flow depths and velocities upstream of the column and debris dam, as illustrated in Figure 4.5. It was also found that the resistance coefficients decreased with increasing impoundment depth and Froude number (Figure 4.6, Figure 4.7).
- The rectangular dam resulted in greater resistance forces and resistance coefficients compared to the case of the cylindrical dam as rectangular obstacles are typically less hydrodynamically-efficient than cylindrical obstacles.
- Increasing the debris dam height resulted in an increase in the resistance forces acting on the column as this increased the area exposed to the flow. The dam height did not have a significant influence on the resistance coefficients, likely because the resistance force was normalized by the dam height through the cross-sectional area. In addition, greater debris dam heights led to the formation of greater water depths upstream of the column, which, in turn, resulted in a decrease in stream-wise velocities. This may reduce the loading for dams of greater heights.
- Increasing porosity resulted in a reduction in loading and a reduction in the bulk resistance coefficient as the holes cause less flow redirection. The effective resistance coefficient was not influenced by the porosity as the porous holes increase the surface area parallel to the flow, increasing the skin friction. The increase in frictional forces likely counteracts the decrease in blockage caused by the porosity.

Empirical relationships were developed for the bulk and effective resistance coefficients in terms of debris dam geometry and the flow conditions in both studies (Table 3.7 and Table 4.6). These relationships indicated that both investigations produced similar results in terms of the effects of Froude number and porosity on loading. Increasing the debris dam height resulted in increased forces. However, it was found that in transient flow conditions the height did not affect the resistance coefficient, whereas in steady-state conditions increasing height resulted in increased resistance coefficients. This could be attributed to the formation of greater surface rollers with increasing dam height. Surface rollers have been known to form in front of flow obstacles tested in dam-break waves (St-Germain et al., 2014; Derschum et al., 2017), which result in decreasing or negative horizontal velocities. Decreasing velocities result in a decrease in the drag force acting on obstacles, as illustrated by Stolle et al. (2018), so this could be the cause of the difference between the results of the steady-state and transient studies in terms of debris dam height. These conclusions were also confirmed by the Welch's *t*-tests that were conducted in both studies, which demonstrate the relationship between dependent variables based on the independent variables.

This study presents a preliminary investigation regarding the impact of debris damming on structural loading and the surrounding flow conditions. The conclusions stemming from this study illustrate that the potential flow conditions should be considered when applying a resistance/ drag coefficient. A conservative assumption in the design process should be that the debris dam is nonporous and its height is of the full flow depth where more specific information regarding potential debris dam characteristics are lacking. This research provides a basis regarding the geometry of debris dams' impact on loading and flow behaviour. However, further research is required to obtain a more comprehensive understanding of debris dam geometry and the associated impacts on structures.

5.2 Recommendations for Future Work

Based on the conclusions obtained from this study, recommended future research areas regarding debris damming loads and the associated flow conditions include:

- Most often, debris dams consist of buoyant materials in extreme flooding events. The dams tested in the present study were attached to the column using non-buoyant materials, which may influence the backwater rise observed, further influencing the resistance forces. Future work should test debris dams consisting of buoyant materials that are free to move as this could affect the flow behaviour and loading.
- The porous dams were modelled with the holes parallel to the flow direction. In reality, debris dams have 3-dimensional voids, which create further resistance to the flow. Future studies should model porosity with 3-dimensional voids as this would more accurately model the voids of debris dams.
- Further experiments should be conducted with a wider range of Froude numbers, dam shapes, heights, and porosities to develop a wider range of data, which would allow for a more comprehensive understanding of the impacts of debris dam geometry and tested flow conditions on the resistance forces.
- In addition, other variables pertaining to debris dams should be investigated in extreme flows in terms of flow behaviour and loading conditions. These include, but are not limited to, debris dam length, width, roughness, and permeability.
- Due to limitations surrounding equipment in the present study, in depth measurements of velocities and water depths surrounding debris dams were not completed. It would be beneficial to obtain a data set of water depths and velocities in a closer proximity to the debris dams to obtain a better understanding of debris dams' impact on the flow field. This would allow for further conclusions surrounding backwater rise, wake formation, and flow accelerations; all of which can have significant impacts on structural loading and scour formation.

References

Achenbach, E. (1974). “The effects of surface roughness and tunnel blockage on the flow past spheres.” *Journal of Fluid Mechanics*, 65(01), 113-125.

Alridge, T., Piper, B., and Hunt, J. (1978). “The drag coefficient of finite-aspect-ratio perforated circular cylinders.” *Journal of Wind Energy and Industrial Aerodynamics*, 3(4), 251–257.

Arnason, H. (2005). Interactions between an incident bore and a free-standing coastal structure. *PhD Thesis*, University of Washington, Seattle.

Arya, S. P. S. (1975). “A drag partition theory for determining the large-scale roughness parameter and wind stress on the Arctic pack ice.” *Journal of Geophysical Research*, 80(24), 3447–3454.

Asadollahi, N., Nistor, I., and Mohammadian, A. (2018). “Numerical investigation of tsunami bore effects on structures, part I: drag coefficients.” *Natural Hazards*, 96(1), 285–309.

Bocchiola, D., Rulli, M. C., and Rosso, R. (2008). “A flume experiment on the formation of wood jams in rivers.” *Water Resources Research*, 44(2).

Borrero, J. C. (2005). “Field Survey of Northern Sumatra and Banda Aceh, Indonesia after the Tsunami and Earthquake of 26 December 2004.” *Seismological Research Letters*, 76(3), 312–320.

Bricker, J. D., Francis, M., and Nakayama, A. (2012). “Scour depths near coastal structures due to the 2011 Tohoku Tsunami.” *Journal of Hydraulic Research*, 50(6), 637–641.

Bricker, J. D., Gibson, S., Takagi, H., and Imamura, F. (2015). “On the Need for Larger Mannings Roughness Coefficients in Depth-Integrated Tsunami Inundation Models.” *Coastal Engineering Journal*, 57(2).

Chanson, H. (2004). *Hydraulics of Open Channel Flow: An Introduction; Basic Principles, Sediment Motion, Hydraulic Modelling, Design of Hydraulic Structures.* Butterworth-Heinemann.

Chanson, H. (2006). “Tsunami Surges on Dry Coastal Plains: Application of Dam Break Wave Equations.” *Coastal Engineering Journal*, 48(4), 355–370.

Chaplin, J., and Teigen, P. (2003). “Steady flow past a vertical surface-piercing circular cylinder.” *Journal of Fluids and Structures*, 18(3-4), 271–285.

Chock, G. Y. K. (2015). “The ASCE 7 Tsunami Loads and Effects Design Standard.” *Structures Congress 2015*, Structural Engineering Institute of ASCE, 1446-1456.

Chock, G. Y. K. (2016). “Design for Tsunami Loads and Effects in the ASCE 7-16 Standard.” *Journal of Structural Engineering*, 142(11), 04016093.

Chow, V. T. (1959). *Open-channel hydraulics*. McGraw-Hill, New York.

City of Victoria. (n.d.). “Tsunami Readiness.” *https://www.victoria.ca*, (Jun. 25, 2019).

Costa, J. E., Jarrett, R. D. (2008). An Evaluation of Selected Extraordinary Floods in the United States Reported by the US Geological Survey and Implications for Future Advancement of Flood Science: US Geological Survey Scientific Investigations Report. 2008-5164, 10.

Derschum, C., Stolle, J., Nistor, I., and Goseberg, N. (2017). “Influence of wave-structure interaction on tsunami-driven debris impact.” *Proceedings of the International Short Course and Conference on Applied Coastal Research*, J. Lara and I. Losada, eds.

Diehl, T. H. (1997). “Potential drift accumulation at bridges.” U.S. Dept. of Transportation, Federal Highway Administration, *Rep. FHWA-RD-97028*, Washington, DC.

Donoho, D. L., and Johnstone, I. M. (1994). “Ideal Spatial Adaptation by Wavelet Shrinkage.” *Biometrika*, 81(3), 425.

Duinker, P. (2002). “Climate Change Impacts and Adaptation in Atlantic Canada.” Senate of Canada, <https://sencanada.ca/content/sen/committee/372/agri/power/atlantic-e.htm> (May 24, 2018).

El-Alfy, K. S. (2006) “Experimental study of backwater rise due to bridge piers as flow obstructions”. *Tenth International Water Technology Conference*, IWTC 10, 2006, 319- 336.

FEMA. (2011). “Coastal Construction Manual: Principles and Practices of Planning, Siting, Designing, Constructing, and Maintaining Residential Buildings in Coastal Area.” *FEMA P-55*, Federal Emergency Management Agency.

FEMA. (2012). “Guidelines for design of structures for vertical evacuation from tsunamis.” *FEMA P-646*, Federal Emergency Management Agency.

Fenton, J. (2003). “The effects of obstacles on surface levels and boundary resistance in open channels.” *In Proceedings of the 30th IAHR* Congress, Thessaloniki, Greece, Volume 2, pp. 9–16.

Fritz, H. M., Borrero, J. C., Synolakis, C. E., and Yoo, J. (2006). “2004 Indian Ocean tsunami flow velocity measurements from survivor videos.” *Geophysical Research Letters*, 33(24).

Goring, D. G. (1978). “Tsunamis - the propagation of long waves onto a shelf.” *Rep. Kh-R-38*, W. M. Keck Laboratory of Hydraulic and Water Resources, California Inst. of Technol., Calif.

Goring, D. G., and Nikora, V. I. (2002). “Despiking Acoustic Doppler Velocimeter Data.” *Journal of Hydraulic Engineering*, 128(1), 117–126.

Haehnel, R.B. and Daly, S.F. (2002). “Maximum impact force of woody debris on floodplain structures”. ERDC/ CRREL TR-02-2, US Army Corp of Engineers, Engineer Research and Development Center.

Häfen, H. V., Goseberg, N., Stolle, J., and Nistor, I. (2019). “Gate-Opening Criteria for Generating Dam-Break Waves.” *Journal of Hydraulic Engineering*, 145(3), 04019002.

Hammack, J. L. (1973). “A note on tsunamis: their generation and propagation in an ocean of uniform depth.” *Journal of Fluid Mechanics*, 60(4), 769–799.

Hammack, J. L., and Segur, H. (1974). “The Korteweg-de Vries equation and water waves. Part 2. Comparison with experiments.” *Journal of Fluid Mechanics*, 65(2), 289–314.

Hager, H., and Lauber, G. (1996). Hydraulische Experimente zum Talsperrenbruchproblem (Hydraulic experiments to dambreak problem). *Schweizer Ingenieur und Architekt I*, 14(24): 515-524 (in German).

Huang, N.E., Shen, Z., Long, S.R., Wu, M.C., Shih, H.H., Zheng, Q., Yen, N.-C., Tung, C.C., Liu, H.H. (1998). “The empirical mode decomposition and the Hilbert spectrum for nonlinear and non-stationary time series analysis.” *Proceedings of the Royal Society of London, Series: A*, 454, 903–995.

Hughes, S. A. (1993). “Physical Models and Laboratory Techniques in Coastal Engineering.” *Advanced Series on Ocean Engineering*.

Imamura, F., Goto, K., and Ohkubo, S. (2008). “A numerical model for the transport of a boulder by tsunami.” *Journal of Geophysical Research*, 113(C1).

Kajitani, Y., Chang, S. E., and Tatano, H. (2013). “Economic Impacts of the 2011 Tohoku-Oki Earthquake and Tsunami.” *Earthquake Spectra*, 29(S1).

Kulikov, E.A., Mendvedev, P.P. (2005). “Satellite recording of the Indian Ocean Tsunami on December 26, 2004.” *Doklady Earth Sciences A401*, 444–448.

Kundu, P. K. (1990). *Fluid Mechanics*. Academic, San Diego, 392.

Lagasse, P. F., Zevenbergen, L. W., and Clopper, P. E. (2010). “Impacts of Debris on Bridge Pier Scour.” *Scour and Erosion*. 7–10.

Laneville, A., and Yong, L. Z. (1984). “Mean Flow Patterns Around Two-Dimensional Rectangular Cylinders And Their Interpretation.” *Journal of Wind Engineering and Industrial Aerodynamics*, 14(1–3), 387–398.

Lauber, G., and Hager, W. H. (1998). “Experiments to dambreak wave: Horizontal channel.” *Journal of Hydraulic Research*, 36(3), 291–307.

Leal, J. G., Ferreira, R. M., and Cardoso, A. H. (2006). “Dam-Break Wave-Front Celerity.” *Journal of Hydraulic Engineering*, 132(1), 69–76.

Lekkas, E., Andreadakis, E., Alexoudi, V., Kapourani, E., and Kostaki, I. (2011). “The Mw=9.0 Tohoku Japan Earthquake (March 11, 2011) Tsunami Impact on Structures and Infrastructure.” *Environmental Geosciences and Engineering Survey for Territory Protection and Population Safety (EngeoPro) International conference, Moscow*, 97-103.

Liang, Q., Chen, K.-C., Hou, J., Xiong, Y., Wang, G., and Qiang, J. (2016). “Hydrodynamic modelling of flow impact on structures under extreme flow conditions.” *Journal of Hydrodynamics*, 28(2), 267–274.

Li, H., Li, Z., and Mo, W. (2017). “A time varying filter approach for empirical mode decomposition.” *Signal Processing*, 138, 146–158.

Lumbroso, D., and Gaume, E. (2012). “Reducing the uncertainty in indirect estimates of extreme flash flood discharges.” *Journal of Hydrology*, 414-415, 16–30.

Lyn, D. A., Cooper, T., Yi, Y. K., Sinha, R., and Rao, A. R. (2003). “Debris accumulation at bridge crossings: Laboratory and field studies*.” Rep. No. FHWA/IN/JTRP-2003/10*, Purdue Univ., West Lafayette, IN.

MathWorks. (2019). MATLAB User's Guide. The MathWorks, Inc., Natick, MA.

Matsutomi, H., Sakakiyama, T., Nugroho, S., and Matsuyama, M. (2006). “Aspects of Inundated Flow Due to the 2004 Indian Ocean Tsunami.” *Coastal Engineering Journal*, 48(2), 167–195.

Matsutomi, H., and Okamoto, K. (2010). “Inundation flow velocity of tsunami on land.” *Island Arc*, 19(3), 443–457.

McDonald, J. H. (2009). *Handbook of biological statistics*, 2nd Ed., Sparky House Publishing. Baltimore, MD.

Melville, B. W., and Dongol, D. M. (1992). “Bridge Pier Scour with Debris Accumulation.” *Journal of Hydraulic Engineering*, 118(9), 1306–1310.

Nagler, F. A. (1918). “Obstruction of bridge piers to the flow of water.” *Proceedings of the American Society of Civil Engineer*, 43(5), 815–846.

Naito, C., Cercone, C., Riggs, H. R., and Cox, D. (2014). “Procedure for Site Assessment of the Potential for Tsunami Debris Impact.” *Journal of Waterway, Port, Coastal, and Ocean Engineering*, 140(2), 223–232.

Nakayama, Y., and Boucher, R. F. (1998). *Introduction to Fluid Mechanics*. Butterworth-Heinemann Ltd, Oxford.

Neumann, B., Vafeidis, A. T., Zimmermann, J., and Nicholls, R. J. (2015). “Future Coastal Population Growth and Exposure to Sea-Level Rise and Coastal Flooding - A Global Assessment.” *Plos One*, 10(3).

Nistor, I., Goseberg, N., and Stolle, J. (2017). “Tsunami-Driven Debris Motion and Loads: A Critical Review.” *Frontiers in Built Environment*, 3.

Razaz, M., and Kawanisi, K. (2011). “Signal post-processing for acoustic velocimeters: detecting and replacing spikes.” *Measurement Science and Technology*, 22(12), 125404.

Paczkowski, K., Riggs, H., Naito, C., and Lehmann, A. (2012). “A one-dimensional model for impact forces resulting from high mass, low velocity debris.” *Structural Engineering and Mechanics*, 42(6), 831–847.

Pagliara, S., and Carnacina, I. (2011). “Influence of Wood Debris Accumulation on Bridge Pier Scour.” *Journal of Hydraulic Engineering*, 137(2), 254–261.

Pagliara, S., and Carnacina, I. (2013). “Bridge pier flow field in the presence of debris accumulation.” *Proceedings of the Institution of Civil Engineers - Water Management*, 166(4), 187–198.

Panici, D., and Almeida, G. A. M. D. (2018). “Formation, Growth, and Failure of Debris Jams at Bridge Piers.” *Water Resources Research*, 54(9), 6226–6241.

Parola, A. C., Apelt, C. J., and Jempson, M. A. (2000). *Debris forces on highway bridges*. National Academy Press, Washington.

Pasha, G. A., and Tanaka, N. (2016). “Effectiveness of Finite Length Inland Forest in Trapping Tsunami-Borne Wood Debris.” *Journal of Earthquake and Tsunami*, 10(04), 1650008.

Peakall, J. and Warburton, J. (1996). “Surface tension in small hydraulic river models- the significance of the Weber number.” *Journal of Hydrology*, 35(2): 199-212.

Pfister, M., Capobianco, D., Tullis, B., and Schleiss, A. J. (2013). “Debris-Blocking Sensitivity of Piano Key Weirs under Reservoir-Type Approach Flow.” *Journal of Hydraulic Engineering*, 139(11), 1134–1141.

Qi, Z. X., Eames, I., and Johnson, E. R. (2014). “Force acting on a square cylinder fixed in a free-surface channel flow.” *Journal of Fluid Mechanics*, 756, 716–727.

Rennie, C. D., and Hay, A. (2010). “Reynolds Stress Estimates in a Tidal Channel from Phase-Wrapped ADV Data.” *Journal of Coastal Research*, 261, 157–166.

Rueben, M., Cox, D., Holman, R., Shin, S., and Stanley, J. (2015). “Optical Measurements of Tsunami Inundation and Debris Movement in a Large-Scale Wave Basin.” *Journal of Waterway, Port, Coastal, and Ocean Engineering*, 141(1), 04014029.

Rossetto, T., Allsop, W., Charvet, I., and Robinson, D. I. (2011). “Physical modelling of tsunami using a new pneumatic wave generator.” *Coastal Engineering*, 58(6), 517–527.

Schalko, I., Lageder, C., Schmocker, L., Weitbrecht, V., and Boes, R. (2019a). “Laboratory Flume Experiments on the Formation of Spanwise Large Wood Accumulations: Part I—I. Effect on Backwater Rise.” *Water Resources Research*, 55.

Schalko, I., Lageder, C., Schmocker, L., Weitbrecht, V., and Boes, R. (2019b). “Laboratory Flume Experiments on the Formation of Spanwise Large Wood Accumulations: Part II—Effect on local scour.” *Water Resources Research*, 55.

Schmocker, L., and Hager, W. H. (2011). “Probability of Drift Blockage at Bridge Decks.” *Journal of Hydraulic Engineering*, 137(4), 470–479.

Schmocker, L., and Hager, W. H. (2013). “Scale Modeling of Wooden Debris Accumulation at a Debris Rack.” *Journal of Hydraulic Engineering*, 139(8), 827–836.

St-Germain, P., Nistor, I., Townsend, R., and Shibayama, T. (2014). “Smoothed-Particle Hydrodynamics Numerical Modeling of Structures Impacted by Tsunami Bores.” *Journal of Waterway, Port, Coastal, and Ocean Engineering*, 140(1), 66–81.

Stolle, J., Takabatake, T., Mikami, T., Shibayama, T., Goseberg, N., Nistor, I., and Petriu, E. (2017). “Experimental Investigation of Debris-Induced Loading in Tsunami-Like Flood Events.” *Geosciences*, 7(3), 74.

Stolle, J., Takabatake, T., Nistor, I., Mikami, T., Nishizaki, S., Hamano, G., Ishii, H., Shibayama, T., Goseberg, N., and Petriu, E. (2018a). “Experimental investigation of debris damming loads under transient supercritical flow conditions.” *Coastal Engineering Journal*, 139, 16–31.

Stolle, J., Ghodoosipour, B., Derschum, C., Nistor, I., Petriu, E., and Goseberg, N. (2018b). “Swing gate generated dam-break waves.” *Journal of Hydraulic Research*, 1–13.

Sumer, B. M., and Fredsøe, J. (1997). *Hydrodynamics around cylindrical structures*. World Scientific Publishing, Singapore.

Suppasri, A., Koshimura, S., Imai, K., Mas, E., Gokon, H., Muhari, A., and Imamura, F. (2012). “Damage Characteristic And Field Survey Of The 2011 Great East Japan Tsunami In Miyagi Prefecture.” *Coastal Engineering Journal*, 54(01), 1250005.

Technical Lifelines Council for Earthquake Engineering (TCLEE). (2006). “Hurricane Katrina: Performance of transportation systems.” R. Des Roches, ed., *ASCE Technical Council on Lifeline Earthquake Engineering Monograph No. 29*, American Society of Civil Engineers, June.

Yao, Y., Huang, Z., Lo, E. Y. M., and Shen, H.-T. (2014). “A Preliminary Laboratory Study of Motion of Floating Debris Generated by Solitary Waves Running up a Beach.” *Journal of Earthquake and Tsunami*, 08(03), 1440006.

Yarnell, D. L. (1934a). Pile trestles as channel obstructions. *Tech. Rep.* 429, US Department of Agriculture, Washington.

Yarnell, D. L. (1934b). Bridge piers as channel obstructions. *Tech. Rep.* 442, US Department of Agriculture, Washington.

Yeh, H., Barbosa, A. R., Ko, H., and Cawley, J. G. (2014). “Tsunami Loadings On Structures: Review And Analysis.” *Coastal Engineering Proceedings*, 1(34), 4.

Yeh, H., Sato, S., and Tajima, Y. (2013). “The 11 March 2011 East Japan Earthquake and Tsunami: Tsunami Effects on Coastal Infrastructure and Buildings.” *Pure Applied Geophysics*, 170(6-8), 1019–1031.

Yu, D., Butler, K., Kareem, A., Glimm, J., and Sun, J. (2013). “Simulation of the Influence of Aspect Ratio on the Aerodynamics of Rectangular Prisms.” *Journal of Engineering Mechanics*, 139(4), 429–438.

Zevenbergen, L. W., Lagasse, P. F., and Clopper, P. E. (2007). “Effects of Debris on Bridge Pier Scour.” *World Environmental and Water Resources Congress 2007*.